Plasmonic Cu-based Catalysts Towards Solar-driven Production of Hydrogen and Value-added Products from Alcohol

（Cu 基プラズモニック金属触媒による光誘起アルコールの脱水素反応に関する研究）

Shunqin LUO

Graduate School of Chemical Sciences and Engineering

Hokkaido University

2021

Contents

Contents

Contents

Abstract

Exploring new catalytic technologies for sustainable and highly-efficient H_2 production from renewable H_2 sources has attracted considerable attention. Due to the relatively high gravimetric H_2 content and easy availability from biomass fermentation, alcohols have been regarded as promising H_2 carriers. Cu-based materials, featuring good selectivity towards C-H bond activation and low price, are generally used for alcohol dehydrogenation. Nevertheless, the conventional alcohol dehydrogenation reactions suffer from intense energy consumption and unsatisfactory activity. In this thesis, the object is to introduce solar-energy as new form of stimulus, which could excite hot carriers from rational designed plasmonic Cu nanostructures for targeted activating specific chemical bonds of the reactants, initiating the alcohol dehydrogenation. Various strategies (i.e., modulating the size or composition of pristine Cu nanoparticle) were applied to improve the light harvesting and regulate the charge transfer pathway of plasmonic Cu towards highly-efficient solar-driven H_2 production from alcohol and thus to deepen the understanding of corresponding mechanism of plasmon-mediated reactant activation.

In chapter 1, a general background about solar-driven hydrogen production reaction and the fundamentals of plasmon-mediated photocatalytic processes (including plasmonic photocatalysis at room temperature, photothermal catalysis at high reaction temperature, and plasmonic photothermal catalysis where hot carrier activation and photothermal heating act in concert) were introduced. Then, the recent development of hydrogen production reaction driven by plasmon-mediated photocatalysis was summarized, with special attention given to the design concepts and reaction mechanisms of the catalysts.

In chapter 2, plasmonic Cu nanoparticles with different size distribution were developed for methanol self-coupling reaction to produce H_2 and methyl formate with the assistance of light energy. The results revealed that under purely thermocatalytic condition, the catalytic activity decreased with the increasing diameter of Cu nanoparticles; while in the photo-assisted thermocatalytic reaction, the optimized Cu catalysts with an average diameter of 34.8 nm exhibited the best photo-enhanced catalytic activity among other Cu samples. With the assistance of visible light, the apparent activation energy for methanol self-coupling over optimized Cu sample was reduced by

43% compared with purely thermocatalytic conditions, and the reaction activity was 14.4 time higher than that of thermocatalytic reaction rate at reaction temperature of 140 °C. Mechanistic investigations indicated that due to the effective visible light harvesting, the optimized plasmonic Cu could induce strong local electric fields and excite larger amounts of hot carriers, which played dominant role in activating the intermediate species and reducing the activation energies. The modulated plasmonic effect, together with the optimized thermocatalytic activity, rendered the optimal Cu nanoparticles a H_2 production activity of 4318 μmol g^{-1} min^{-1} with a high solar-to-energy of 3.6% during the solar-driven methanol self-coupling process.

In chapter 3, an efficient solar-driven ethanol dehydrogenation process was achieved using a low-cost Ni-Cu bimetallic catalyst for the high-yield and selective production of H_2 and acetaldehyde. Under the irradiation of focused simulated solar light, 176.6 mmol $g_{catalyst}^{-1}$ h^{-1} of H_2 production rate with a high solar-to-fuel conversion efficiency (3.8%) was achieved without additional thermal energy input. Mechanistic investigations revealed that photothermal heating and hot carrier generation over Ni-Cu catalysts took responsibilities for the high activity. Hot electrons generated from Cu nanoparticles could migrate to Ni atoms, which simultaneously favored the separation of charge carriers and the activation of adsorbates.

In chapter 4, in order to achieve highly efficient solar-driven methanol steam reforming (MSR) without additional thermal energy input, a low-cost plasmonic ZnCu alloy catalyst composed of Cu nanoparticles with surface-deposited Zn atoms was reported. An unprecedentedly high H_2 production rate of 328 mmol $g_{catalyst}^{-1}$ h^{-1} with a solar energy conversion efficiency of 1.2% under 7.9 Suns irradiation was obtained, which substantially exceeds the reported conventional photocatalytic MSR. Experimental results and theoretical calculations suggested that Zn atoms act not only as the catalytic sites for water reduction with lower activation energy, but also as the charge transfer channel, pumping hot electrons into water molecules and subsequently resulting in the formation of electron-deficient Cu for methanol activation. The interplay of dual active sites, together with photothermal heating, endowed the ZnCu catalysts with excellent capacity for activating both the water and methanol molecules, ultimately delivering a high H_2 production rate.

In chapter 5, an overall summary of this dissertation was presented. This thesis carried out a systematic study on Cu-based plasmonic nanoparticles for efficient solar-driven

alcohol reforming reaction for the production of H_2 and other high value-added products without additional thermal energy input. Various strategies have been employed to improve the catalytic activity through modulating the optical response and regulating the charge transfer pathway, such as modulating the size or composition of pristine Cu nanoparticle. With the assistance of photo-induced hot carriers, a higher reaction rate and lower apparent activation energy can be achieved. This thesis revealed that the morphology and structure of plasmonic nanoparticle were of significance in determining the optical response and charge transfer pathway, which could ultimately control the catalytic property. The findings in this study deepened the understanding of the interaction between hot carriers and surface reactants, and provided a potential strategy for initiating efficient H_2 production and various other energy-demanding industrial reactions through designing plasmonic nanostructures.

Chapter 1 Introduction

1.1 General background for solar-driven hydrogen production

With the continuous growth of the population and the significantly improvement of living standard, the global energy consumption has risen enormously.[1] To date, most of the energy is derived from burning non-renewable fossil fuels, leading to numerous problems such as CO_2 emission and environmental pollution.[2-4] As one of the pollution-free alternative power sources and an essential feedstock that can be utilized in various industrial processes (such as hydrogenation reaction and fuel cells), hydrogen is of great importance to the global energy system and chemical industry.[5] Currently, the H_2 has already become an important part of our clean and secure energy future, as the global demand for H_2 has grown more than threefold since 1975, reaching approximately 70 Mt in 2018.[6, 7] Conventional techniques for large-scale H_2 production are mostly through thermocatalytic reactions (e.g. steam reforming of methane, and water-gas shift), requiring high operating temperatures to achieve satisfactory reaction rate.[8, 9] In these cases, non-renewable fossil fuels were indispensably required as the energy input and the feedstock (source of the natural gas and coal). Seeking for a highly efficient and sustainable H_2 production strategy with low energy consumption and affordable cost is a challenging but essential task. In order to alleviate the reliance on fossil fuel while achieving highly efficient H_2 production, most researches have been focused on exploring alternative and sustainable hydrogen sources and developing energy-efficient catalytic processes by providing a new form of energy input.[10-12]

Solar-energy is the most abundant renewable energy resource, and is one of the most promising candidates in the future renewable energy supply framework.[13, 14] Using solar-energy by photocatalysts to initiate catalytic reactions, the so-called photocatalytic process, is an emerging trend and regarded as a promising strategy to curtail the increasing global energy demand while alleviating the environmental issues.[15] Adopting solar-energy solely as the energy input, CO_2, H_2O, and other building blocks can be transformed by photocatalysts into value-added chemicals (such as H_2, CO, and CH_4), demonstrating the concept of solar-to-fuel conversion by storing the solar-energy into chemical bonds efficiently.[16, 17] Due to the wide band gap and limited light-matter interaction, conventional semiconductor-based photocatalysis is facing two major

challenges: limited photo harvesting and low quantum efficiency. Extending the range of optical response to improve the solar light harvesting is highly desirable, and is considered as an effective approach for enormously enhancing the net reaction efficiency. Previous works suggested that the plasmonic photocatalysis performs attractive light absorption and charge carrier utilization features.[18, 19] In plasmonic photocatalysis, the free electrons in plasmonic metal nanoparticle can be collectively oscillated under light irradiation through the excitation of localized surface plasmon resonance (LSPR).[20] In addition to the electron-hole pairs generated from semiconductor photocatalysts, LSPR can serve as additional energy input for enhancing photocatalytic performance by converting light energy into the hot carrier. Since the resonant wavelength and LSPR intensity are determined by size, shape, and composition of the plasmonic nanostructures, it is possible to fabricate plasmonic nanometals with full solar-spectrum response.[21, 22]

Along with the plasmonic photocatalysts which combined plasmonic metals with semiconductors, utilizing plasmonic metals solely as catalysts has emerged as a cutting-edge research area of solar-to-fuel conversion technology.[23] The unique capability of plasmonic metals that combines light-harvesting, hot carrier excitation, photo-to-thermal conversion, and surface catalytic reaction in one material endows them with a bright future for catalyzing various chemical reactions. With the assistance of both hot carriers and photothermal heat, several conventional catalytic processes which originally driven by the thermal-energy can be initiated efficiently by the solar-energy via plasmonic photothermal technology without additional thermal energy input.[12, 24, 25] Furthermore, the participation of hot carrier into the surface reaction can preferentially activate desired chemical reactions through specifically targeting electronic excitations, offering a great potential to discover additional and more selective reaction pathways that cannot be accessed by the conventional thermocatalytic process.[26] These remarkable achievements strongly indicate that plasmonic photothermal technology taking the advantages of both the photo and thermal features of the sun light holds great promise for addressing the increasing global energy demands through solar-to-fuel conversion.

1.2 The fundamentals of plasmon mediated photocatalysis

Localized surface plasmon resonance (LSPR) is a common optical property of metallic nanoparticles, which can be visualized as the coherent oscillation of conduction electrons established when the frequency of the photons matches the natural frequency of the surface electrons oscillating against the restoring force of positive nuclei.[26] After the

intra-band (between Fermi level and the sp conduction band) or inter-band (between d band and sp conduction band) excitation of plasmonic nanometals, energetic hot carriers are produced from the dephasing of the free electron oscillation through non-radiative energy dissipation pathway (also known as Landau damping process).[22] Those hot carriers with sufficient energy can inject into the electron-accepting states of nearby surface adsorbates or semiconductors, inducing a surface chemical transformation (in femtosecond to picosecond level), or dissipate their energy into heat through the energy exchange between hot carriers and phonon modes (in picosecond to nanosecond level) to promote the mass transfer and reaction rate.[20, 23]

Depending on the type of main driving force, LSPR-mediated catalytic process over plasmonic nanostructures can be divided into plasmonic photocatalysis and photothermal catalysis, where the former is dominated by the charge carrier activation and the latter is governed by photothermal heat. It is noteworthy that through tailoring the optical properties (such as the energy of LSPR) of plasmonic metal to match the electronic structure of adsorbates, hot carrier activation and photothermal heat can be constructively coupled by the plasmonic photothermal catalysts under the irradiation of high-intensity light, ultimately initiating the surface reaction efficiently and selectively. Such a kind of reaction process is defined here as plasmonic photothermal catalysis that combines the advantages of plasmonic photocatalysis and photothermal catalysis. The reaction mechanism of plasmonic photothermal catalysis, including hot carrier transfer and photothermal conversion, has been introduced briefly in the following section.

1.2.1 Reaction mechanism of plasmonic photocatalysis

Purely plasmonic photocatalytic reactions are generally conducted at ambient temperature or low reaction temperature (less than 100 °C), where photo-induced hot carriers play a dominant role in the reaction, and the influence of photothermal heat is insignificant during the plasmonic photocatalysis. In the plasmonic photocatalytic process, photo-induced hot electrons can be produced over plasmonic nanoparticle and transfer to an adjacent semiconductor or interact with the molecules adsorbed on the surface of nanoparticle.[27-29] For the plasmonic metal/semiconductor system (Figure 1.1a), abundant hot electrons with high potential energy are generated from plasmonic metals via the LSPR excitation, followed by the efficient transferring of hot electrons to the conduction band (CB) of the interfaced semiconductors.[20, 30] The Schottky barrier (Φ_{SB}) formed at the semiconductor-metal interface prevents the flowback of the hot electrons,

extending the lifetime of the hot electron and accumulated electrons in the CB of the semiconductor, which is beneficial to various surface chemical reactions, such as H_2O splitting and CO_2 reduction.[31-33] On the other hand, for the plasmonic metal/adsorbate system, photo-induced hot carriers are in a distribution of low-energy charge carriers in high concentration. Hot carriers with suitable energy level can be injected into the adsorbates through accessible orbitals, which is called indirect hot carrier transfer mechanism (Figure 1.1b).[34] In addition, the hot carriers can be directly transferred from metals to adsorbates through a hybridized surface electronic states formed at the interface for activating the reactants, without the formation of the excited electron distribution (Figure 1.1c).[35-37] With the assistance of hot carriers, both the bond activation and the intermediate conversion can be facilitated through transient electronic excitations after photoexcitation of plasmonic nanostructures. In detail, hot carriers benefit the adsorbate molecules to evolve on the surface of plasmonic metal after energy transfer from plasmon to adsorbates along the excited potential energy surface, providing additional vibration energy to the adsorbates, and thus facilitating the chemical bonds activation.[37]

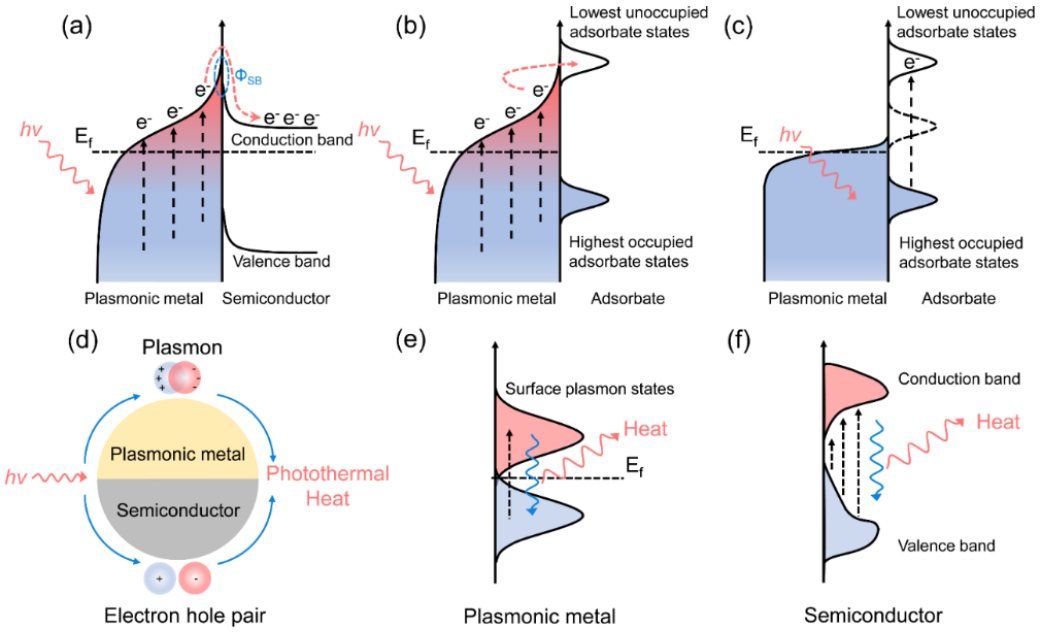

Figure 1.1 Schematic illustrations of the hot carrier transfer pathway and the photo-thermal conversion. (a) Hot electron transfer process in the plasmonic metal/semiconductor interface. (b) Indirect hot carrier transfer mechanism. (c) Direct hot carrier transfer mechanism. (d) Photo-induced thermal effect of plasmonic metal and semiconductor via plasmon- and exciton-based processes. (e) Photothermal conversion process over plasmonic metal. (f) Photothermal conversion process over semiconductor with LSPR characteristics.

The LSPR can be established when the light wavelengths are longer than the size of plasmonic nanoparticles, and the generation process of photo-induced hot carriers have been described by theoretical calculations.[38] By using a free electron mode, Nordlander and co-authors simulated the energy distribution of hot electrons and holes in Ag nanoparticle, and the results indicated that a higher production rate and lower energy of hot carriers could be achieved over larger nanoparticle.[39] In general, with the increasing size of plasmonic nanoparticles, a red-shift of LSPR absorption peak could be observed.[40] The resonant wavelength and the LSPR intensity are dependent on both the intrinsic nature of plasmonic metals and the geometry of plasmonic nanostructures.[21, 22] Plasmonic nanostructures with sharp features, such as the corners of nanocubes and tips of nanocones, demonstrate significantly higher local electromagnetic field enhancements compared with spherical nanoparticles with similar size.[41] Due to the lightning rod effect and reduced radiative damping, sharp features of plasmonic nanostructures can concentrate the incident light energy and increase the production of photo-induced hot carriers, which play important roles for activating surface chemical transformations.[42] Besides, through changing the size and shape of plasmonic nanostructures, a shift in the electric field density could be induced, changing the oscillation frequency of the electrons, therefore inducing different cross-section of the LSPR properties. Therefore, modulating the composition and geometry of the plasmonic nanostructures could ultimately result in enhanced catalytic property.[43] Among all the metallic elements, coinage elements (Cu, Ag, and Au) in Gourp IB demonstrate the best LSPR effect. The energy thresholds for the inter-band excitation of Cu and Au nanometals are 2.1 and 2.2 eV, respectively, indicating the visible light absorption capacity of Cu and Au.[44-46]

1.2.2 Reaction mechanism of pure photothermal catalysis

Solar-energy can also be converted into heat through photothermal conversion over plasmonic materials, providing sufficient thermal energy to stimulate the catalytic reactions (Figure 1.1d).[47] For plasmonic metallic nanostructures, upon light irradiation, the oscillation of conduction electron dephases and produces hot carriers. An athermal charge-carrier distribution then is formed.[48, 49] Afterwards, hot carriers cool down through transferring energy to lattice phonon. Namely, those energetic charge carriers, which do not participate in the charge migration process of surface reaction, would finally dissipate their energy to the phonon modes, inducing a considerable temperature increase on the surface of plasmonic nanometals (Figure 1.1e).[26, 50] During the photothermal conversion

process, the heat can be dissipated through particle-media interfaces after electron-phonon interaction. Therefore, the photothermal conversion efficiency are dependent on the medium and the particle size of plasmonic nanostructures. Generally, reducing the particle size of plasmonic nanometals can lead to an enhancement of the photothermal conversion efficiency.[51] For semiconductor nanomaterials with LSPR characteristics, the photo-induced electrons fall back to the lower energy states through releasing energy into photons or phonons, where the latter can interact with lattice to produce heat (Figure 1.1f).[52] Assuming that most of the carriers' energy is converted into heat through energy exchange between electrons and phonons, the reaction obeys the same mechanism with the conventional thermocatalytic reactions.[53] Contrary to plasmonic photocatalysis, pure photothermal catalytic processes generally occur in the gas-phase reactions, and light with high intensity (orders of magnitude higher than solar flux) is required to produce high temperatures to initiate the chemical reactions. In the pure photothermal catalysis, solar-energy merely converts into thermal energy, and the hot carrier-driven surface adsorbates activation is negligible.

1.2.3 Reaction mechanism of plasmonic photothermal catalysis

In the plasmonic photothermal catalysis, through rational design of plasmonic catalysts, hot carrier-driven reactant activation and photothermal heating co-exist and can be combined to synergistically drive the surface chemical reactions.[12, 25, 54] As instructed above, initially formed hot carriers after light excitation could redistribute their energy through different plasmon decay pathways.[23] Through electron-electron collisions, light-excited charge carriers over plasmonic metals could dissipate their energy, resulting in the secondary excitation of charge carriers; and this could lead to a Fermi-Dirac distribution of hot carriers near the fermi level of plasmonic metals.[26] High-energy charge carriers from such a distribution can participate in the surface chemical reactions through exchanging the energy between plasmonic nanostructures and surface adsorbed reactants.[26] Alternatively, adsorbate electronic states induced by strong interaction between plasmonic metals and adsorbates can serve as an additional channel for directly dissipating the LSPR energy.[37]

The prerequisites for realizing such hot electron activation processes contain several aspects. First, the existence of accessible adsorbate orbitals that could match with the electronic structure of plasmonic metals, or the presence of interfacial electronic states through the strong interaction between adsorbate and plasmonic metal that enables an

ultra-fast and momentum-reserved direct electronic excitation.[23] In addition, an intense electric field at the surface of plasmonic metals after light irradiation, which can reroute the charge excitation process, is also considered as the precondition for such an energy exchange process.[23] Consequently, hot carriers can facilitate the surface reaction through the following reaction roles: 1) Activating specific chemical bonds of surface reactants to modify the reaction pathway, which can enhance the selectivity and suppress unintended side reactions;[55] 2) Accelerating the desorption of certain surface-adsorbed species, which can further promote the catalytic activity and prolong the stability from resisting the coking of metallic nanoparticles.[11]

The residual hot carriers that do not participate in the surface catalytic reaction could subsequently cool down by transferring their energy to phonon modes, resulting in heating of the plasmonic metal surface.[23] Photo-induced heat can also serve as an effective driving force for stimulating surface reaction through the following functions: 1) Exciting the phonon modes of plasmonic nanoparticle, which could couple with reaction coordinate, evolving the surface-adsorbed reactants to products;[24] 2) Promoting the adsorption-desorption process of the surface catalytic process;[47] 3) Shifting the chemical equilibria toward a higher yield of end products. Compared with plasmonic catalysis and photothermal catalysis, plasmonic photothermal catalysis is much more attractive since both the light and thermal features of the solar light are concurrently utilized, resulting in highly efficient solar-to-energy conversion. Under such circumstances, the dual-functional roles of the plasmonic nanostructures (hot carrier-driven reactant activation and photothermal conversion) should be systematically considered and carefully differentiated.

There are several distinct signatures that can experimentally differentiate the contribution of hot carriers from photothermal heat: 1) Linear dependence of the reaction rate on light intensity indicates that the surface reaction is induced by hot carriers, and this can be attributed to the fact that the generation rate of hot carrier increases linearly with the photon flux;[26] 2) A higher kinetic isotope effect compared with the reaction driven by thermal energy at same reaction temperature;[56] 3) Modified selectivity for the chemical reaction induced by photo energy compared with the same reaction induced by thermal energy;[11] 4) Similar tendency of apparent quantum efficiency and the optical absorption spectrum of plasmonic metal.[57] The contribution of photo-induced hot carriers in the situation where the hot-carriers and photothermal heat work synergistically can be

evaluated through precisely designed contrast experiments.[12] More specifically, through comparing the catalytic activity under the purely solar-driven condition (without additional thermal energy input) and under thermocatalytic condition (without irradiation of light) with external heating temperature equivalent to those achieved under illumination, the contribution of hot carriers can be differentiated quantitively.[12] It should be noted that the surface temperature of catalyst needs to be detected accurately in such a process.[58]

The utilization of plasmonic photothermal technology presents several advantages. First, the most abundant and renewable solar-energy is adopted in the chemical reaction as the driving force, which can effectively reduce the consumption of non-renewable fossil fuels. Second, the reaction pathways can be modified by injecting hot carriers into specific chemical bonds, thus increasing the reaction selectivity. Third, compared with the thermocatalytic process, the milder reaction conditions of the photothermal catalytic process can lead to significant advantages, such as prolonged stability, enhanced safety, and a wider choice of catalyst.

1.3 Previous research on plasmon-mediated hydrogen production reaction

1.3.1 Plasmonic photocatalysis at ambient temperature

Metal nanoparticles with strong light scattering ability can generate hot electrons under ultraviolet, visible, and near-infrared light irradiation through the decay of surface plasmons. By applying hot electrons as the driving force to initiate the activation of adsorbates or intermediates, the performance of photocatalytic reactions can be enhanced.

Water splitting driven by solar-energy is a fundamental step for artificial photosynthesis toward a sustainable energy future. Combining an oxide semiconductor with plasmonic metal nanostructures for water splitting is prevalent because the utilization of the hot carriers generated from metals can reduce the recombination of charge-carriers during charge-carrier migration. In 2011, Chen et al. fabricated plasmonic Au-TiO_2 as the photocatalysts, and investigated the reaction mechanism for LSPR-mediated photocatalytic pure water splitting.[59] After UV irradiation for 7 h, a small amount of H_2 about 0.79 μmol g^{-1} was produced from TiO_2, while ~44-fold enhancement (35.04 μmol g^{-1}) has been achieved after Au incorporating. Whereas, no H_2 production was detected over Au-TiO_2 under the visible light irradiation, probably because the LSPR phenomenon of small Au nanoparticles (approximately 3 nm) is not significant. The

LSPR excitation of Au-CdS hybrids also assisted the electron transfer between the interface of Au and CdS. Naya et al. prepared selective deposited hexagonal CdS (shell) above Au nanoparticles (core) to form the Au-CdS heteroepitaxial junctional structure (Figure 1.2a and b) with different mean size (d_{Au}) and shell thickness (l_{CdS}).[60] As shown in Figure 1.2c, the Au LSPR showed strong damping around 620 nm in contrast to original Au signal with peak locating at λ = 520 nm. The H_2 production activity was controlled by both the lifetime (τ) of LSPR-electrons as well as the size of CdS nanoparticle (Figure 1.2d). Au-CdS (d_{Au} = 12.1 nm, l_{CdS} = 2.1 nm) gave continuous H_2 generation rate of (79.2 ± 2.1 μmol h^{-1} g^{-1}) with external quantum yield of 0.24% under excitation of red-light (λ = 640 nm). Benefited from LSPR, hot electrons generated from Au under red-light irradiation can transfer to CdS, endowing a stable stoichiometric water splitting of H_2 and O_2 (with production ratio 2:1) for more than 200 h (Figure 1.2e and f). Above study further verified that the geometry and the dimension of the plasmonic nanostructures determine the overall efficiency toward water splitting.

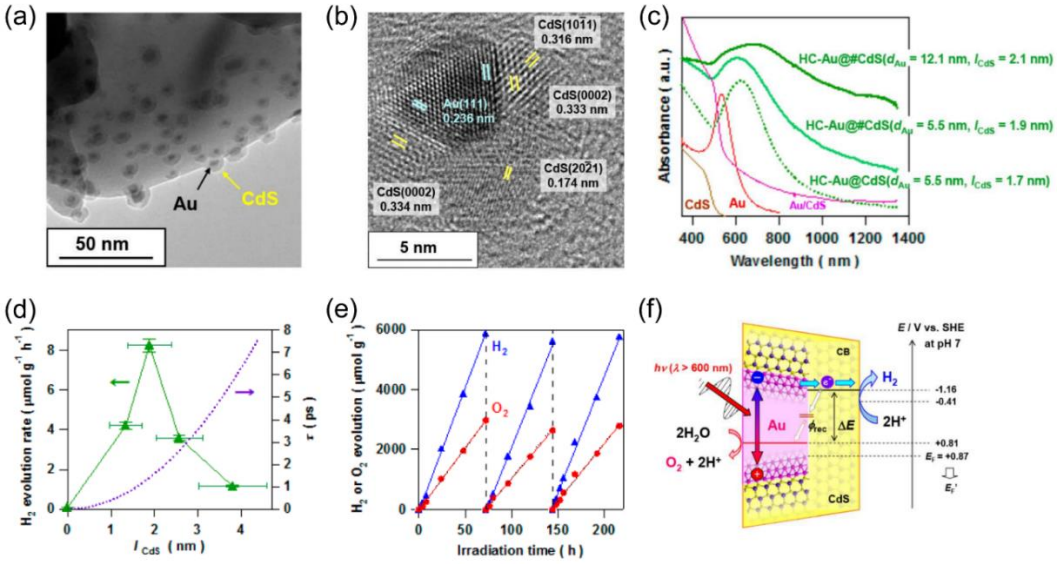

Figure 1.2 Plasmonic photocatalysis for overall water splitting. (a) and (b) TEM images for ZnO supported Au@CdS heteroepitaxial junctional structure. (c) UV-vis-NIR absorption spectra of Au@CdS. (d) H_2 evolution rate and electrons transit time in relation with CdS thickness. (e) Stability test over the optimal Au@CdS sample under red-light illumination. (f) Proposed LSPR-induced hot electron transfer mechanism.[60]

1.3.2 Photothermal catalysis at high temperature

Another strategy for initiating H_2 production reaction is via photo-thermochemistry, which utilizes full spectrum of sunlight to increase surface temperatures of catalysts and then initiate the thermocatalytic reactions.[61] Under this circumstance, photo-induced hot carriers play insignificant role in activating the surface adsorbed reactants, but dissipate their energy into heat through energy exchange between electrons and phonons. Group VIII nanometals are considered as promising candidate for photothermal catalysis by their outstanding photo-thermal conversion capacity and catalytic property, although their LSPR intensities are relatively weak.[62] Due to the high photo-thermal conversion efficiency of plasmonic photothermal catalysts, the surface temperatures of catalysts can be elevated to 300-600 °C under the irradiation of focused solar light, providing sufficient energy to stimulate thermodynamically unfavorable reactions, such as methane dry reforming and reverse water gas shift.[63-65]

Dry reforming of methane (DRM) ($CO_2 + CH_4 \rightarrow 2CO + 2H_2$ ΔH_{298K} = 247.3 kJ mol^{-1}), is a promising approach for converting two major greenhouse gases (CO_2 and CH_4) into syngas (CO and H_2). Thermodynamically, DRM requires a very high temperature to overcome the activation energy barrier, consuming a large amount of energy. The catalysts are also vulnerable to be deactivated in the harsh reaction conditions. Therefore, it is highly desirable to explore novel routes regarding the energy input and catalyst design. Recently, using photothermal route for driving CO_2 reduction with CH_4 has attracted tremendous research interests. Group VIII metals (such as Ni, Co, and Pt) were regarded as ideal catalysts for photothermal catalytic DRM.[65-67] For example, Li and co-authors designed silica-cluster-modified Ni nanocrystals (SCM-Ni/SiO_2) for highly efficient photothermal catalytic DRM.[66] Under the irradiation of focused light with high intensity, the surface temperature of SCM-Ni/SiO_2 could reach up to approximately 650 °C from photo-thermal conversion. Photo-induced heating served as the driving force to initiate the photothermal catalytic DRM without additional thermal energy input. Under the full spectrum light irradiation, high production rates of H_2 and CO (17.1 and 19.9 mmol min^{-1} g^{-1}) with solar-to-fuel conversion efficiency up to 12.5% can be achieved. Density functional theory (DFT) calculation was conducted via constrained occupancy approach to calculate the activation energy (Ea) for each elementary step both in excited state and ground state during the solar-driven DRM over Ni/SiO_2 slab, and the results revealed that the Ea for CH and CHO dissociation in the excited state were decreased (from 0.67 and

1.11 eV to 0.58 and 0.99 eV, respectively). Besides, the Ea for C and CH oxidation in the excited state also showed a slight decrease compared with the Ea in ground state, suggesting the existence of a photoactivation effect which was responsible for the acceleration of DRM. Besides, the SCM-Ni/SiO_2 demonstrated excellent durability. After 700 h reaction, no carbon deposition and deactivation could be observed over SCM-Ni/SiO_2. Based on the mechanistic investigations, authors concluded that highly efficient catalytic activity of SCM-Ni/SiO_2 towards solar-light-driven DRM can be attributed to surface plasmon-induced photo-thermal conversion and IR heating effect. High surface temperature on the catalytic active Ni nanocrystals took responsibility for high activity.

The water gas shift (WGS) reaction for hydrogen production ($CO + H_2O \rightarrow H_2 + CO_2$ $\Delta H_{298K} = -41.0$ kJ mol^{-1}) is an industrially essential process to convert coal resources into H_2.[68] In practical applications, high reaction temperatures (at least 200 °C) are required for efficient WGS reaction, although the standard thermodynamic of WGS is marginally favorable.[69] The supported metal catalysts, including noble metals (Au, Pt, Pd)[68, 70, 71] and transition metals (Fe, Cu)[72-75] with diverse supporters (CeO_2, ZrO_2, Al_2O_3, TiO_2, and ZnO),[70, 71, 75-80] have been extensively investigated in the thermocatalytic WGS reaction.

Recently, solar-driven WGS reaction, which combined the light features of the photocatalytic process and the thermal features of the thermocatalytic process by full utilization of solar light, has received significant attention for achieving highly efficient catalytic performance.[10] In a representative experiment, CuO_X/Al_2O_3 nanostructured materials, which consist of Cu nanoparticles and Cu_2O semiconductors, were designed for efficient solar-driven WGS reaction.[10] Solar energy was utilized as the only energy input to drive the WGS reaction, with no additional electric/thermal energy input. Under the light irradiation, a surface temperature of 285 °C was detected on CuO_X/Al_2O_3 catalysts. The solar-driven production rate of H_2 was approximately 122 μmol g_{cat}^{-1} s^{-1}, which is far more efficient than noble-metal-based catalysts (Au/Al_2O_3 and Pt/Al_2O_3) (Figure 1.3a). Furthermore, this solar-driven WGS reaction over CuO_X/Al_2O_3 catalysts demonstrated more than twice the activity of the thermal catalysis at a reaction temperature of ca. 300 °C, illustrating that solar energy not only can be converted into heat but also caused other effects to promote the reaction (Figure 1.3b). The UV-visible-NIR absorption spectra revealed that a wide wavelength range of solar light was absorbed by CuO_X/Al_2O_3 catalysts, indicating the high utilization efficiency of solar light (Figure 1.3c). ESR results showed that the interfacial oxygen vacancy of Cu-Cu_2O in CuO_X/Al_2O_3

catalysts can be induced by light irradiation (Figure 1.3d), which favored the production of H_2. Based on the experimental results, the authors proposed a coupling effect of the photothermocatalysis and photocatalysis processes over the CuO_X/Al_2O_3 catalysts (Figure 1.3e). Light was utilized solely as energy input for initiating the WGS reaction, which could reduce the total energy consumption for practical H_2 production from coal gasification. Besides, Xu and co-workers manipulated metal oxides (ZnO, Al_2O_3, and a mixture of ZnO and Al_2O_3) supported Cu nanomaterials for solar-driven WGS reaction.[81] Under the irradiation of a 300 W xenon light, a surface temperature of ca. 350 °C was measured on the catalysts. Cu-ZnO catalysts demonstrated the highest catalytic activity among all the samples, which could produce 9.5 mmol of H_2 in 30 min. The authors proposed that the local reaction temperature induced by the LSPR effect of Cu was responsible for the high activity.

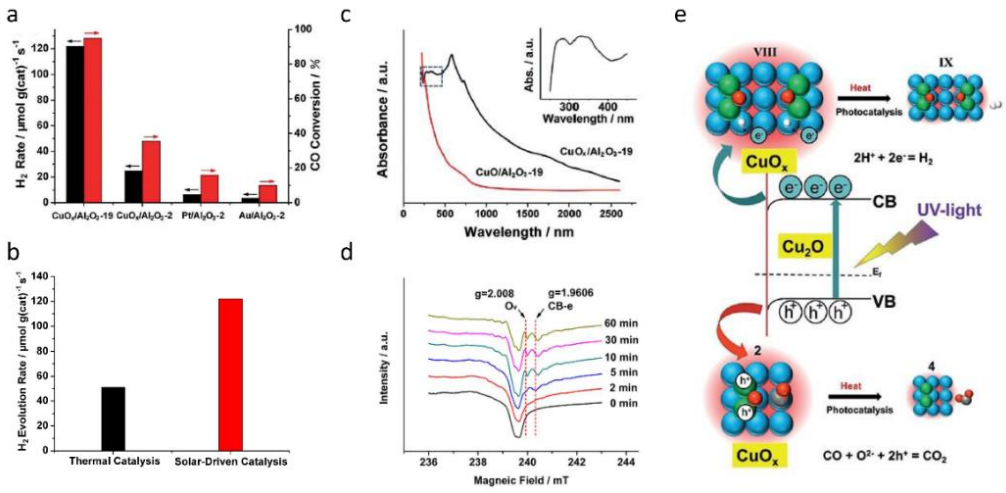

Figure 1.3 Solar-driven WGS reaction. (a) H_2 production activity and CO conversion efficiency over CuOx/Al_2O_3, Pt/Al_2O_3, and Au/Al_2O_3 catalysts. (b) Contrast of H_2 production efficiency under solar- and thermal-driven WGS conditions over CuOx/Al_2O_3 catalyst. (c) Light absorption spectra of CuOx/Al_2O_3 and CuO/Al_2O_3. (d) *In situ* ESR results of CuOx/Al_2O_3 catalyst during solar-driven WGS reaction. (e) Proposed reaction mechanism for solar-driven WGS reaction over CuOx.[10]

1.3.3 Plasmonic photothermal catalysis at high temperature

After the oscillated electrons are excited under the light irradiation over plasmonic metals, the high energy electrons can relax to the ground state by a non-radiative decay route, following the Frank-Condon principle. The photo-induced hot carriers can either interact with molecules adsorbed on the surface of plasmonic metals by the selective

activation of chemical bond of the adsorbates, or dissipate their energy into environment to increase the local temperature. Recently, several studies demonstrated that by rational design of plasmonic photothermal catalysts, the hot carrier and photothermal heating can contribute the reaction simultaneously, resulting in not only enhanced activity but also modulated selectivity.[50, 82, 83]

Recent study suggested that the solar-energy could be considered as an efficient stimulus for water splitting, and both the charge carriers and photothermal heat contributed to the reaction concertedly.[84] In a typical work, SiO_2/Ag@TiO_2 core-shell nanocomposites were designed and applied as a solar thermal collector to produce clean H_2 from glycerol aqueous solution.[84] Contrast experiments by using the illuminant in different wavelength ranges revealed that an H_2 production rate of 786 μmol g^{-1} h^{-1} was achieved over SiO_2/Ag@TiO_2 under the UV light irradiation, which was higher than SiO_2@TiO_2 and TiO_2 spheres (Figure 1.4a). All the samples were detected at similar temperatures (approximately 30 °C) under the irradiation of UV light, illustrating that the photothermal effect played a secondary role in this case (Figure 1.4b). After the illuminant was changed to full-spectrum, the reaction rate of SiO_2/Ag@TiO_2 was increased enormously to 1536 μmol g^{-1} h^{-1}. The significant enhancement of the catalytic activity, especially the SiO_2/Ag@TiO_2, was attributed to the photothermal effect, since a relatively large temperature difference of 2.6 °C between SiO_2/Ag@TiO_2 and SiO_2@TiO_2 were detected after the irradiation of full-spectrum (Figure 1.4c). However, no H_2 was detected for all samples when visible-NIR light was solely used for irradiation. The author proposed that the UV portion of the solar spectrum could be absorbed by the TiO_2 porous shell, while the SiO_2/Ag core absorbed visible and NIR light. In such a photocatalytic system, higher energy photons were used for electron-hole pairs generation, while lower-energy photons were used to heat the catalysts and enhance the hole-scavenging effect of glycerol by photothermal effects, achieving the full-spectrum utilization of solar light for photocatalytic H_2 production (Figure 1.4d).

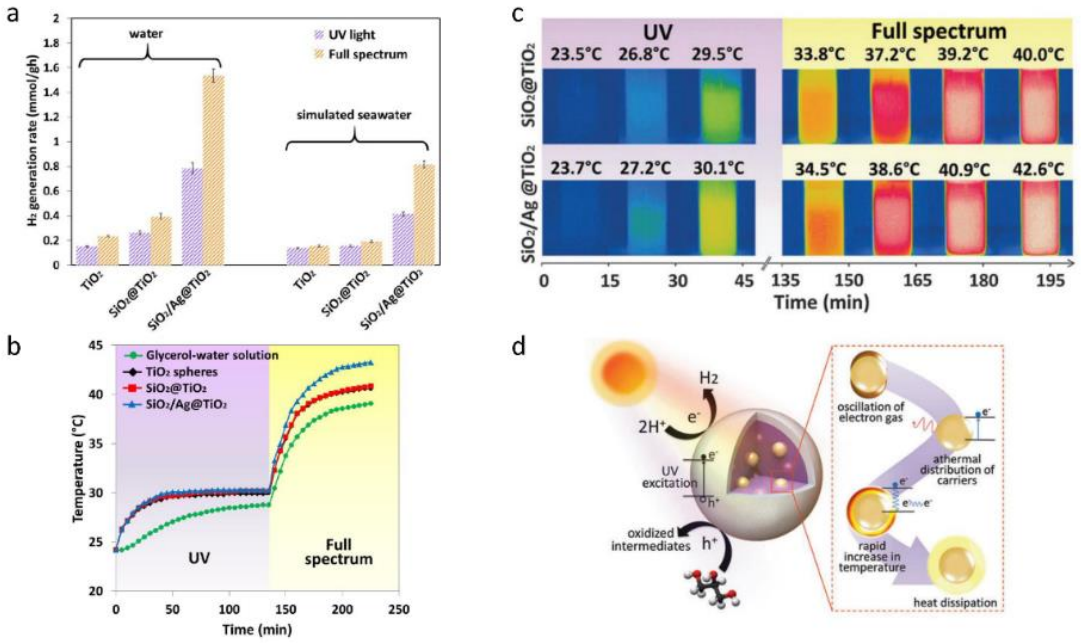

Figure 1.4 Solar driven H_2 production from glycerol aqueous solution. (a) H_2 production rates of TiO_2, SiO_2@TiO_2 and SiO_2/Ag@TiO_2 nanocomposites under different reaction conditions. (b) Detected temperatures of glycerol-water solution with and without photocatalysts under different irradiation conditions. (c) Infrared images of the reactor with different catalysts and under different irradiation conditions. (d) Schematic illustration of the proposed reaction mechanism.[84]

Dry reforming of methane (DRM), an industrially valuable but strong endothermic reaction for the H_2 production, can also be stimulated efficiently through plasmonic photothermal technology. Very recently, Halas and co-authors designed a plasmonic single atomic site antenna-reactor consisting of Cu nanoparticle "antenna" with the single Ru active "reactor" sites dispersed on the Cu surface (Cu-Ru) for efficient plasmonic photothermal DRM reaction.[11] The supercontinuum laser was applied as the energy supply to drive the photothermal DRM reaction. The surface temperatures of the catalysts under the illumination were recorded by a thermal camera. Under the irradiation, a surface temperature of 1000 K was detected over $Cu_{19.8}Ru_{0.2}$. The $Cu_{19.8}Ru_{0.2}$ demonstrated the optimal performance towards photothermal DRM among all samples, and a turnover frequency of 34 mol H_2 (mol Ru)$^{-1}$ s^{-1} was achieved under the irradiation of white light (19.2 W cm^{-2}) without external energy input (Figure 1.5a). Through the comparison of activity and selectivity over $Cu_{19.8}Ru_{0.2}$ under photo-driven and thermal-driven conditions at the same surface temperature induced by illumination and external heating, a hot

carrier-mediated DRM process was proposed (Figure 1.5b). The participation of hot carriers in the surface reaction was further confirmed by investigating the reaction selectivity under different light intensities, and an increased selectivity with light intensity was observed, which was in consistence with the hot-carrier-mediated reaction mechanism. In a such process, a solar-to-fuel energy conversion efficiency up to 15% was achieved under the irradiation of white light with strong light intensity of 16 W cm^{-2}. Based on the mechanistic investigations and theoretical calculations both in ground- and excited-state, the authors indicated that the advanced plasmonic photothermal catalytic activity of $Cu_{19.8}Ru_{0.2}$ can be attributed to two aspects. Firstly, atomic dispersed Ru active sites on the surface of Cu facilitated the CH_4 dehydrogenation with a suppressed side reaction (such as RWGS) and coke formation. Secondly, C-H bond activation and H_2 desorption on the Ru active sites were promoted by the photo-induced hot carriers, resulting in a substantial reduction of the energy barrier for CH_4 activation and eventually facilitating the charge transfer onto the detaching H (Figure 1.5c). Under intense white light irradiation, the plasmonic Cu could deliver the hot carriers to the surface Ru atoms, powering the surface reaction over Ru active sites. This study highlighted that the light-energy might be a more effective form of energy input for driving DRM. By utilizing plasmonic photothermal catalysis, the combination of photo-induced hot carriers and photothermal heating can be achieved for driving tough but industrially valuable reactions.

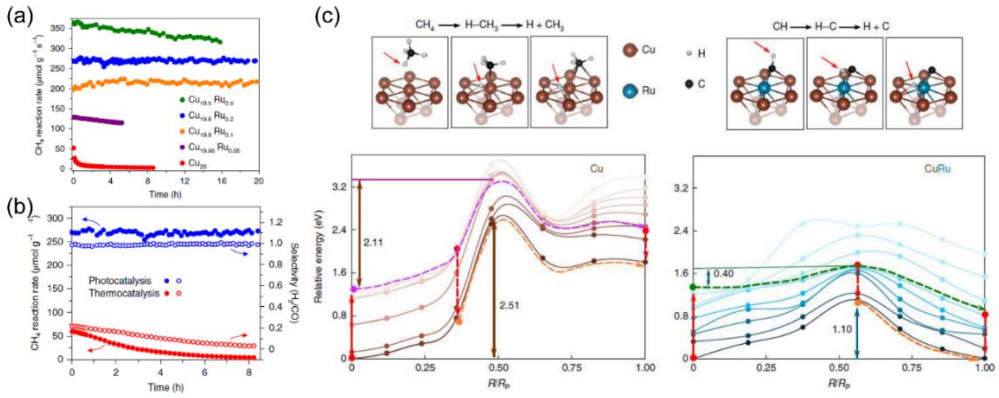

Figure 1.5 Plasmonic photothermal catalytic DRM reaction over Cu-Ru surface alloy antenna-reactor plasmonic photocatalysts. (a) Reaction activity and long-term stability of Cu-Ru catalysts with different Ru ratios for plasmonic photothermal catalytic DRM. (b) Comparison of the activity, stability, and selectivity of $Cu_{19.8}Ru_{0.2}$ under 19.2 W cm^{-2} white-light illumination and for thermocatalysis at a reaction temperature of 1000 K. (c) Calculated ground- and excited-state energy curves for CH_4 and CH dehydrogenation over Cu and Cu-Ru, respectively.[11]

1.4 H_2 production from alcohol

Currently, natural gas is served as the primary source of H_2, accounting for around 48% of the annual global dedicated H_2 production. Conventional H_2 production reactions (e.g., methane dry reforming and water gas shift reaction) are generally conducted in high temperature for achieving satisfactory reaction rate. Photocatalytic overall water splitting using solar light as the energy input for H_2 production is sustainable, yet the net reaction efficiency is still rather moderate. Recent advances highlighted that by adopting plasmonic photothermal technology, various conventional H_2 production reaction can be initiated by the solar energy, resulting in the greatly reduction of total energy consumption. Nevertheless, these reactions are still suffering from unsatisfactory reaction rate, unsustainability, and harsh reaction condition requirement due to the sluggish reaction kinetics and the consumption of fossil fuels (CH_4 and CO).

Recently, using renewable organics liquid as the H_2 source has attracted considerable attention.[85-87] The liquid organic hydrogen carriers (LOHC) concept, including transportation of H_2 in liquids and *in-situ* producing H_2, offers a flexible approach to solve the storage and transportation issues and enable a sustainable H_2 production.[88, 89] Various organics (such as methanol, ethanol, and formic acid) are considered as suitable LOHC, since they can be easily derived from the fermentation of renewable biomass, and can be dehydrogenated at elevated temperatures in the presence of catalysts.[90-92] Most of the research efforts have been devoted to the design and application of Cu-based and Pt-based materials in alcohol reforming.[93] Due to the high abundancy in earth's crust and good capacity for activating the C-H bond of alcohols, Cu-based materials have made great progress in industrial thermocatalytic alcohol reforming process.[93]

1.4.1 H_2 production from methanol

Methanol (CH_3OH) is the simplest alcohol and can be easily produced from various carbon sources such natural gas, coal, biomass, and carbon dioxide.[94] CH_3OH can be directly employed as an alternative energy carrier for numerous industrial applications, including methanol fuel cells and methanol-fueled vehicles. Furthermore, the relatively high gravimetric hydrogen content (12.6 %) renders the methanol as an ideal LOHC.[85] The CH_3OH can be dehydrogenated at relatively mild reaction conditions compared with traditional methane reforming process. The methanol steam reforming (MSR) reaction ($CH_3OH + H_2O = CO_2 + 3H_2$, $\Delta H_{298K} = 48.97$ kJ mol^{-1}) can produce H_2 as the main

product with a small amount of carbon monoxide and carbon dioxide, and such a reaction generally operates at temperatures of 200-350 °C.[95] It is highly desirable to hinder the generation of by-products (especially for CO) during the MSR, as a trace amount (10 ppm) of CO could destroy the catalysts. Currently, the representative catalysts for methanol reforming are $Cu/Zn/Al_2O_3$-based and Pt-based catalysts.[93, 95]

It is generally considered that the active site on the $Cu/Zn/Al_2O_3$-based catalysts for methanol dehydrogenation reaction (i.e., methanol decomposition or reforming) is Cu, which is related to the unique capacity for activating C-H bond of the alcohol.[96] Various parameters of Cu nanoparticle determine the overall catalytic performance, such as the chemical composition and the fabrication process of the Cu-based catalysts.[97-99] The promotion effect of ZnO over $Cu/Zn/Al_2O_3$-based catalysts towards methanol reforming is generally considered to be minimal, but it is mainly regarded as the supporter to prevent the sintering of Cu nanoparticles in the elevated reaction temperatures. Whereas some studies suggested a promotional effect of ZnO additives on Cu for MSR reaction.[100] Ceria has been regarded as an idea catalyst for driving a variety of thermocatalytic reaction including MSR.[101] Liu and co-authors reported the promotion effect of cerium towards MSR over Cu-based materials. In their work, Cu/CeO_2 catalysts were designed and synthesized for thermocatalytic MSR. The results demonstrated that Cu/CeO_2 catalysts exhibited higher activity among all samples. The authors indicated that a greatly enhanced activity was attributed to the higher dispersion of Cu nanoparticles and strong metal-support interaction.[101]

Previous studies suggested the thermocatalytic steam methanol reforming activity could be promoted by light energy.[102-104] For example, in the Cu-Ti-Zn oxides system, photo-energy was utilized to activate the catalysts and improve the activity towards steam methanol reforming.[103] Cu-Ti-Zn oxides were synthesized by a co-precipitation approach, and a fixed bed reactor was utilized to measure the activity for photo-assisted steam methanol reforming reaction. The production rate of H_2 was approximately 76.2 mmol g^{-1} h^{-1} at the reaction temperature of 210 °C with the irradiation of simulated sunlight, which was 6 times higher compared to that without light irradiation. Contrast experiment by the irradiation of light in different wavelengths at a reaction temperature of 210 °C indicated that the H_2 production was assisted by the introduced light energy (Figure 1.6a), and the UV portion of the light plays critical role in facilitating the steam methanol reforming reaction (Figure 1.6b). Long term reaction measurements suggested that a photo-induced

in-situ activation of the catalysts occurred at the early stage of the catalytic reaction. Control experiments over different catalysts (Cu-Ti, Zn-Ti, and Cu-Zn oxides) suggested that the photo-activation process was mainly occurred on Cu. H_2 temperature-programmed reduction (TPR) measurement results suggested that Cu-Ti-Zn oxides possessed the best reducibility among all the samples. Cu Auger spectrum further confirmed that the Cu (II) in Cu-Ti-Zn oxides were reduced to Cu (I) after the photo-activation. Based on the experimental results, the author concluded that the photo-energy could activate the catalysts and promoted the activity for steam methanol reforming synergistically. In the purely thermocatalytic conditions, the Cu in Cu-Ti-Zn oxides was CuO, while it reduced to Cu_2O and served as active catalysts for steam methanol reforming reaction after light irradiation. The photo-induced electron-hole pairs on the activated catalysts could further facilitate the surface reaction, promoting the activity. However, in this paper, thermal energy was indispensably consumed as the main driving force to stimulate the reaction (with the light energy being the secondary one).

Pt-based catalysts also attracted considerable attention for methanol reforming. For instance, the Pt/MoC was designed by Ma and coauthors, and the catalysts demonstrated superb catalytic efficiency towards H_2 production through CH_3OH reforming.[95] At the reaction temperature of approximately 190 °C, a high turnover frequency (TOF) of 18046 h^{-1} were achieved (Figure 1.6c). The authors proposed that the Pt was favored for activating C-H bond of methanol, whereas the MoC was favored for water dissociation. These combined merits endowed the Pt/MoC catalysts a high reaction efficiency. Similar materials design concept was also applied for the fabrication of Ni/MoC towards H_2 production from methanol reforming. Very recently, Ma and co-authors designed MoC catalysts supporter with surface dispersed single atom Ni sites (Ni/MoC), and the Ni/MoC was applied for initiating methanol reforming at 240 °C (Figure 1.6d). The results showed that Ni/MoC catalysts demonstrated approximately 6 times higher activity than that of Pt/Al_2O_3.[105] The authors proposed that the observed activity could be attributed to the efficient C-H bond dissociation over single atom Ni active sites as well as the outstanding water activation capacity of MoC.[105]

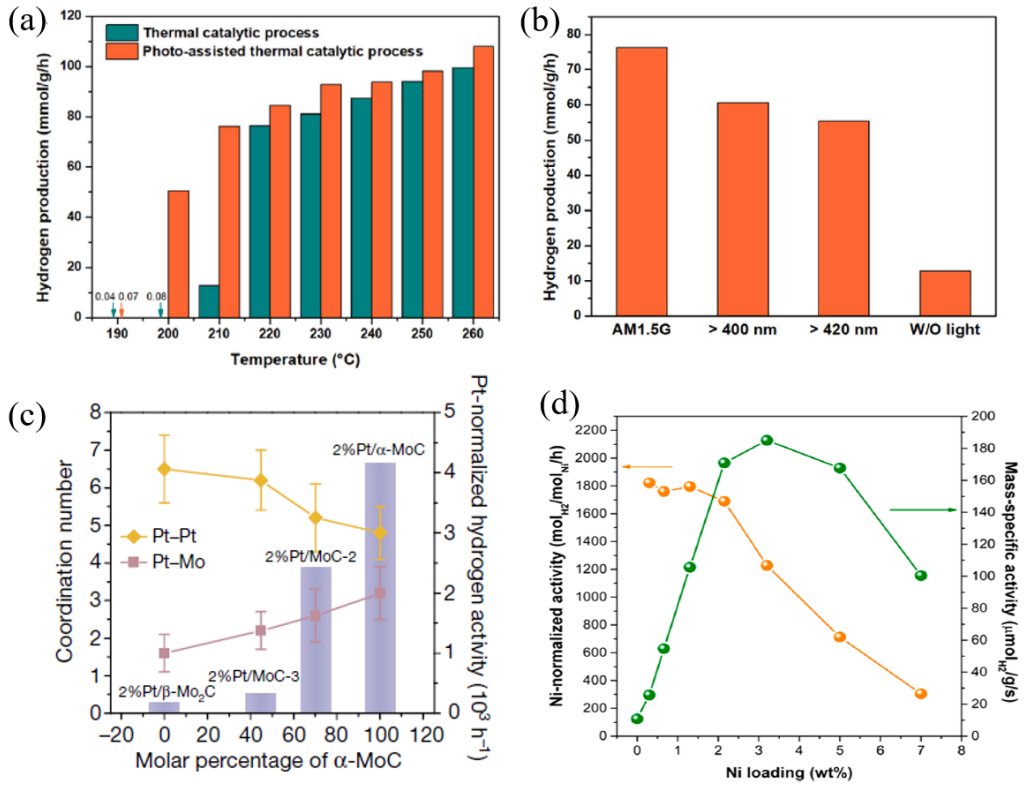

Figure 1.6 Methanol reforming for H_2 production. (a) Optimal MSR activity under thermocatalytic and photo-assisted catalytic conditions over Cu-Ti-Zn oxides. (b) Wavelength-dependent H_2 production efficiency at the reaction temperature of 210 °C over Cu-Ti-Zn oxides.[103] (c) Dependence between coordination numbers and catalytic activity over Pt/MoC samples.[95] (d) Normalized catalytic performance over different Ni/α-MoC catalysts.[105]

1.4.2 H_2 production from ethanol

In addition to the methanol, ethanol can also be regarded as a potential LOHC by its high energy density and low toxicity.[92, 106, 107] Since the large scale of ethanol production from biomass-treatment (bio-ethanol) has been industrialized,[108] ethanol processing is economically competitive thus attracting increasing interest in recent years.[109] The non-oxidative ethanol dehydrogenation ($CH_3CH_2OH = H_2 + CH_3CHO$, ΔH_{298K} = 68.9 kJ mol^{-1}) has been regarded as an industrially important process to generate clean H_2 and acetaldehyde simultaneously. The acetaldehyde is one of the most critical intermediates for the synthesis of high value-added fine chemicals.[110-112] Moreover, the non-oxidative ethanol dehydrogenation is also the first elementary step for ethanol reforming process, including steam reforming and partial oxidation.[113, 114] The supported Cu nanocatalysts

are the commercial materials for thermocatalytic ethanol dehydrogenation, requiring relatively high reaction temperatures (~300 °C) to obtain optimal efficiency.[110, 111, 115] However, it has been found that the catalytic activity of Cu was decreased rapidly due to the sintering of Cu nanoparticles at the elevated reaction temperatures.[116, 117]

Recently, Sykes and co-authors developed Pt-Cu single atom alloy for ethanol dehydrogenation towards selective production of H_2 and acetaldehyde. The results demonstrated that adding 1% percent of Pt on the surface of Cu nanoparticle can result in a 6-fold enhancement of the activity towards ethanol dehydrogenation. Mechanistic investigations suggested that O-H bond of the ethanol was activated by surface deposited Pt active sites, followed by ethoxy spillover to Cu sites, inducing a significantly enhancement of the ethoxy. Then, the ethoxy intermediate was further dissociated through C-H bond scission, forming the acetaldehyde as the final products and desorbed from Cu (111).[118] Flytzani-Stephanopoulos and co-authors found that the C-H bond activation of the ethanol can be considered as the rate determining step for the ethanol dehydrogenation. Through adding a little amount of Ni, the reaction rate of Cu nanoparticles could be enhanced enormously.[110] The Cu nanomaterials were constructed through wet chemistry method, and the Ni atoms were anchored on the surface of Cu by using electroless galvanic replacement method. The results showed that the Ni atoms were anchored on the surface of Cu as the single atom (Figure 1.7a). The ethanol dehydrogenation reaction was conducted in a temperature range of 150 to 200 °C. Compared with pristine Cu, PtCu single atom alloy, as well as PdCu single atom alloy, NiCu single atom alloy demonstrated greatly reduced apparent activation energy (Figure 1.7b). These results indicated that adding a small amount of Ni in Cu nanoparticle could greatly facilitate the ethanol dehydrogenation. Mechanistic investigation by using *in-situ* DRIFTS revealed that the participation of Ni atoms in the C-H dissociation of ethanol played critical role for the observed high activity (Figure 1.7c). Lu and co-authors developed a serious of Cu-based nanomaterials with different catalysts supports, and the dependence of selectivity and stability of ethanol dehydrogenation on different active sites and supports was investigated.[119] The results showed that the Cu nanoparticle supported by mesoporous carbon demonstrated excellent catalytic performance towards ethanol dehydrogenation. At a reaction temperature of 280 °C, an ethanol conversion rate of 73% with the selectivity of 94% were detected, and the activity was 1.7 time higher than that of Cu/SBA-15 (Figure 1.7d).

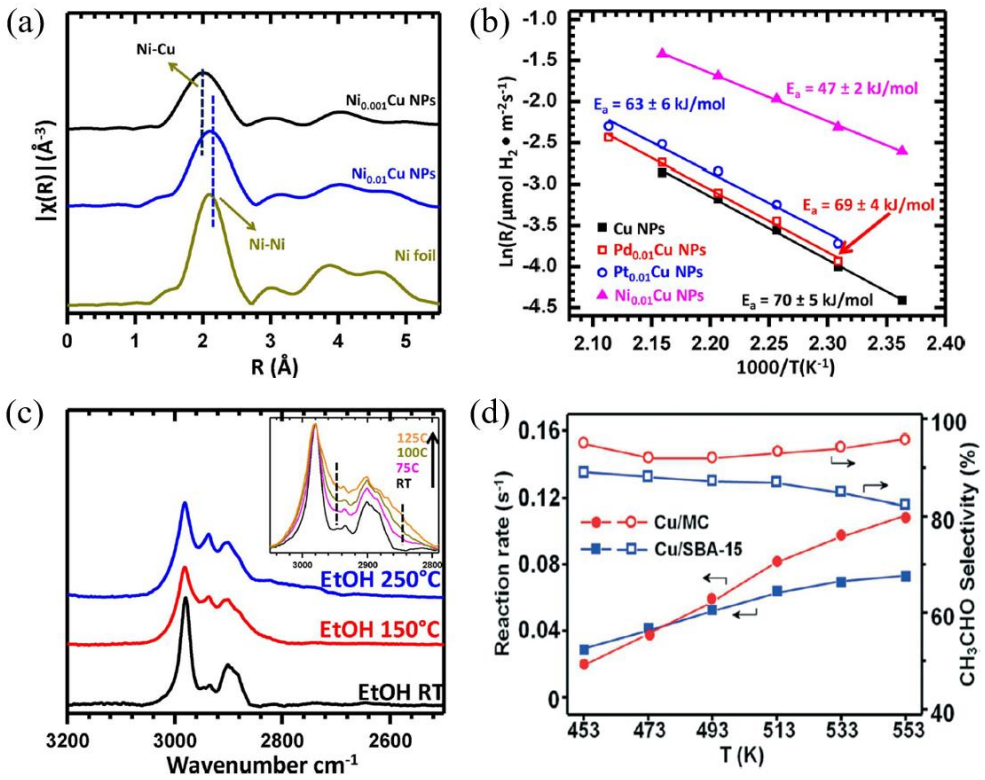

Figure 1.7 H_2 production from ethanol dehydrogenation. (a) Ni K-edge EXAFS data of different catalysts. (b) Apparent activation energy during thermocatalytic ethanol dehydrogenation over different catalysts. (c) DRIFT spectra over NiCu single atom catalysts under ethanol atmosphere at different temperatures.[110] (d) Reaction rate and selectivity during ethanol dehydrogenation over different catalysts.[119]

1.5 Thesis motivations and organization

Considering the relatively high gravimetric H_2 content, easy availability from biomass fermentation, and mild H_2 releasing condition, alcohols have been regarded as promising H_2 sources. Compared with conventional thermocatalytic H_2 production reaction (i.e., methane reforming and water gas shift) that heavily relies on the non-renewable fossil fuels, alcohol reforming for H_2 production is of great interests by its sustainability and lower energy consumption. Nevertheless, to date, in order to obtain satisfactory production rate in the alcohol reforming system, thermal energy is still required as the main energy input to drive the reaction. In this case, it is of great significance to develop a cost-effective and sustainable catalytic technology (without any thermal energy input) for alcohol dehydrogenation by providing a new form of energy input and constructing efficient catalysts.

Chapter 1

Plasmonic photothermal catalysis has been adopted as a promising alternative strategy for initiating a variety of conventional catalytic process. Benefiting from the rational design of the catalysts, plasmonic nanostructures could exhibit both plasmonic and photothermal attributes. Although there have been significant developments in plasmonic catalysis in the past few years, the reaction efficiency is still rather moderate due to the limited light capturing ability and disordered charge transfer process. Furthermore, very limited studies have reported to utilize plasmonic photothermal catalysts for initiating alcohol reforming towards H_2 production. In order to construct a highly efficient and sustainable solar-driven H_2 production processes, great research efforts should be devoted into the following two aspects: 1) Rational design of plasmonic nanostructures with excellent light response, numerous active catalytic sites, and regulated charge transfer pathway; 2) Exploring new reactions that can utilize solar-energy to initiate efficient H_2 production from renewable H_2 sources with mild reaction condition requirement.

Therefore, in this thesis, the object is to utilize solar energy to initiate alcohol dehydrogenation over plasmonic nanostructures towards a highly-efficient and sustainable H_2 production. Due to the the good visible light response, low cost, and the unique capacity for activating C-H bond of the alcohols, Cu-based materials are selected in this thesis. Several types of the strategies are considered to further enhance the photocatalytic activity of plasmonic Cu nanoparticles, including size modulation and components regulation to further improve the activity for alcohol reforming. This dissertation is divided into five chapters. A summary of the remaining four chapters is described as below:

Chapter 2 Solar-driven methanol self-coupling to produce hydrogen and methyl formate over plasmonic Cu nanoparticles with optimized size

Recent researches have indicated that after light irradiation, the interaction between surface adsorbates and photo-induced hot carriers on the surface of plasmonic nanoparticles could serve as an additional energy input to enhance the thermocatalytic performance under milder conditions. However, up until now, no work has been reported on solar-driven methanol self-coupling over plasmonic Cu. In order to achieve a highly-efficient solar-driven catalytic activity without additional thermal energy input, both the thermocatalytic and plasmonic properties of Cu nanoparticles should be considered systematically, and all these properties are governed by the size distribution. In this chapter, Cu nanoparticles with different size distribution were fabricated and were

utilized for photo-assisted thermocatalytic methanol self-coupling reaction. It can be expected that the Cu nanoparticles with optimized size distribution can effectively utilize solar energy to produce larger amounts of energetic hot electrons for activating the reactants. The modulated optical absorption property, together with thermocatalytic performance, may ultimately result in a highly-efficient catalytic activity under light irradiation.

Chapter 3 Solar-driven production of hydrogen and acetaldehyde from ethanol on Ni-Cu bimetallic catalysts

Ethanol dehydrogenation is a promising approach to produce hydrogen and acetaldehyde. Cu-based materials are considered as one of the most promising candidates for ethanol dehydrogenation due to their good selectivity and low cost. Up until now, in order to obtain a satisfactory production rate for ethanol dehydrogenation, thermal energy is still required as the main energy input to drive the reaction, consuming a large amount of energy. Previous studies demonstrated that the deposition of Ni single atom on the surface of Cu can further facilitate the C-H bond activation (the rate determining step for ethanol dehydrogenation), however, no work has been reported on solar-driven ethanol dehydrogenation reaction. In this chapter, an efficient solar-driven ethanol dehydrogenation system (without any thermal energy input) over Ni-Cu bimetallic catalysts was developed. It can be expected that under solar-light irradiation, photothermal heating and hot carrier generation over Ni-Cu catalysts could work synergistically for initiating ethanol dehydrogenation reaction. Hot electrons could be generated from Cu nanoparticles, and could migrate to surface Ni active sites, which simultaneously favored the separation of charge carriers and the C-H bond activation.

Chapter 4 Exploiting water and methanol activation for solar-driven H_2 production: interplay of dual active sites over plasmonic ZnCu alloy

To achieve highly efficient methanol steam reforming under mild reaction conditions, both methanol and water molecules need to be activated effectively. Considering the excellent visible-light response for hot carrier excitation and the good ability for activating C-H bond of methanol over Cu nanoparticles, I reasoned that the modification of Cu by other components with an outstanding capacity for water activation could bring a further catalytic activity enhancement towards solar-driven MSR. In this chapter I developed a Zn-Cu alloy plasmonic catalyst that comprise homogeneously dispersed Zn atoms on the surface of Cu. I proposed that introducing Zn atoms can lower the activation

energy of water dissociation, and can trap the hot electrons from Cu and deliver them to water molecules, further promoting the water activation and retarding the back-flow of hot electrons. Such a charge migration process could suppress the non-effective carrier recombination, and subsequently induce electron-deficient Cu for methanol oxidation. The interface formed between Zn and Cu in ZnCu alloy could favor the hot carrier transfer to activate both the water and methanol molecules, which accounts for the hot carrier-mediated catalytic performance.

Chapter 5 General conclusions and future prospects

This chapter presented an overall summary and conclusion of this dissertation and gave the prospects for future work.

References

1. J. Chow, R. J. Kopp and P. R. Portney, *Science*, 2003, **302**, 1528.

2. S. Shafiei and R. A. Salim, *Energy Policy*, 2014, **66**, 547-556.

3. A. Shahsavari and M. Akbari, *Renewable Sustainable Energy Rev.*, 2018, **90**, 275-291.

4. D. Gielen, F. Boshell and D. Saygin, *Nat. Mater.*, 2016, **15**, 117-120.

5. I. P. Jain, *Int. J. Hydrogen Energy*, 2009, **34**, 7368-7378.

6. I. Staffell, D. Scamman, A. Velazquez Abad, P. Balcombe, P. E. Dodds, P. Ekins, N. Shah and K. R. Ward, *Energy Environ. Sci.*, 2019, **12**, 463-491.

7. E. S. Hanley, J. P. Deane and B. P. Ó. Gallachóir, *Renewable Sustainable Energy Rev.*, 2018, **82**, 3027-3045.

8. D. S. Newsome, *Catal. Rev.*, 1980, **21**, 275-318.

9. A. Iulianelli, S. Liguori, J. Wilcox and A. Basile, *Catal. Rev.*, 2016, **58**, 1-35.

10. L. Zhao, Y. Qi, L. Song, S. Ning, S. Ouyang, H. Xu and J. Ye, *Angew. Chem. Int. Ed.*, 2019, **58**, 7708-7712.

11. L. Zhou, J. M. P. Martirez, J. Finzel, C. Zhang, D. F. Swearer, S. Tian, H. Robatjazi, M. Lou, L. Dong, L. Henderson, P. Christopher, E. A. Carter, P. Nordlander and N. J. Halas, *Nat. Energy*, 2020, **5**, 61-70.

12. L. Zhou, D. F. Swearer, C. Zhang, H. Robatjazi, H. Zhao, L. Henderson, L. Dong, P. Christopher, E. A. Carter, P. Nordlander and N. J. Halas, *Science*, 2018, **362**, 69-72.

13. Y. A. Wu, I. McNulty, C. Liu, K. C. Lau, Q. Liu, A. P. Paulikas, C.-J. Sun, Z. Cai, J. R. Guest, Y. Ren, V. Stamenkovic, L. A. Curtiss, Y. Liu and T. Rajh, *Nat. Energy*, 2019, **4**, 957-968.

14. S. Chen, T. Takata and K. Domen, *Nat. Rev. Mater.*, 2017, **2**, 17050.

15. D. Voiry, H. S. Shin, K. P. Loh and M. Chhowalla, *Nat. Rev. Chem.*, 2018, **2**, 0105.

16. Y. Wang, X. Shang, J. Shen, Z. Zhang, D. Wang, J. Lin, J. C. S. Wu, X. Fu, X. Wang and C. Li, *Nat. Commun.*, 2020, **11**, 3043.

17. X.-B. Li, C.-H. Tung and L.-Z. Wu, *Nat. Rev. Chem.*, 2018, **2**, 160-173.

18. S. Linic, P. Christopher, H. Xin and A. Marimuthu, *Acc. Chem. Res.*, 2013, **46**, 1890-1899.

19. D. F. Swearer, H. Zhao, L. Zhou, C. Zhang, H. Robatjazi, J. M. P. Martirez, C. M. Krauter, S. Yazdi, M. J. McClain, E. Ringe, E. A. Carter, P. Nordlander and N. J. Halas, *Proc. Natl. Acad. Sci. U. S. A.*, 2016, **113**, 8916-8920.

20. Y. Zhang, S. He, W. Guo, Y. Hu, J. Huang, J. R. Mulcahy and W. D. Wei, *Chem. Rev.*, 2018, **118**, 2927-2954.

21. M. A. El-Sayed, *Acc. Chem. Res.*, 2001, **34**, 257-264.

22. C. Burda, X. Chen, R. Narayanan and M. A. El-Sayed, *Chem. Rev.*, 2005, **105**, 1025-1102.

23. U. Aslam, V. G. Rao, S. Chavez and S. Linic, *Nat. Catal.*, 2018, **1**, 656-665.

24. Z.-j. Wang, H. Song, H. Liu and J. Ye, *Angew. Chem. Int. Ed.*, 2020, **59**, 8016-8035.

25. S. Rej, L. Mascaretti, E. Y. Santiago, O. Tomanec, Š. Kment, Z. Wang, R. Zbořil, P. Fornasiero, A. O. Govorov and A. Naldoni, *ACS Catal.*, 2020, **10**, 5261-5271.

26. S. Linic, U. Aslam, C. Boerigter and M. Morabito, *Nat. Mater.*, 2015, **14**, 567-576.

27. S. F. Hung, F. X. Xiao, Y. Y. Hsu, N. T. Suen, H. B. Yang, H. M. Chen and B. Liu, *Adv. Energy Mater.*, 2016, **6**, 1501339.

28. J. S. DuChene, B. C. Sweeny, A. C. Johnston-Peck, D. Su, E. A. Stach and W. D. Wei, *Angew. Chem. Int. Ed.*, 2014, **53**, 7887-7891.

29. K. Qian, B. C. Sweeny, A. C. Johnston-Peck, W. Niu, J. O. Graham, J. S. DuChene, J. Qiu, Y.-C. Wang, M. H. Engelhard, D. Su, E. A. Stach and W. D. Wei, *J. Am. Chem. Soc.*, 2014, **136**, 9842-9845.

30. J. Sá, G. Tagliabue, P. Friedli, J. Szlachetko, M. H. Rittmann-Frank, F. G. Santomauro, C. J. Milne and H. Sigg, *Energy Environ. Sci.*, 2013, **6**, 3584-3588.

31. A. Furube, L. Du, K. Hara, R. Katoh and M. Tachiya, *J. Am. Chem. Soc.*, 2007, **129**, 14852-14853.

32. W. Hou, W. H. Hung, P. Pavaskar, A. Goeppert, M. Aykol and S. B. Cronin, *ACS Catal.*, 2011, **1**, 929-936.

33. Z. Zhang, Z. Wang, S.-W. Cao and C. Xue, *J. Phys. Chem. C*, 2013, **117**, 25939-25947.

34. H. Song, X. Meng, Z.-j. Wang, H. Liu and J. Ye, *Joule*, 2019, **3**, 1606-1636.

35. M. J. Kale, T. Avanesian and P. Christopher, *ACS Catal.*, 2013, **4**, 116-128.

36. P. Christopher and M. Moskovits, *Annu. Rev. Phys. Chem.*, 2017, **68**, 379-398.

37. M. J. Kale and P. Christopher, *Science*, 2015, **349**, 587-588.

38. A. O. Govorov, H. Zhang and Y. K. Gun'ko, *J. Phys. Chem. C*, 2013, **117**, 16616-16631.

39. A. Manjavacas, J. G. Liu, V. Kulkarni and P. Nordlander, *ACS Nano*, 2014, **8**, 7630-7638.

40. S. Link and M. A. El-Sayed, *J. Phys. Chem. B*, 1999, **103**, 4212-4217.

41. B. D. Clark, C. R. Jacobson, M. Lou, D. Renard, G. Wu, L. Bursi, A. S. Ali, D. F. Swearer, A.-L. Tsai, P. Nordlander and N. J. Halas, *ACS Nano*, 2019, **13**, 9682-9691.

42. L. Yuan, M. Lou, B. D. Clark, M. Lou, L. Zhou, S. Tian, C. R. Jacobson, P. Nordlander and N. J. Halas, *ACS Nano*, 2020, **14**, 12054-12063.

43. C. Wang and D. Astruc, *Chem. Soc. Rev.*, 2014, **43**, 7188-7216.

44. H. Wang, F. Tam, N. K. Grady and N. J. Halas, *J. Phys. Chem. B*, 2005, **109**, 18218-18222.

45. A. Pinchuk, U. Kreibig and A. Hilger, *Surf. Sci.*, 2004, **557**, 269-280.

46. R. H. Doremus, *J. Chem. Phys.*, 1964, **40**, 2389-2396.

47. M. Ghoussoub, M. Xia, P. N. Duchesne, D. Segal and G. Ozin, *Energy Environ. Sci.*, 2019, **12**, 1122-1142.

48. Z. Xie, Y. Duo, Z. Lin, T. Fan, C. Xing, L. Yu, R. Wang, M. Qiu, Y. Zhang, Y. Zhao, X. Yan and H. Zhang, *Adv. Sci.*, 2020, **7**, 1902236.

49. G. Tas and H. J. Maris, *Phys. Rev. B*, 1994, **49**, 15046-15054.

50. M. L. Brongersma, N. J. Halas and P. Nordlander, *Nat. Nanotechnol.*, 2015, **10**, 25-34.

51. K. Jiang, D. A. Smith and A. Pinchuk, *J. Phys. Chem. C*, 2013, **117**, 27073-27080.

52. C. M. Hessel, V. P. Pattani, M. Rasch, M. G. Panthani, B. Koo, J. W. Tunnell and B. A. Korgel, *Nano Lett.*, 2011, **11**, 2560-2566.

53. S. Linic, P. Christopher and D. B. Ingram, *Nat. Mater.*, 2011, **10**, 911-921.

54. S. Luo, H. Song, D. Philo, M. Oshikiri, T. Kako and J. Ye, *Appl. Catal., B*, 2020, **272**, 118965-118973.

55. E. Cortés, *Adv. Opt. Mater.*, 2017, **5**, 1700191.

56. M. Bonn, S. Funk, C. Hess, D. N. Denzler, C. Stampfl, M. Scheffler, M. Wolf and G. Ertl, *Science*, 1999, **285**, 1042-1045.

57. H. Robatjazi, H. Zhao, D. F. Swearer, N. J. Hogan, L. Zhou, A. Alabastri, M. J. McClain, P. Nordlander and N. J. Halas, *Nat. Commun.*, 2017, **8**, 27.

58. G. Baffou, I. Bordacchini, A. Baldi and R. Quidant, *Light Sci. Appl.*, 2020, **9**, 108.

59. J.-J. Chen, J. C. S. Wu, P. C. Wu and D. P. Tsai, *J. Phys. Chem. C*, 2011, **115**, 210-216.

60. S.-i. Naya, T. Kume, R. Akashi, M. Fujishima and H. Tada, *J. Am. Chem. Soc.*, 2018, **140**, 1251-1254.

61. L. Zhu, M. Gao, C. K. N. Peh and G. W. Ho, *Mater. Horiz.*, 2018, **5**, 323-343.

62. X. Meng, L. Liu, S. Ouyang, H. Xu, D. Wang, N. Zhao and J. Ye, *Adv. Mater.*, 2016, **28**, 6781-6803.

63. G. Liu, X. Meng, H. Zhang, G. Zhao, H. Pang, T. Wang, P. Li, T. Kako and J. Ye, *Angew. Chem. Int. Ed.*, 2017, **56**, 5570-5574.

64. H. Huang, M. Mao, Q. Zhang, Y. Li, J. Bai, Y. Yang, M. Zeng and X. Zhao, *Adv. Energy Mater.*, 2018, **8**, 1702472-1702482.

65. S. Wu, Y. Li, Q. Zhang, Z. Jiang, Y. Yang, J. Wu and X. Zhao, *Energy Environ. Sci.*, 2019, **12**, 2581-2590.

66. H. Huang, M. Mao, Q. Zhang, Y. Li, J. Bai, Y. Yang, M. Zeng and X. Zhao, *Adv. Energy Mater.*, 2018, **8**, 1702472.

67. M. Mao, Q. Zhang, Y. Yang, Y. Li, H. Huang, Z. Jiang, Q. Hu and X. Zhao, *Green Chem.*, 2018, **20**, 2857-2869.

68. S. Yao, X. Zhang, W. Zhou, R. Gao, W.n Xu, Y. Ye, L. Lin, X. Wen, P. Liu, B. Chen, E. Crumlin, J. Guo, Z. Zuo, W. Li, J. Xie, L. Lu, C. J. Kiely, L. Gu, C. Shi, J. A. Rodriguez and D. Ma, *Science*, 2017, **357**, 389-393.

69. O. Lazarus, T. W. Woolerton, A. Parkin, M. J. Lukey, E. Reisner, J. Seravalli, E. Pierce, S. W. Ragsdale, F. Sargent and F. A. Armstrong, *J. Am. Chem. Soc.*, 2009, **131**, 14154-14155.

70. Qi Fu, Howard Saltsburg and M. Flytzani-Stephanopoulos, *Science*, 2003, **301**, 935-938.

71. T.Bunluesin, R.J.Gorte and G.W.Graham, *Appl. Catal., B*, 1998, **15**, 107-114.

72. X. Wang and R. J. Gorte, *Appl. Catal., A*, 2003, **247**, 157-162.

73. L. Zhang, X. Wang, J.-M. M. Millet, P. H. Matter and U. S. Ozkan, *Appl. Catal., A*, 2008, **351**, 1-8.

74. C. Chen, W. Cheng and S. Lin, *Appl. Catal., A*, 2004, **257**, 97-106.

75. Y. Li, Q. Fu and M. Flytzani-Stephanopoulos, *Appl. Catal., B*, 2000, **27**, 179-191.

76. P. O. Graf, D. J. M. de Vlieger, B. L. Mojet and L. Lefferts, *J. Catal.*, 2009, **262**, 181-187.

77. D. Tibiletti, F. Meunier, A. Goguet, D. Reid, R. Burch, M. Boaro, M. Vicario and A. Trovarelli, *J. Catal.*, 2006, **244**, 183-191.

78. M. Shekhar, J. Wang, W. S. Lee, W. D. Williams, S. M. Kim, E. A. Stach, J. T. Miller, W. N. Delgass and F. H. Ribeiro, *J. Am. Chem. Soc.*, 2012, **134**, 4700-4708.

79. T. Shishido, M. Yamamoto, D. Li, Y. Tian, H. Morioka, M. Honda, T. Sano and K. Takehira, *Appl. Catal., A*, 2006, **303**, 62-71.

80. H. Sakurai, A. Ueda, T. Kobayashi and M. Haruta, *Chem.Commun.*, 1997, DOI: 10.1039/a606192c, 271-272.

81. F. Liu, L. Song, S. Ouyang and H. Xu, *Catal. Sci. Technol.*, 2019, **9**, 2125-2131.

82. X. Zhang, X. Li, M. E. Reish, D. Zhang, N. Q. Su, Y. Gutiérrez, F. Moreno, W. Yang, H. O. Everitt and J. Liu, *Nano Lett.*, 2018, **18**, 1714-1723.

83. X. Li, X. Zhang, H. O. Everitt and J. Liu, *Nano Lett.*, 2019, **19**, 1706-1711.

84. M. Gao, P. K. N. Connor and G. W. Ho, *Energy Environ. Sci.*, 2016, **9**, 3151-3160.

85. M. Nielsen, E. Alberico, W. Baumann, H. J. Drexler, H. Junge, S. Gladiali and M. Beller, *Nature*, 2013, **495**, 85-89.

86. S. E. Hosseini and M. A. Wahid., *Renewable Sustainable Energy Rev.*, 2016, **57**, 850-866.

87. J. Goldemberg, *Science*, 2007, **315**, 808.

88. L. N. Chen, K. P. Hou, Y. S. Liu, Z. Y. Qi, Q. Zheng, Y. H. Lu, J. Y. Chen, J. L. Chen, C. W. Pao, S. B. Wang, Y. B. Li, S. H. Xie, F. D. Liu, D. Prendergast, L. E. Klebanoff, V. Stavila, M. D. Allendorf, J. Guo, L. S. Zheng, J. Su and G. A. Somorjai, *J. Am. Chem. Soc.*, 2019, **141**, 17995-17999.

89. D.Teichmann, W. Arlt, P. Wasserscheid and R. Freymann., *Energy Environ. Sci.*, 2011, **4**, 2767-2773.

90. M. D. Marcinkowski, J. Liu, C. J. Murphy, M. L. Liriano, N. A. Wasio, F. R. Lucci, M. Flytzani-Stephanopoulos and E. C. H. Sykes, *ACS Catal.*, 2016, **7**, 413-420.

91. P. Preuster, C. Papp and P. Wasserscheid, *Acc. Chem. Res.*, 2017, **50**, 74-85.

92. Y. H. P. Zhang, *Int. J. Hydrogen Energy*, 2010, **35**, 10334-10342.

93. D. R. Palo, R. A. Dagle and J. D. Holladay, *Chem. Rev.*, 2007, **107**, 3992-4021.

94. C. Mesters, *Annu. Rev. Chem. Biomol. Eng.*, 2016, **7**, 223-238.

95. L. Lin, W. Zhou, R. Gao, S. Yao, X. Zhang, W. Xu, S. Zheng, Z. Jiang, Q. Yu, Y. W. Li, C. Shi, X. D. Wen and D. Ma, *Nature*, 2017, **544**, 80-83.

96. H. Yang, Y. Chen, X. Cui, G. Wang, Y. Cen, T. Deng, W. Yan, J. Gao, S. Zhu, U. Olsbye, J. Wang and W. Fan, *Angew. Chem. Int. Ed.*, 2018, **57**, 1836-1840.

97. H. Jeong, K. I. Kim, T. H. Kim, C. H. Ko, H. C. Park and I. K. Song, *J. Power Sources*, 2006, **159**, 1296-1299.

98. G.-S. Wu, D.-S. Mao, G.-Z. Lu, Y. Cao and K.-N. Fan, *Catal. Lett.*, 2009, **130**, 177-184.

99. Y.-F. Li, X.-F. Dong and W.-M. Lin, *Int. J. Hydrogen Energy*, 2004, **29**, 1617-1621.

100. X. Huang, L. Ma and M. S. Wainwright, *Appl. Catal., A*, 2004, **257**, 235-243.

101. Y. Liu, T. Hayakawa, T. Tsunoda, K. Suzuki, S. Hamakawa, K. Murata, R. Shiozaki, T. Ishii and M. Kumagai, *Top. Catal.*, 2003, **22**, 205-213.

102. R. Song, B. Luo, J. Geng, D. Song and D. Jing, *Ind. Eng. Chem. Res.*, 2018, **57**, 7846-7854.

103. Z. Sun, S. Fang, Y. Lin and Y. H. Hu, *Chem. Eng. J.*, 2019, **375**, 121909-121917.

104. X. Han, L. Song, H. Xu and S. Ouyang, *Catal. Sci. Technol.*, 2018, **8**, 2515-2518.

105. L. Lin, Q. Yu, M. Peng, A. Li, S. Yao, S. Tian, X. Liu, A. Li, Z. Jiang, R. Gao, X. Han, Y.-w. Li, X.-d. Wen, W. Zhou and D. Ma, *J. Am. Chem. Soc.*, 2021, **143**, 309-317.

106. A. Haryanto, S. Fernando, N. Murali and S. Adhikari, *Energy & Fuels*, 2005, **19**, 2098-2106.

107. Z. Chai, T. T. Zeng, Q. Li, L. Q. Lu, W. J. Xiao and D. Xu, *J. Am. Chem. Soc.*, 2016, **138**, 10128-10131.

108. G. Giannakakis, A. Trimpalis, J. Shan, Z. Qi, S. Cao, J. Liu, J. Ye, J. Biener and M. Flytzani-Stephanopoulos, *Top. Catal.*, 2018, **61**, 475-486.

109. M. Ni, D. Y. C. Leung and M. K. H. Leung, *Int. J. Hydrogen Energy*, 2007, **32**, 3238-3247.

110. J. Shan, N. Janvelyan, H. Li, J. Liu, T. M. Egle, J. Ye, M. M. Biener, J. Biener, C. M. Friend and M. Flytzani-Stephanopoulos, *Appl. Catal., B*, 2017, **205**, 541-550.

111. J. Shan, J. Liu, M. Li, S. Lustig, S. Lee and M. Flytzani-Stephanopoulos, *Appl. Catal., B*, 2018, **226**, 534-543.

112. Z.-T. Wang, R. A. Hoyt, M. El-Soda, R. J. Madix, E. Kaxiras and E. C. H. Sykes, *Top. Catal.*, 2017, **61**, 328-335.

113. M. C. Sanchez-Sanchez, R. M. Navarro Yerga, D. I. Kondarides, X.n E. Verykios and J. L. G. Fierro, *J. Phys. Chem. A*, 2010, **114**, 3873-3882.

114. J. Sun, A. M. Karim, D. Mei, M. Engelhard, X. Bao and Y. Wang, *Appl. Catal., B*, 2015, **162**, 141-148.

115. J. M. Conesa, M. V. Morales, C. López-Olmos, I. Rodríguez-Ramos and A. Guerrero-Ruiz, *Appl. Catal., A*, 2019, **576**, 54-64.

116. F.-W. Chang, H.-C. Yang, L. S. Roselin and W.-Y. Kuo, *Appl. Catal., A*, 2006, **304**, 30-39.

117. Yao-Jen Tu and Y.-W. Chen, *Ind. Eng. Chem. Res.*, 2001, **40**, 5889-5893.

118. Z.-T. Wang, R. A. Hoyt, M. El-Soda, R. J. Madix, E. Kaxiras and E. C. H. Sykes, *Top. Catal.*, 2018, **61**, 328-335.

119. Q.-N. Wang, L. Shi and A.-H. Lu, *ChemCatChem*, 2015, **7**, 2846-2852.

Chapter 2 Solar-driven methanol self-coupling to produce hydrogen and methyl formate over plasmonic Cu nanoparticles with optimized size

2.1 Introduction

Hydrogen is regarded as a critical and indispensable chemical building block to be utilized in various industrial processes, such as hydrogenation reaction and fuel cells.[1-3] Because of the internal nature of hydrogen, it is remaining technical and economic challenges to transport and store the hydrogen in an efficient and reliable way, hindering the large-scale application of elemental hydrogen in the future energy sector.[4, 5] Recent scientific and technological achievements suggested that the hydrogen can be handled in the form of chemical bond from liquid organic hydrogen carrier (LOHC), and on-demand hydrogen production can be realized through activating certain chemical bonds of LOHC in the presence of catalysts.[6-8] Considering the high H_2 gravimetric density (18.8% by weight) and the mild H_2 release condition, the methanol is regarded as one of the most promising LOHC candidate.[9-11] The non-oxidative and dry (in the absence of water molecules) methanol self-coupling (MSC) has attracted considerable attention from both the scientific and industrial area.[12] During the MSC, the methanol molecules can be converted into hydrogen and another value-added chemical (methyl formate) simultaneously, and the resulting methyl formate is a critical intermediate for the synthesis of various valuable industrial chemicals including carboxylic acids, ethylene glycol, formic acid and formamides.[13]

The pioneering works have demonstrated that Cu-based materials exhibited good selectivity for the thermocatalytic methanol self-coupling reaction (MSC),[14] and substantial efforts have been devoted to modifying Cu-based catalysts for promoting the activity and stability.[15] For instance, Fan and co-authors developed mesoporous silica shell coated Cu nanoparticles for the dehydrogenation of methanol into methyl formate, and the authors proposed that methyl formate was formed through the reaction of CH_3O and HCHO over Cu^0 sites.[16] Yuan and co-authors supposed that the introduction of Pd into the Cu-MgO catalysts could prevent the deactivation and improve the catalytic activity.[17] Despite an excellent catalytic activity that can be achieved over Cu-based catalysts, tremendous energy input in conventional thermocatalytic MSC is still an

obstacle for the large-scale applications, since high reaction temperature (approximately 200-250 °C) is indispensably required for achieving satisfactory activity. Under such circumstances, it is of great significance to develop a cost-effectiveness catalytic technology using a sustainable energy supply for catalyzing MSC.

An innovative and sustainable strategy for initiating the catalytic reactions is to utilize the solar energy as the energy input.[18-20] Very recently, plasmonic nanostructures, which can harness and convert the solar-energy into energetic hot carriers and photothermal heat synergistically through the excitation of localized surface plasmon resonance (LSPR), have emerged as promising photocatalysts for achieving highly-efficient catalytic activity.[19, 21, 22] In a plasmonic photothermal catalytic process, photo-induced hot carriers can interact with adsorbates via injecting charge carriers into antibonding orbitals on the surface of excited plasmonic nanoparticles, providing an alternative reaction mechanism by modifying the reaction pathway.[23, 24] Meanwhile, the photothermal heat can serve as another stimulus for further accelerating the surface chemical reaction.[25] Through the interaction between surface adsorbates and energetic hot carriers produced from plasmonic metals after light excitation, surface catalytic reaction can be initiated efficiently and selectively.[26-28] For instance, Halas and co-authors reported the Al@Cu_2O plasmonic catalysts, which combined the plasmonic light harvesting (Al) and active sites (Cu_2O) together for achieving efficient plasmonic reverse water gas shift reaction.[29] In such configuration, hot carriers produced by the plasmonic Al were transferred to the Cu_2O, followed by injection into unoccupied states of CO_2 adsorbed on the surface of Cu_2O for C-O bond activation, initiating the reverse water gas shift reaction.

In general, the LSPR effect of plasmonic nanometals were strongly governed by its size and shape.[30, 31] By modulating the geometry of plasmonic metals, catalytic activity can be promoted effectively.[32-34] These phenomena can be attributed to the fact that a shift in the electric field density was induced by modifying the morphology of plasmonic nanostructures, which changes the oscillation frequency of the electrons, and therefore inducing different cross-section of the LSPR properties.[35] Qian and co-authors proved that increasing the size of Au plasmonic nanoparticles can significantly increase the light scattering, ultimately affecting the reduction potential.[36] Ye and co-authors designed plasmonic Ni nanoparticles with different size distributions for light-assisted methane dry reforming reaction.[37] The results suggested that the photo-enhancement of the catalytic activity was strongly governed by the size distribution of Ni nanoparticles, and the Ni

nanoparticles with smaller size demonstrated higher light-enhancement. Mechanistic investigation results indicated that the LSPR effect played dominant role in the Ni nanoparticles with smaller size, whereas the interband transition played increased role in enhancing the activity over Ni nanoparticles with larger size.

Above studies revealed that in order to increase the production of hot carriers from plasmon decay, the size of the plasmonic nanostructures needs to be carefully modulated.[38] However, in the conventional thermocatalytic process, nanometals with smaller size are more favorable for the surface catalytic reaction, which can be attributed to a larger surface area and more coordinatively unsaturated surface atoms are induced by nanometals with smaller diameter, exposing more active sites which can participate in the surface reaction.[39-41] Under such circumstance, when constructing plasmonic catalysts with both the thermocatalytic activity and plasmonic effect for driving the catalytic reaction under light irradiation, the size of plasmonic nanometals should be considered systematically.

In this chapter, Cu nanoparticles with different mean diameters were synthesized, and were applied in photo-enhanced thermocatalytic methanol self-coupling reaction for the selective production of hydrogen and methyl formate. It was discovered that the light absorption property could be modulated by changing the diameter of Cu nanoparticles, which ultimately controlled their photocatalytic activity. As a result, the optimized Cu sample (3-Cu) with an average diameter of 34.8 nm demonstrated the best photo-enhanced activity towards MSC among all samples. At a reaction temperature of 180 °C with the visible light irradiation, a H_2 production rate of 2358 μmol g^{-1} min^{-1} was achieved, which was 7.5 times higher than that under dark condition at same reaction temperature. Mechanistic investigation revealed that the photo-induced hot carriers over Cu nanoparticle played dominant role in the catalytic enhancement under light irradiation. Furthermore, solar-driven MSC reaction without the additional thermal energy input was conducted to evaluate the catalytic performance over 3-Cu. The results showed that 3-Cu sample with optimized thermocatalytic activity and plasmonic effect could achieve a H_2 production rate of 4318 μmol g^{-1} min^{-1} under the irradiation of concentrated solar light (933 mW cm^{-2}), and a solar-energy conversion efficiency up to 3.6% was achieved. Our findings provide a feasible strategy of manipulating LSPR effect simply by varying the size of Cu nanoparticles, and is expected to greatly facilitate the design of plasmonic photocatalysts for solar-energy conversion.

2.2 Experimental section

2.2.1 Materials preparation

Cu nanoparticles were synthesized by using the wet chemistry method. Accordingly, 0.1M (10 mL) ascorbic acid (L(+)-Ascorbic acid, Wako, 99 % purity, CAS: 50-81-7) solution was added into a mixed aqueous solution (100 mL) of Cu $(NO_3)_2 \cdot 3H_2O$ (Copper nitrate trihydrate, Wako, 99 % purity, CAS: 10031-43-3) and different amount of PVP (Polyvinylpyrrolidone, Sigma-Aldrich, CAS: 9003-39-8). Afterward, 0.1M (10 mL) of $NaBH_4$ (Sodium tetrahydroborate, Wako, 95 % purity, CAS: 16940-66-2) was drop-wisely added into the solution. The solution was stirred continuously at room temperature in the Ar atmosphere to prevent the oxidation of Cu. 500 mg of SiO_2 (Silicon dioxide, Wako, 99.9 % purity, CAS: 7631-86-9) was then added into the solution, under continuous stirring to form a homogeneous dispersion. After stirred for 1 h, the solid was collected and washed by ethanol and water three times, followed by drying in a vacuum oven in 70 °C overnight and calcination in the air at 350 °C for 4 h. The sample was reduced in hydrogen (10 % in Ar) at 350 °C for 3 h to prepare SiO_2 supported metallic Cu nanoparticle. For comparison, original Cu nanoparticles without adding PVP were also synthesized.

2.2.2 Material characterization

The crystalline structures of the catalysts were characterized using an X-ray powder diffractometer with Cu Kα radiation (PANalytical). The surface electronic states of catalysts were investigated by X-ray photoelectron spectroscopy (XPS, Escalab 250 Xi, Thermo Scientific). UV-Vis absorption spectra of catalysts were collected by a spectrophotometer (UV-2600, Shimadzu). Transmission electron microscopy (TEM) and high-resolution TEM (HRTEM) measurements were carried out on the FEI TECNAI G2 F30 instrument. The specific surface areas were determined using a surface area analyzer (Quantachrome, USA) by the Brunauer-Emmett-Teller (BET) method. Light intensity and wavelength distribution of the illuminant were analyzed by the USR-40 spectrophotometer.

2.2.3 Photocatalytic activity measurement

Two different types of reactors (photo-assisted thermal catalysis reactor and solar-driven catalysis reactor) were utilized to manifest the reaction mechanism and solar-

driven catalytic activity, respectively. In order to elucidate the reaction mechanism, photo-assisted thermal catalytic MSC was conducted under atmospheric pressure in a homemade flow-bed reactor (diameter: 8.5 mm), as shown in Figure 2.1. A quartz window was equipped on the reactor to allow the irradiation of visible light to the catalysts. LA-251 Xe lamp with HA30 and L42 filters (to remove the infrared and ultra-violate light) was employed to provide the photon energy (Figure 2.2). The thermocouple and temperature controller (TC-1000, JASCO) were utilized to keep the catalysts at the desired temperature. Heat induced by light irradiation was mitigated by the temperature controller. Typically, 5 mg of catalysts were dispersed in the reaction cell uniformly. Prior to the activity measurement, the catalysts were *in-situ* reduced in the reactor at 350 °C for 1 h under a flow of hydrogen (10% in Ar), then cooling down to the room temperature. Subsequently, the reactor was flushed with pure Ar gas for 30 min to remove the hydrogen in the reactor. The reaction gas was introduced into the reactor at a flow rate of 50 mL min^{-1} through the bubbler system. The products were quantified by gas chromatography (GC) equipped with thermal conductivity and flame ionization detector.

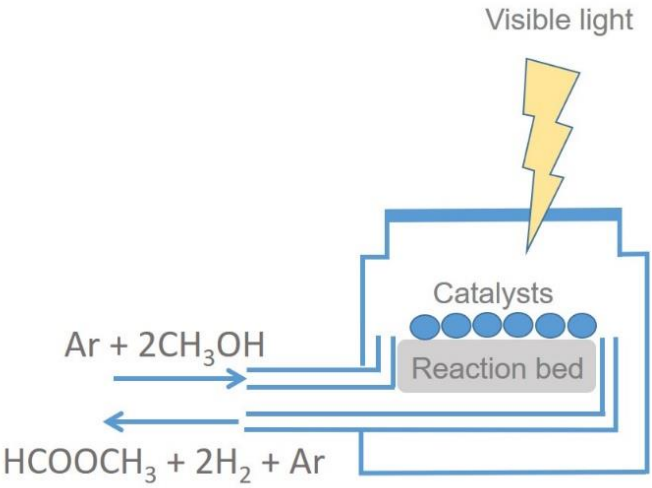

Figure 2.1 Schematic diagram of home-made photo-thermocatalytic reaction system.

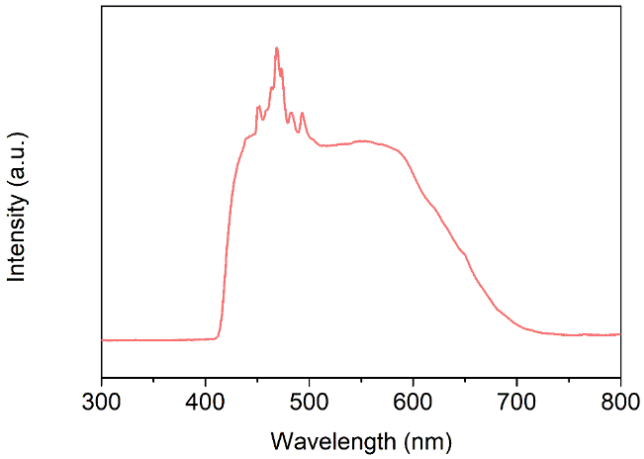

Figure 2.2 Output irradiance of the visible light in the photo-assisted thermal catalytic reaction.

Solar-driven methanol dehydrogenation reaction was conducted in a home-made flow-type reactor (diameter 10 mm) with quartz cover to allow the irradiation of light to catalysts (Figure 2.3). In this measurement, the AM 1.5 light was employed as the illuminant, and no external thermal energy was applied. A maximum light intensity of 933 mW cm^{-2} was achieved by the optical lens (Figure 2.4). A thermocouple was utilized to test the surface temperature of catalysts. Prior to the activity measurement, the catalysts (10 mg) were reduced at 350 °C for 1 h under a flow of hydrogen (10% in Ar), then dispersed in the reaction cell uniformly after cooling down to the room temperature. Through a bubbler system, the reaction gas was introduced into the reactor. The space velocity was controlled to be 50 mL min^{-1} unless otherwise specified. The product measurement method was as same as the photo-assisted thermal catalytic reaction.

The solar energy conversion efficiency was calculated using

$$\eta = \frac{\alpha(mol \cdot s^{-1}) \cdot \Delta H^0_{MSC}(J \cdot mol^{-1})}{light\ power\ (J \cdot s^{-1})} \times 100\%,$$

where ΔH^0_{MSC} (73.1 kJ mol^{-1}) is the standard reaction enthalpy changes of methanol self-coupling reaction.

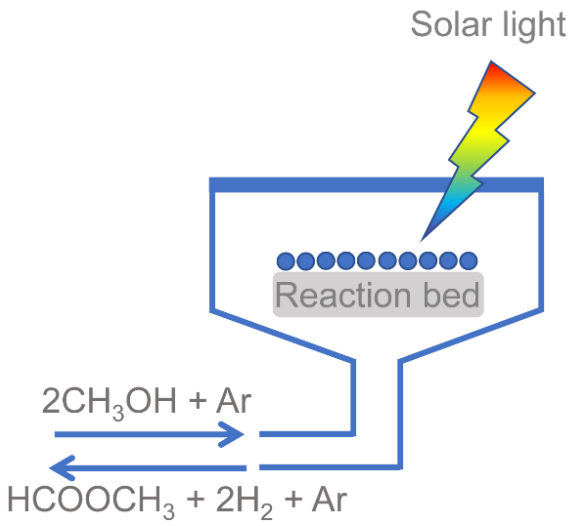

Figure 2.3 Schematic illustration of home-made solar-driven reaction system.

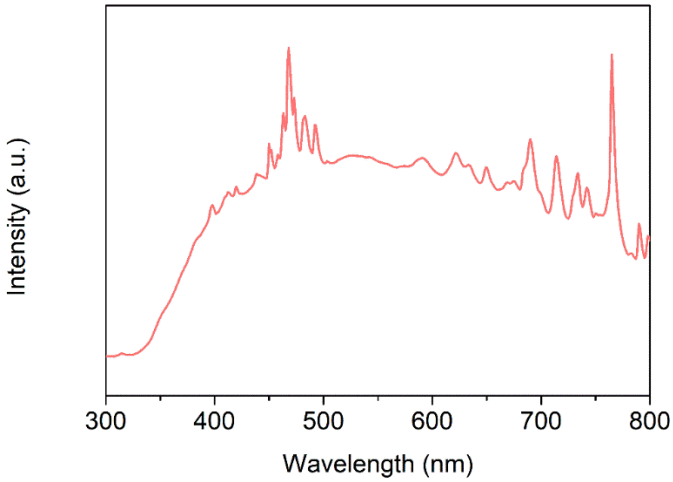

Figure 2.4. Output irradiance of simulated solar light in the solar-driven catalytic reaction.

2.2.4 Finite difference time domain (FDTD) simulation

The spatial distribution of the electric fields around the plasmonic Cu nanoparticles with different diameter were calculated by means of the finite difference time domain (FDTD) method using the FullWAVE software (RSoft, Synopsys). The dielectric functions of Cu was obtained from the literature.[42, 43]

2.3 Results and discussion

2.3.1 Catalyst characterization

The Cu nanoparticles with different mean sizes were synthesized by changing the PVP amount during the fabrication process, and the transmission electron microscopy (TEM) images were collected to investigate the size distribution of as-synthesized Cu nanoparticles. Figure 2.5 showed the representative TEM images of four Cu nanoparticle samples with different average diameters. From TEM images, it can be observed that the as-prepared Cu nanoparticle were spherical in shape (Figure 2.5), and a clear lattice fringe with interplanar distance of 0.21 nm was observed, which was in good agreement with the (111) plane of Cu (Figure 2.6). The Cu nanoparticles synthesized without adding PVP (named as 1-Cu hear and after) showed a mean size of 7.8 nm (Figure 2.5 a and Figure 2.7 a). The average diameters of Cu nanoparticles were increased after PVP addition, and were measured to be 11.5, 34.8, and 54.7 nm (named as 2-Cu, 3-Cu, and 4-Cu, here and after) (Figure 2.7).

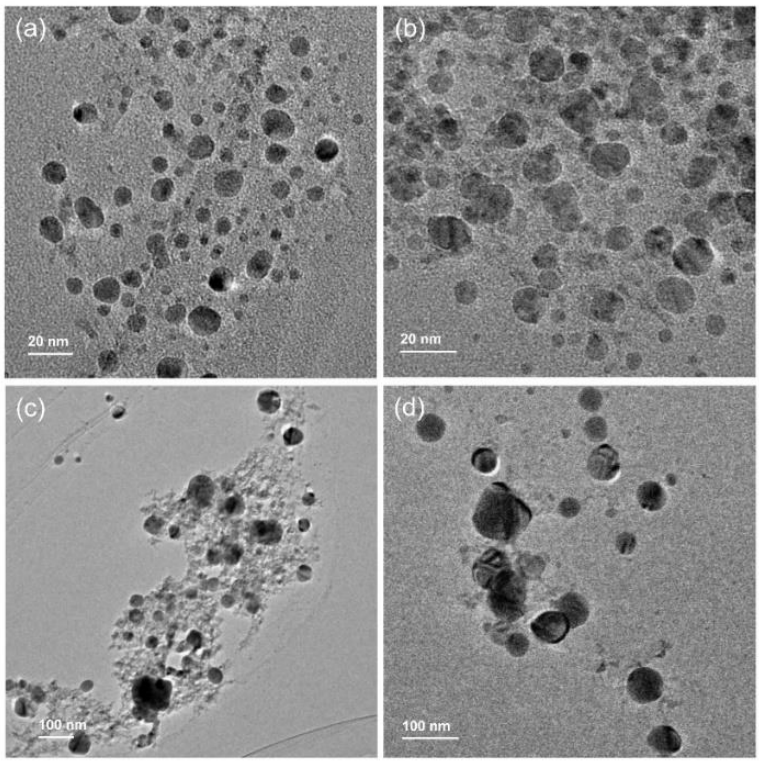

Figure 2.5 TEM characterization of Cu nanoparticles with different average diameters. (a) 1-Cu. (b) 2-Cu. (c) 3-Cu. (d) 4-Cu.

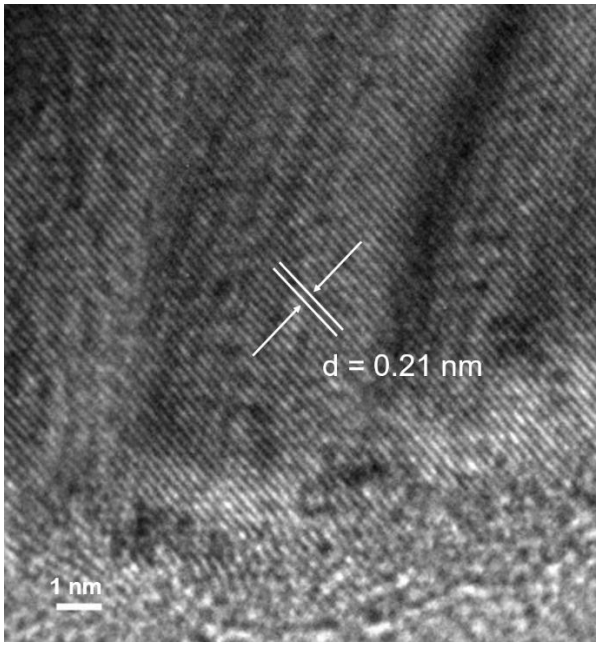

Figure 2.6 High resolution TEM image of 3-Cu sample.

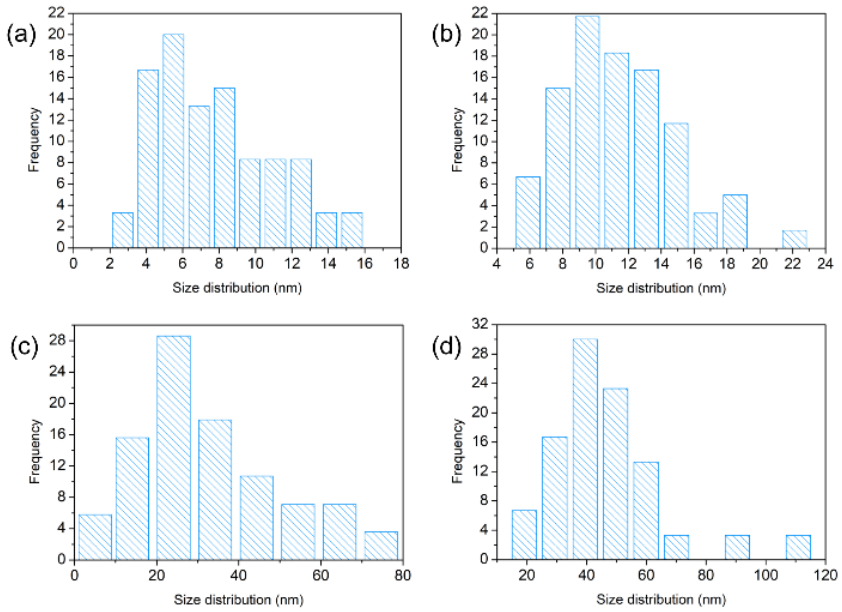

Figure 2.7 Size distribution of Cu nanoparticles with different average diameter from TEM measurement. (a) 1-Cu. (b) 2-Cu. (c) 3-Cu. (d) 4-Cu.

The optical absorption property was investigated by using UV-Vis absorption spectra, and the results indicated that all the Cu nanoparticles exhibited strong LSPR absorption peaks in the visible region (Figure 2.8). As shown in Figure 2.8a, 1-Cu samples demonstrated a strong light absorption peak at 550 nm. Increasing the average particle

size can induce a red-shift of the LSPR absorption peak. The 2-Cu, 3-Cu, and 4-Cu samples showed the light absorption peak at 560, 567, and 580 nm, respectively (Figure 2.8b-d), in good agreement with their size distribution. Increasing the PVP amount reduced the specific surface area, further verifying that the Cu nanoparticles with larger mean diameters were fabricated (Table 2.1). Clearly, the size of Cu nanoparticles increased gradually after PVP addition, from quite small size (approximately 7.8 nm without adding PVP) to large size (approximately 54.7 nm).

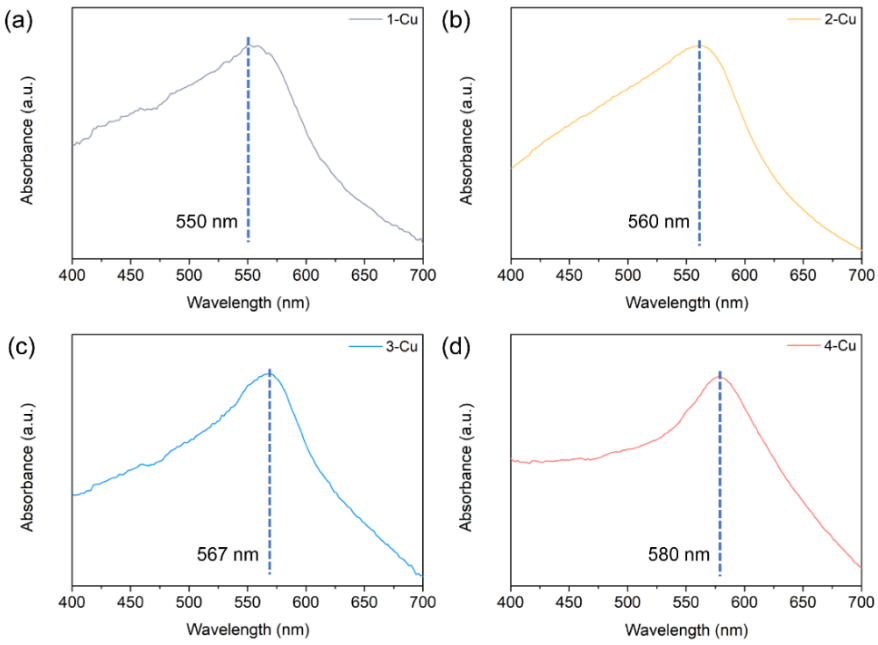

Figure 2.8 UV-VIS absorption spectra of Cu nanoparticles with different size distribution. (a) 1-Cu. (b) 2-Cu. (c) 3-Cu. (d) 4-Cu.

Table 2.1 Physicochemical properties of the catalysts.

Samples	S_{BET} (m^2 g^{-1})[a]	LSPR peak (nm)	Mean size (nm)[b]
1-Cu	188.3	550	7.8
2-Cu	180.3	560	11.5
3-Cu	166.8	567	34.8
4-Cu	147.1	580	54.7

a, obtained by N_2 adsorption-desorption method through Brunauer-Emmett-Teller (BET) equation;

b, determined by TEM.

X-ray diffraction (XRD) patterns were employed to investigate the crystalline structure of the catalysts, and the results showed that all the samples exhibited the characteristic peaks centered at 43.3°, 50.4°, and 74.1°, which could be assigned to metallic Cu, indicating that the Cu nanoparticles were synthesized (Figure 2.9a). Cu nanoparticles with larger average diameters demonstrated stronger intensity of the characteristic diffraction peaks due to their better crystallinity. The X-ray photoelectron spectroscopy (XPS) measurements were carried out to determine the surface electronic states of the 3-Cu catalyst. In the Cu 2p spectra, a Cu $2p_{3/2}$ peak was detected at 933.0 eV, proving that the Cu was in the metallic state. Satellite peaks of Cu^{2+} could not be observed in the Cu 2p spectra, indicating the absence of Cu_2O or CuO in 3-Cu catalysts (Figure 2.9b).[44] In order to get more convincing evidence for the valence state of Cu in 3-Cu catalysts, the XPS Auger peaks were recorded. The Cu $L_3M_{45}M_{45}$ spectrum showed a clear peak at the kinetic energy of 918.6 eV, which strongly indicated that the Cu in 3-Cu catalyst was in metallic state (Figure 2.9c).[45] Above characterization results verified that the Cu nanoparticles were synthesized successfully, and the Cu element was in metallic state.

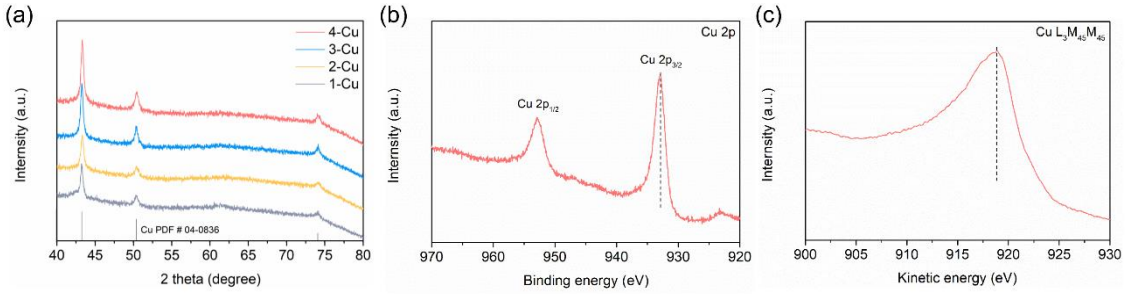

Figure 2.9 (a) XRD patterns of Cu nanoparticles with different mean sizes. (b) XPS Cu 2p spectra of 3-Cu catalysts. (c) XPS Auger spectrum of Cu $L_3M_{45}M_{45}$ over 3-Cu catalysts.

2.3.2 Visible light-enhanced catalytic activity

Visible light-assisted thermocatalytic MSC was performed on a flow-bed reactor under atmospheric pressure to evaluate the performance of plasmonic Cu nanoparticles with different mean diameters. The influence of ultraviolet and infrared light was ruled out by the light filters (L42 and HA30), and the visible light ($420 < \lambda < 800$ nm) with an intensity of approximately 617 mW cm^{-2} was used in the measurement. Photo-induced heat was mitigated by the reactor. Figure 2.10a demonstrated the reaction rate of H_2 production over Cu with different mean sizes under a reaction temperature of 180 °C with and

without the irradiation of visible light. At the reaction temperature of 180 °C without the irradiation of visible light, 1-Cu demonstrated the best performance towards thermocatalytic MSC among all the samples, and a H_2 production rate of 581 μmol g^{-1} min^{-1} was achieved, which could be attributed to the smaller particle size of Cu can expose more active sites for surface reaction. Increasing the diameter of Cu nanoparticles reduced the thermocatalytic activity towards MSC, probably due to the size increment reduced the number of coordinatively unsaturated Cu surface active sites, leading to a decrease in activity (Figure 2.10a). After introducing light-energy into the reaction system, the reaction rates of different Cu samples were higher than that in the dark condition (Figure 2.10a). It was noteworthy that the catalytic activity under light irradiation was varied with particle size, and the optimum sample (3-Cu) showed a H_2 production rate of 2358 μmol g^{-1} min^{-1} with the light irradiation at a reaction temperature of 180 °C, which was significantly higher than that of 1-Cu sample (Figure 2.10a). The photo enhancement of the catalysts was calculated (reaction rate at light condition divided by the rate at dark condition), and the results showed that the 1-Cu, 2-Cu, 3-Cu, and 4-Cu demonstrated the photo enhancement of 2.2, 4.6, 7.5, and 4.2 times, indicating that the optimum sample was 3-Cu (Figure 2.10b).

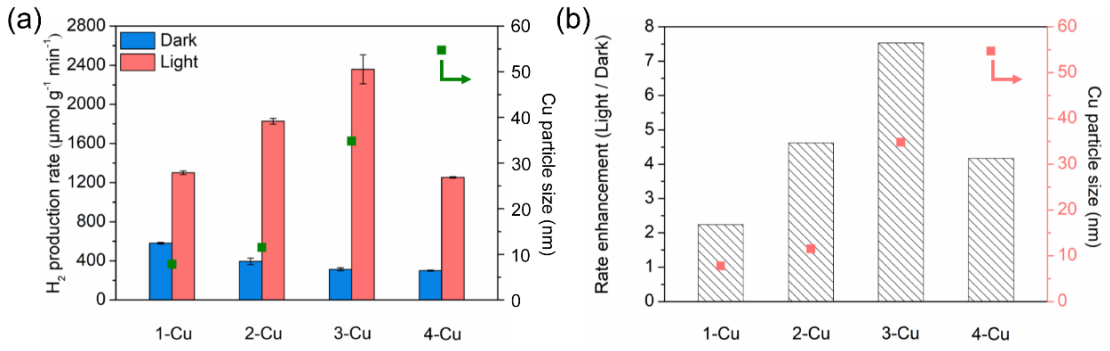

Figure 2.10 Visible light-enhanced catalytic activity. (a) MSC activity at a reaction temperature of 180 °C with and without visible light irradiation over Cu catalysts with different size distribution. (b) Rate enhancement at a reaction temperature of 180 °C with and without visible light irradiation over Cu catalysts with different size distribution.

The photo-assisted thermocatalytic activity over Cu catalysts with different size distributions were systematically evaluated to elucidate the catalytic performance under different reaction condition. Figure 2.11 showed the reaction rate of H_2 production over different Cu catalysts as a function of temperature under the thermocatalytic condition

with and without the irradiation of visible light. Under purely thermal conditions (dark), H_2 production rates over 2-Cu, 3-Cu, and 4-Cu were elevated with the increasing reaction temperature (Figure 2.11b-d), whereas the 1-Cu deactivated even in a short reaction time (30 min) which might relate to the severe aggregation of Cu nanoparticles with small particle size (Figure 2.11a). Subsequently, the reaction rates under different reaction conditions were measured over 2-Cu, 3-Cu, and 4-Cu. A H_2 production rate of 94 μmol g^{-1} min^{-1} was measured over 2-Cu catalysts at the reaction temperature of 140 °C, and the production rate was increased exponentially with the reaction temperature, reaching 395 μmol g^{-1} min^{-1} at the reaction temperature of 180 °C (Figure 2.11b). Increasing the particle size of Cu slightly decreased the thermocatalytic activity towards MSC. 3-Cu exhibited a H_2 production rate of 56 μmol g^{-1} min^{-1} under the reaction temperature of 140 °C, and the activity was increased to 313 μmol g^{-1} min^{-1} with the increasing reaction temperature to 180 °C (Figure 2.11c), whereas the 4-Cu only showed a H_2 production rate of 301 μmol g^{-1} min^{-1} at the reaction temperature of 180 °C (Figure 2.11d). These results indicated that the average diameter of Cu nanoparticle played an important role in determining the reaction rate under purely thermocatalytic condition.

Furthermore, the visible light energy can serve as additional energy input to facilitate the MSC effectively over Cu catalysts. After the introduction of visible light into the reaction system, the reaction rates of 2-Cu, 3-Cu, and 4-Cu catalysts were consistently higher than that in the dark condition, but the enhancement was varied with particle size of Cu. Under the light conditions at the reaction temperature of 180 °C, 2-Cu catalysts presented H_2 production rate of 1827 μmol g^{-1} min^{-1} (Figure 2.11b), while the 3-Cu catalysts demonstrated a H_2 production rate of 2358 μmol g^{-1} min^{-1} (Figure 2.11c). Further increasing the particle size of Cu could reduce the photo-enhanced catalytic activity, as shown in Figure 2.11d, 4-Cu only exhibited a reaction rate of 1253 μmol g^{-1} min^{-1} at a reaction temperature of 180 °C with the visible light irradiation. Above results demonstrated that both the thermocatalytic activity and plasmonic effect contributed to the overall reaction activity. Under purely thermocatalytic condition, the catalytic activities demonstrated a negative correlation with the size of Cu nanoparticles, which could be attributed to that more surface active sites can be exposed the Cu nanoparticles with smaller size. Under photo-assisted thermocatalytic condition, the 3-Cu with a mean diameter of 34.8 nm was optimal among other samples. I speculate that the bigger particle

sizes of Cu nanoparticle could possess stronger capacity for light harvesting, and can convert the light energy into hot carriers effectively for facilitating the catalytic reaction.

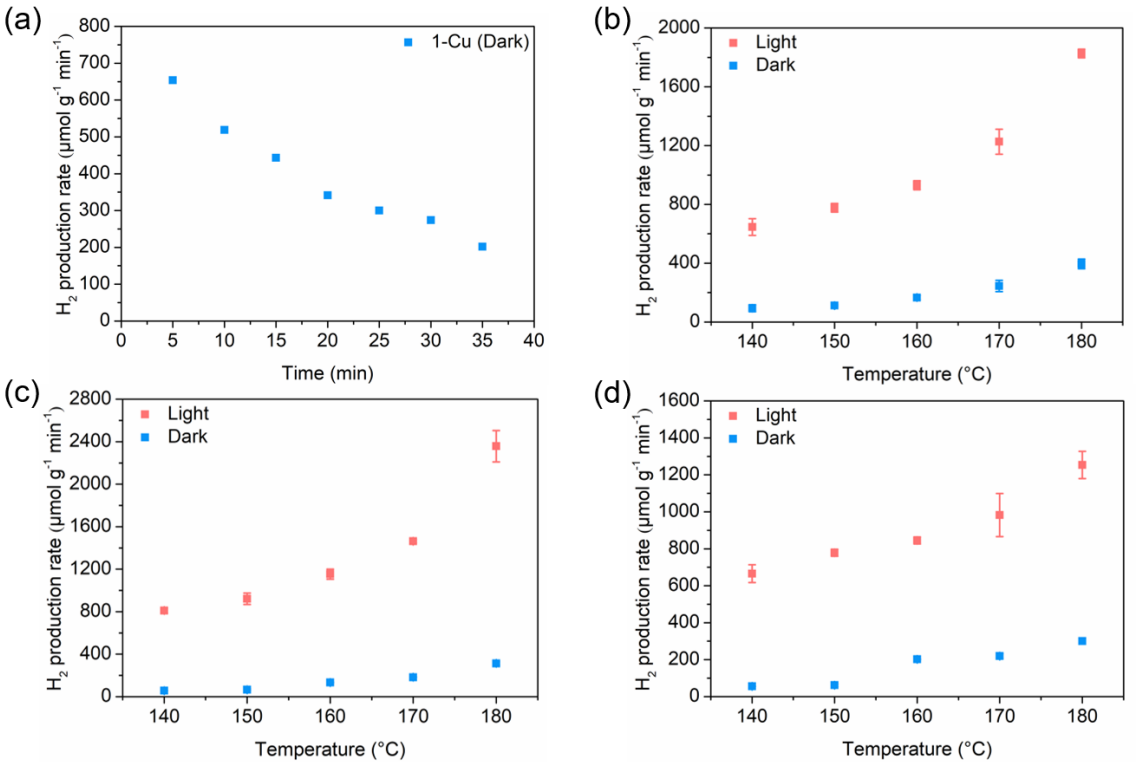

Figure 2.11 Stability test of 1-Cu (a) and MSC activity over 2-Cu, 3-Cu, and 4-Cu samples as a function of temperature in the purely thermal condition and under visible light illumination (b-d).

2.3.3 Reaction role of visible light towards MSC

To understand the mechanism of the observed rate enhancement induced by visible light irradiation in MSC reaction over 3-Cu, I performed a series of fundamental investigations. Steady-state H_2 production rate at a temperature of 180 °C revealed that the photo-enhanced MSC over 3-Cu catalyst was light-sensitive, since the reaction rate increased from approximately 300 μmol g^{-1} min^{-1} to 2400 μmol g^{-1} min^{-1} after the visible light was introduced into the reaction system, and it dropped back to 300 μmol g^{-1} min^{-1} level when the illumination was blocked (Figure 2.12). I suppose that the observed photo-enhancement in the catalytic activity was mainly resulted from the hot carrier-induced reactants activation. To verify this assumption, visible light intensity dependent H_2 production activity (Figure 2.13) was carried out to evaluate the activity under the irradiation of different light intensity at the reaction temperature of 180 °C. Generally,

the linear dependence between the catalytic activities and light intensities indicates that the enhancement of catalytic activity is attributed to the photo-induced charge carriers, which can be attribute to the generation rate of the hot carrier that increases linearly with the photon flux.[20, 23, 46, 47] The results showed that the H_2 production rate presented a linear dependence on light intensity, validating that the reaction was facilitated by the photo-induced hot carriers (Figure 2.13).

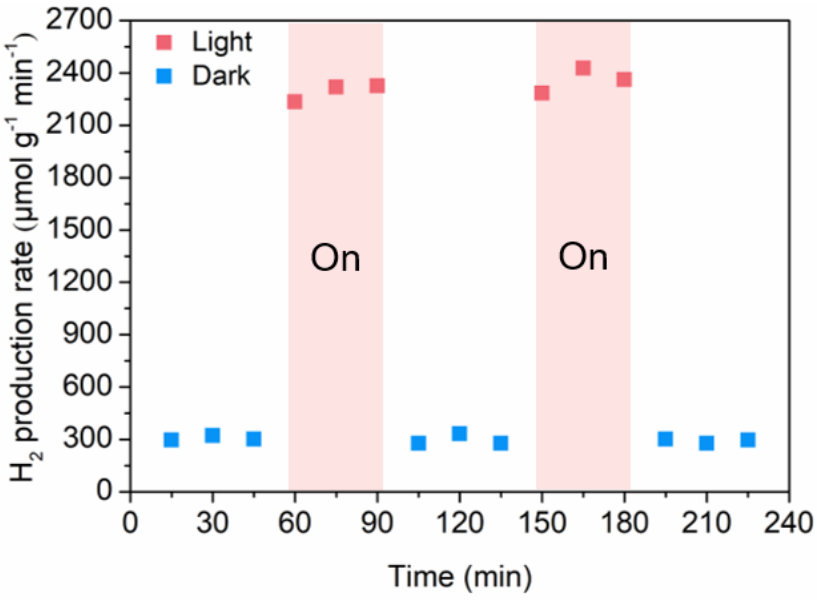

Figure 2.12 MSR activity over 3-Cu catalysts with and without visible light irradiation at a reaction temperature of 180 °C.

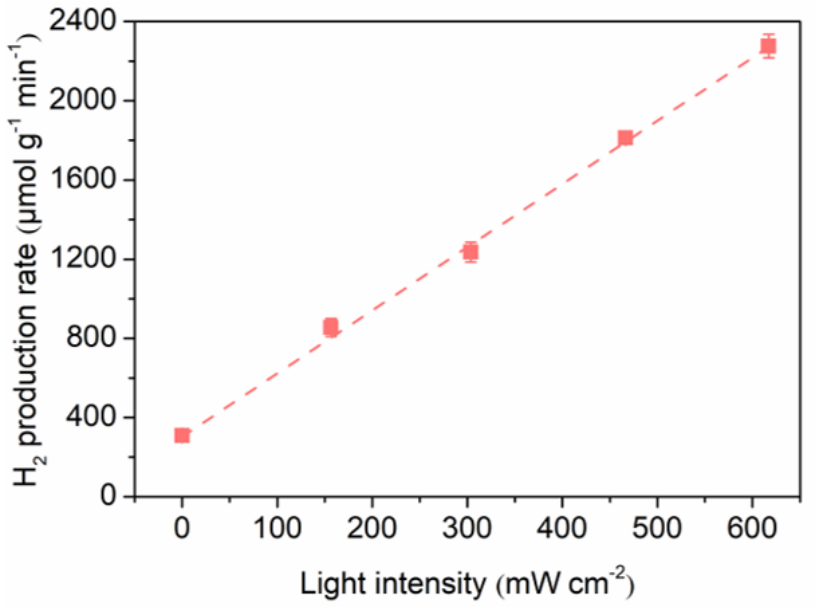

Figure 2.13 Dependence of reaction rate of 3-Cu on light intensity at reaction temperature of 180 °C.

To understand the underlying reaction mechanism, the reaction kinetics of MSC reaction over 3-Cu catalyst under dark condition and with light irradiation were investigated experimentally in the reaction temperature from 140 to 180 °C. The apparent activation energy was calculated by fitting the measured reaction rate (r) with Arrhenius equation (ln r = - Ea/RT + ln A). With the assistance of photo-induced hot carriers, the apparent activation energy over 3-Cu catalyst decreased from 69.22 kJ mol^{-1} to 40.18 kJ mol^{-1}, demonstrating that photo-induced hot carriers can stimulate the MSC efficiently (Figure 2.14).

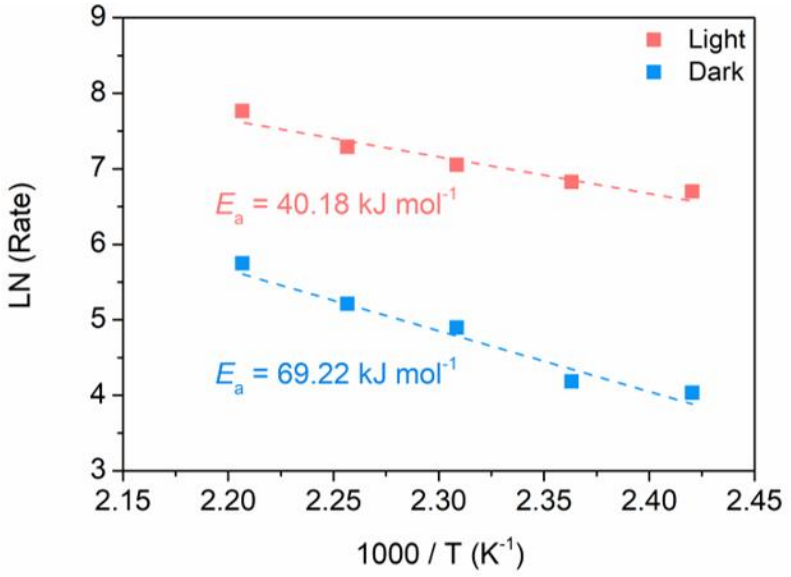

Figure 2.14 Arrhenius plots for H_2 production rate under dark and light conditions over 3-Cu catalysts.

To investigate the underlying reaction mechanism of the visible-light promoted methanol self-coupling reaction over plasmonic Cu nanoparticles with different size distributions, the finite difference time domain (FDTD) simulations were carried out to simulate the intensity and distribution of electric field of catalysts. Figure 2.15 displayed the electric field distribution of plasmonic Cu nanoparticles with different mean sizes under light irradiation at the wavelength 570 nm (the LSPR peak of Cu). In each simulation, the distance between two plasmonic Cu nanoparticles was set to be 2 nm. The results showed that an amplified electric field on the surface of each Cu nanoparticles was observed clearly under the light irradiation. As shown in Figure 2.15a, the maximum field enhancement of 2.3 was observed on the 1-Cu sample (diameter: 7.8 nm) under light

irradiation. These amplified electric fields can trigger the excitation of hot carriers capable of enhancing the catalytic reactions by activating certain chemical bonds of adsorbates.[33] Increasing the diameter of plasmonic Cu nanoparticles resulted in the increased electric fied intensity. As shown in Figure 2.15c, a considerable higher intensity of electric field (amounted to 10.7) can be observed on the surface of 3-Cu. The Cu sample with the biggest average diameter (54.7 nm, 4-Cu) demonstrated a maximum field enhancement of 58.2, indicating that the a larger accumulated plasmonic effect was provided by plasmonic Cu nanoparticles with bigger mean size. These results suggested that abundant hot electrons can be produced on the surface of Cu under the visible light irradiation, which may play a vital role in participating the surface chemical reaction.

In the photo-enhanced catalytic activity measurement (Figure 2.10a), the photo-enhancement showed the similar tendency with their electric field intensity under light irradiation in the 1-Cu, 2-Cu, and 3-Cu sample, while in the 4-Cu sample, the photo-enhanced thermocatalytic activity is lower than 3-Cu, even the intensity of electric field enhancement over 4-Cu is higher. That could be attributed to the lower surface area and less coordinatively unsaturated surface atoms were exposed over 4-Cu, resulting in the lower overall reaction rate. Above investigation results indicated that both the plasmonic effect and surface catalytic property were determined by the size of plasmonic Cu nanoparticles. Increasing the size of plasmonic Cu nanoparticles could rise the surface electric field enhancement but decrease the surface catalytic property. 3-Cu samples with an average diameter of 34.8 nm demonstrated the best performance towards photo-enhanced thermocatalytic MSC, which could be attributed to the optimized particle size with modulated LSPR effect and surface catalytic property.

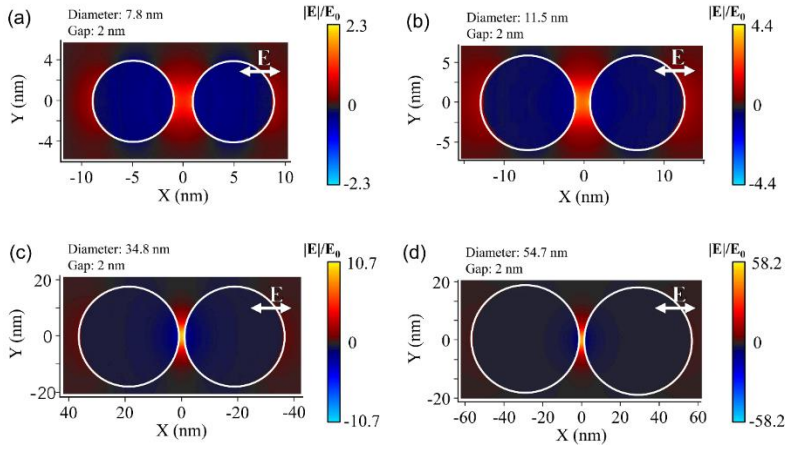

Figure 2.15 Electrical field simulation. Electrical field enhancement of (a) 1-Cu, (b) 2-Cu, (c) 3-Cu, and (d) 4-Cu under the irradiation of 570 nm.

2.3.4 Solar-driven MSC over optimized Cu sample

Since the 3-Cu sample could achieve superior photo-enhanced thermocatalytic activity, I further investigated the performance of the solar-driven MSC over optimized Cu (3-Cu sample) using the home-made solar-driven reactor, and the solar-irradiance was simulated by AM 1.5 light. As presented in Figure 2.16, the H_2 production rate over 3-Cu catalysts increased linearly with the increasing light intensity. Under the irradiation intensity of 570 mW cm^{-2}, 3-Cu exhibited a H_2 production rate of 654 μmol g^{-1} min^{-1}, and the reaction rate was increased to 4318 μmol g^{-1} min^{-1} with the light intensity increasing to the maximum value (933 mW cm^{-2}). The production rates of H_2 and methyl formate over 3-Cu during solar-driven condition were roughly consistent with the stoichiometry of the methanol self-coupling reaction (producing 2 moles of H_2 and 1 mole of methyl formate from 2 moles of methanol). As revealed in Figure 2.16, 3-Cu catalysts demonstrated a MF production rate of 280 μmol g^{-1} min^{-1} under the minimum irradiation intensity of 570 mW cm^{-2}. The production rate of MF also increased linearly with the rise of light intensity. Under the irradiation intensity of 933 mW cm^{-2}, the production rate of MF can be reached at 2116 μmol g^{-1} min^{-1}.

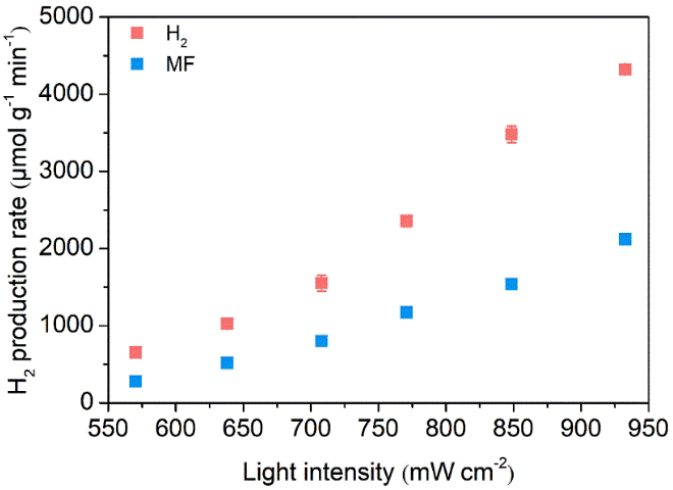

Figure 2.16 Solar-driven methanol self-coupling for the production of H_2 and methyl formate over 3-Cu catalysts under irradiation of different light intensity.

During the solar-driven MSC process over 3-Cu, only a trace amount of undesirable product (such as CO) was detected, confirming the absence of unintended side reactions (Table 2.2). The solar-energy conversion efficiency, which can be defined as the efficiency of solar-energy converted into chemical energy in the form of reaction enthalpy,

was calculated over 3-Cu. The results suggested that at the maximum light intensity of 933 mW cm^{-2}, the conversion efficiency can be reached at approximately 3.6 % over 3-Cu (Figure 2.17). These results indicated that the 3-Cu nanoparticles exhibited good performance for solar-driven catalytic MSC.

Table 2.2 Solar-driven catalytic performance for MSC over 3-Cu catalyst

Reaction condition	H_2 rate (μmol g^{-1} min^{-1})	MF rate (μmol g^{-1} min^{-1})	Selectivity (CO) %
932.7 mW (cm^{-2}) (281.5 °C)	4318.7	2116.3	3.4
848.7 mW (cm^{-2}) (263.6 °C)	3478.3	1535.4	2.0
770.9 mW (cm^{-2}) (242.5 °C)	2356.8	1169.2	1.3
708.1 mW (cm^{-2}) (230.8 °C)	1551.7	800.0	0.8
638.2 mW (cm^{-2}) (215.8 °C)	1022.8	516.0	0.6
570.4 mW (cm^{-2}) (198.0 °C)	654.2	279.3	0.3

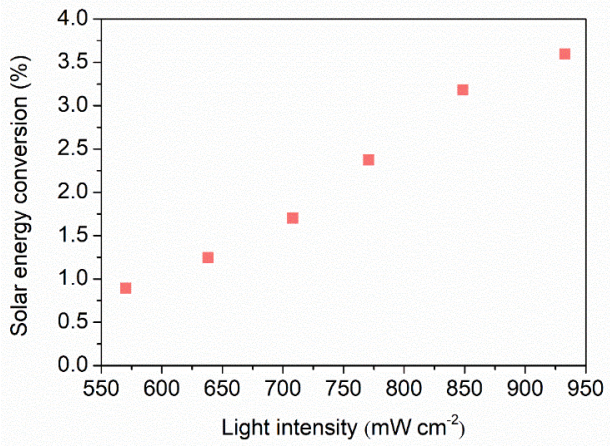

Figure 2.17 Solar-to-energy conversion efficiency of 3-Cu under irradiation of different light intensity.

2.4 Conclusions

In this chapter, I demonstrated that the light absorption property of plasmonic Cu can be modulated by changing the size of nanoparticle, which ultimately controlled the production of energetic hot carriers for promoting the methanol self-coupling reaction under light irradiation. The photo-enhancement was varied by changing the average particle size, and the Cu nanoparticle with mean diameter of 34.8 nm was considered as the optimal samples towards photo-enhanced MSC. Mechanistic investigations revealed that the photo-induced hot carriers over Cu nanoparticle played dominant role in the catalytic enhancement under light irradiation, leading to an approximately 40% decrement of the apparent activation energy compared to that under purely thermocatalytic condition. The optimal plasmonic effect and thermocatalytic property rendered the 3-Cu a highly efficient solar-driven MSC activity. Under the irradiation of concentrated solar light (932.7 mW cm^{-2}), a H_2 production rate of 4318 μmol g^{-1} min^{-1} with the solar-energy conversion efficiency up to 3.6% was achieved. Our findings indicated that in order to construct plasmonic photothermal catalysts with high catalytic performance, both the thermocatalytic performance and the LSPR effect needs to be systematically considered.

References

1. M. Z. Jacobson, W. Colella and D. Golden, *Science*, 2005, **308**, 1901-1905.

2. G. Sievi, D. Geburtig, T. Skeledzic, A. Bösmann, P. Preuster, O. Brummel, F. Waidhas, M. A. Montero, P. Khanipour, I. Katsounaros, J. Libuda, K. J. J. Mayrhofer and P. Wasserscheid, *Energy Environ. Sci.*, 2019, **12**, 2305-2314.

3. I. E. L. Stephens, J. Rossmeisl and I. Chorkendorff, *Science*, 2016, **354**, 1378.

4. R. L. Cohen and J. Wernick, *Science*, 1981, **214**, 1081-1087.

5. A. Anastasopoulou, H. Furukawa, B. R. Barnett, H. Z. H. Jiang, J. R. Long and H. M. Breunig, *Energy Environ. Sci.*, 2021, **14**, 1083-1094.

6. D. Teichmann, W. Arlt, P. Wasserscheid and R. Freymann., *Energy Environ. Sci.*, 2011, **4**, 2767-2773.

7. Y.-Q. Zou, N. von Wolff, A. Anaby, Y. Xie and D. Milstein, *Nat. Catal.*, 2019, **2**, 415-422.

8. P. Hu, E. Fogler, Y. Diskin-Posner, M. A. Iron and D. Milstein, *Nat. Commun.*, 2015, **6**, 6859.

9. M. Nielsen, E. Alberico, W. Baumann, H. J. Drexler, H. Junge, S. Gladiali and M. Beller, *Nature*, 2013, **495**, 85-89.

10. N. Garg, A. Sarkar and B. Sundararaju, *Coord. Chem. Rev.*, 2021, **433**, 213728.

11. P. Preuster, C. Papp and P. Wasserscheid, *Acc. Chem. Res.*, 2017, **50**, 74-85.

12. I. A. Fisher and A. T. Bell, *J. Catal.*, 1999, **184**, 357-376.

13. S. Cao, M. Yang, A. O. Elnabawy, A. Trimpalis, S. Li, C. Wang, F. Göltl, Z. Chen, J. Liu, J. Shan, M. Li, T. Haas, K. W. Chapman, S. Lee, L. F. Allard, M. Mavrikakis and M. Flytzani-Stephanopoulos, *Nat. Chem.*, 2019, **11**, 1098-1105.

14. J. Zhao, R. Shi, Z. Li, C. Zhou and T. Zhang, *Nano Select*, 2020, **1**, 12-29.

15. A. Guerrero-Ruiz, I. Rodriguez-Ramos and J. L. G. Fierro, *Appl. Catal.*, 1991, **72**, 119-137.

16. H. Yang, Y. Chen, X. Cui, G. Wang, Y. Cen, T. Deng, W. Yan, J. Gao, S. Zhu, U. Olsbye, J. Wang and W. Fan, *Angew. Chem. Int. Ed.*, 2018, **57**, 1836-1840.

17. D.-J. Yuan, A. M. Hengne, Y. Saih and K.-W. Huang, *ACS Omega*, 2019, **4**, 1854-1860.

18. Y. Zhao, W. Gao, S. Li, G. R. Williams, A. H. Mahadi and D. Ma, *Joule*, 2019, **3**, 920-937.

19. Z.-j. Wang, H. Song, H. Liu and J. Ye, *Angew. Chem. Int. Ed.*, 2020, **59**, 8016-8035.

20. U. Aslam, V. G. Rao, S. Chavez and S. Linic, *Nat. Catal.*, 2018, **1**, 656-665.

21. S. Rej, L. Mascaretti, E. Y. Santiago, O. Tomanec, Š. Kment, Z. Wang, R. Zbořil, P. Fornasiero, A. O. Govorov and A. Naldoni, *ACS Catal.*, 2020, **10**, 5261-5271.

22. L. Zhou, D. F. Swearer, C. Zhang, H. Robatjazi, H. Zhao, L. Henderson, L. Dong, P. Christopher, E. A. Carter, P. Nordlander and N. J. Halas, *Science*, 2018, **362**, 69-72.

23. S. Linic, U. Aslam, C. Boerigter and M. Morabito, *Nat. Mater.*, 2015, **14**, 567-576.

24. U. Aslam, S. Chavez and S. Linic, *Nat. Nanotechnol.*, 2017, **12**, 1000-1005.

25. M. Ghoussoub, M. Xia, P. N. Duchesne, D. Segal and G. Ozin, *Energy Environ. Sci.*, 2019, **12**, 1122-1142.

26. P. Christopher, H. Xin and S. Linic, *Nat. Chem.*, 2011, **3**, 467-472.

27. S. Linic, P. Christopher, H. Xin and A. Marimuthu, *Acc. Chem. Res.*, 2013, **46**, 1890-1899.

28. P. Christopher, H. Xin, A. Marimuthu and S. Linic, *Nat. Mater.*, 2012, **11**, 1044-1050.

29. H. Robatjazi, H. Zhao, D. F. Swearer, N. J. Hogan, L. Zhou, A. Alabastri, M. J. McClain, P. Nordlander and N. J. Halas, *Nat. Commun.*, 2017, **8**, 27.

30. M. A. El-Sayed, *Acc. Chem. Res.*, 2001, **34**, 257-264.

31. C. Burda, X. Chen, R. Narayanan and M. A. El-Sayed, *Chem. Rev.*, 2005, **105**, 1025-1102.

32. B. D. Clark, C. R. Jacobson, M. Lou, D. Renard, G. Wu, L. Bursi, A. S. Ali, D. F. Swearer, A.-L. Tsai, P. Nordlander and N. J. Halas, *ACS Nano*, 2019, **13**, 9682-9691.

33. L. Yuan, M. Lou, B. D. Clark, M. Lou, L. Zhou, S. Tian, C. R. Jacobson, P. Nordlander and N. J. Halas, *ACS Nano*, 2020, **14**, 12054-12063.

34. S. Linic, S. Chavez and R. Elias, *Nat. Mater.*, 2021, DOI: 10.1038/s41563-020-00858-4.

35. C. Wang and D. Astruc, *Chem. Soc. Rev.*, 2014, **43**, 7188-7216.

36. K. Qian, B. C. Sweeny, A. C. Johnston-Peck, W. Niu, J. O. Graham, J. S. DuChene, J. Qiu, Y.-C. Wang, M. H. Engelhard, D. Su, E. A. Stach and W. D. Wei, *J. Am. Chem. Soc.*, 2014, **136**, 9842-9845.

37. H. Liu, H. Song, X. Meng, L. Yang and J. Ye, *Catal. Today*, 2019, **335**, 187-192.

38. R. Long, Y. Li, L. Song and Y. Xiong, *Small*, 2015, **11**, 3873-3889.

39. B. Ni and X. Wang, *Adv. Sci.*, 2015, **2**, 1500085.

40. L. Liu and A. Corma, *Chem. Rev.*, 2018, **118**, 4981-5079.

41. S. Cao, F. Tao, Y. Tang, Y. Li and J. Yu, *Chem. Soc. Rev.*, 2016, **45**, 4747-4765.

42. E. D. Palik, *Handbook of optical constants of solids*, Academic press, 1998.

43. W. S. M. Werner, K. Glantschnig and C. Ambrosch-Draxl, *J. Phys. Chem. Ref. Data*, 2009, **38**, 1013-1092.

44. M. Romand, M. Roubin and J. P. Deloume, *J. Electron. Spectrosc. Relat. Phenom.*, 1978, **13**, 229-242.

45. K. S. Kim, S. W. Gaarenstroom and N. Winograd, *Chem. Phys. Lett.*, 1976, **41**, 503-506.

46. H. Song, X. Meng, Z.-j. Wang, Z. Wang, H. Chen, Y. Weng, F. Ichihara, M. Oshikiri, T. Kako and J. Ye, *ACS Catal.*, 2018, **8**, 7556-7565.

47. S. Luo, X. Ren, H. Lin, H. Song and J. Ye, *Chem. Sci.*, 2021, DOI: 10.1039/D1SC00064K, 10.1039/D1031SC00064K.

Chapter 3 Solar-driven production of hydrogen and acetaldehyde from ethanol on Ni-Cu bimetallic catalysts

3.1 Introduction

Hydrogen (H_2) is an important chemical and fuel which can be utilized for many applications, such as hydrogenation reaction and fuel cell.[1-3] To date, large-scale hydrogen production in the industry is primarily through steam methane reforming; however, this process requires high operating temperatures (700-1100 °C), thus consuming a massive amount of energy.[4] Since solar light is by far the greatest available source of renewable energy, the utilization of solar energy to drive the chemical reactions, so-called photocatalytic process, is attractive for its sustainability.[5, 6] Photocatalytic H_2 production from ethanol dehydrogenation ($CH_3CH_2OH \rightarrow CH_3CHO + H_2$, $\Delta H = 68$ kJ mol^{-1}) is a promising alternative approach because only solar light is employed as the energy input and ethanol can be produced from renewable biomass.[7] In addition, the other product, acetaldehyde is one of the important building blocks for the synthesis of various industrial chemicals.[8, 9] This reaction has been intensively studied by using various semiconductors and/or metals in these recent years,[7, 10-12] however, the reported efficiencies are still quite low (remains only several mmol $g_{catalyst}^{-1}$ h^{-1} level with low solar-to-fuel conversion efficiency), rendering no any potential industrial applications.[13, 14] Up until now, in order to obtain a satisfactory production rate in the photocatalytic ethanol dehydrogenation system, thermal energy is still required as the main energy input to drive the reaction.[15] In this case, a significant breakthrough is necessary to manifest the efficient solar-driven ethanol dehydrogenation system (without any thermal energy input) for prospective and cost-effective industrial processes.

Recently, light-harvesting plasmonic metal nanostructures have attracted much research interests.[16-18] Compared with the traditional photocatalytic process, the full solar spectrum, including the ultra-violet (UV), visible, and even near-infrared (NIR) light can be utilized by plasmonic metal catalysts to drive catalytic reactions.[19] With the assistance of light, plasmonic photocatalysts can drive many reactions with enhanced activities under far milder conditions compared to conventional thermocatalysis.[20, 21] The strong interaction between photon energy and plasmonic metal nanostructures through the excitation of localized surface plasmon resonance (LSPR) generates energetic hot carriers,

which can drive reactions by locally heating nanoparticles and/or transferring the energy into reactants for synergistically enhancing the catalytic activity.[22] Plasmonic metal nanoparticles such as Au, Ag, Cu have been employed as catalysts in various chemical reactions such as carbon dioxide reduction and methane reforming reactions.[23-27] Among all the plasmonic metals, Cu is a promising candidate for practical application due to its low cost and unique properties.[28-30] Recently, Halas and her colleagues demonstrated that hot carriers and photo-thermal effect could be produced simultaneously by the illumination of plasmonic Cu-Ru nanoparticles for reducing the reaction activation barrier.[16] In addition, Cu-based nanomaterials are also good candidate catalysts for thermal catalytic ethanol dehydrogenation.[31-33] It was reported that Cu-Ni single atom alloy catalysts could exhibit good activity and stability towards thermal catalytic ethanol dehydrogenation reaction, where Ni single atom would improve the activity and stability of Cu nanoparticles.[34] Nevertheless, this process still required a relatively high operating temperature (~ 300 °C).

In this study, I demonstrate an efficient solar-driven ethanol dehydrogenation process for the production of H_2 and acetaldehyde over plasmonic Ni-Cu bimetallic catalysts. Under the illumination of simulated 5.7 Suns with no external energy input, a superior H_2 production rate of 176.6 mmol $g_{catalyst}^{-1}$ h^{-1} with 3.81% of solar-to-fuel conversion efficiency is obtained. Mechanistic investigations indicate that photothermal heating and hot carrier generation over Ni-Cu catalysts take responsibility for the high activity. The apparent activation energy for ethanol dehydrogenation reaction is reduced by ~55% over Ni-Cu bimetallic catalysts under visible light irradiation compared to the pure Cu under dark condition. *In-situ* DRIFTS results reveal that the adsorbed intermediates could be activated by the photo-induced hot carriers. First-principles molecular dynamics simulation results suggest that the hot electrons produced by Cu nanoparticles easily migrate to Ni atoms and then transfer to the adsorbates, hence suppressing the non-effective carrier recombination and leading to the promotion of hydrogen production.

3.2 Experimental section

3.2.1 Material preparation

Cu nanoparticles were synthesized by using the wet chemistry method.[32] Accordingly, 0.1 M (10 mL) ascorbic acid (L(+)-Ascorbic acid, Wako, 99% purity, CAS: 50-81-7) solution was added into a mixed aqueous solution (100 mL) of Cu $(NO_3)_2 \cdot 3H_2O$ (Copper

nitrate trihydrate, Wako, 99% purity, CAS: 10031-43-3) and PVP (Polyvinylpyrrolidone, Sigma-Aldrich, CAS: 9003-39-8) (200:1 molar ratio of Cu to PVP). 500 mg of SiO_2 (Silicon dioxide, Wako, 99.9% purity, CAS: 7631-86-9) was then added into the solution, under continuous stirring to form a homogeneous dispersion. Afterward, 0.1 M (10 mL) of $NaBH_4$ (Sodium tetrahydroborate, Wako, 95% purity, CAS: 16940-66-2) was drop-wisely added into the solution. The solution was stirred continuously at room temperature in the Ar atmosphere to prevent the oxidation of Cu. After stirred for 1 h, the solid was collected and washed by ethanol and water three times, followed by drying in a vacuum oven in 70 °C overnight and calcination in the air at 350 °C for 4 h. The sample was reduced in hydrogen (10% in Ar) at 350 °C for 3 h to prepare SiO_2 supported metallic Cu nanoparticle (named as Cu here and after). Ni atoms were deposited on Cu by using electroless galvanic deposition method,[34] based on the following reaction:

$$2Cu + 2OH^- + Ni^{2+} = Cu_2O + Ni + H_2O, \Delta E^0 = +0.103\ V$$

The Cu atom can be substituted by Ni in alkaline solution spontaneously with the oxidation of the Cu. The fabrication process (Figure 3.1) was shown as follows: pH value of Ni $(NO_3)_2 \cdot 3H_2O$ (Nickel nitrate hexahydrate, Wako, 99% purity, CAS: 13478-00-7) aqueous solution was adjusted to 10.83 by drop-wise adding 0.01 M NaOH (Sodium Hydroxide, Wako, 97% purity, CAS: 1310-73-2) under Ar protection and continuous stirring. Subsequently, a certain amount of Cu was added into the solution, and keep stirred under Ar protection for 1 h. The precipitates were collected by using a centrifuge, washed with deionized water three times and then dried at 70 °C in vacuum overnight. The catalysts were then reduced in hydrogen (10% in Ar) at 400 °C for 1 h. The typical atomic ratio of Ni in Cu ranges from 0.04 to 0.18, as determined by the inductivity coupled plasma optical emission spectrometer (ICP-OES). For comparison, pure Ni catalysts were synthesis by the same method as the fabrication process of Cu, and the Ni $(NO_3)_2 \cdot 3H_2O$ was utilized as the nickel source.

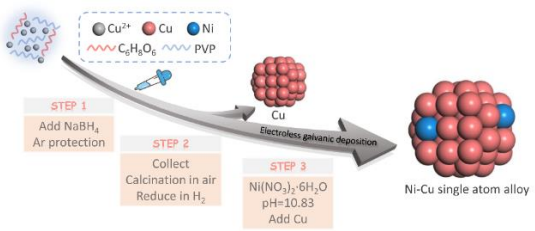

Figure 3.1 Schematic illustration of the preparation process of Ni-Cu bimetallic catalysts.

3.2.2 Material characterization

The crystalline structures of the catalysts were characterized using an X-ray powder diffractometer with Cu Kα radiation (PANalytical). The surface electronic states of catalysts were investigated by X-ray photoelectron spectroscopy (XPS, Escalab 250 Xi, Thermo Scientific). UV-Vis absorption spectra of catalysts were collected by a spectrophotometer (UV-2600, Shimadzu). Transmission electron microscopy (TEM) and high-resolution TEM (HRTEM) measurements were carried out on the FEI TECNAI G2 F30 instrument. Scanning transmission electron microscope energy dispersive X-ray spectrometry (STEM-EDS) mapping analysis was conducted on a FEI Titan Cubed instrument. Light intensity and wavelength distribution of the illuminant were analyzed by the USR-40 spectrophotometer. Diffuse reflectance infrared Fourier transform spectroscopy (DRIFTS) measurements were performed on a FT-IR-6300 system (JASCO Corp.) equipped with an *in-situ* DR cell and a liquid nitrogen-cooled mercury-cadmium-telluride detector. For CO-DRIFTS, 10 mg samples were firstly reduced in the reaction cell in a hydrogen atmosphere at 350 °C for 1 h. After the reduction, the samples were purged with Ar gas. Background spectra were recorded in the Ar atmosphere after the catalysts cooling down to room temperature. CO gas (2% in Ar) was introduced into the cell for 20 min at a flow rate of 10 mL min^{-1}, then the gas was switched to Ar flowing at 20 mL min^{-1}. After Ar gas purged for 5 min and 15 min, spectra were recorded.

3.2.3 Photocatalytic activity measurements

Two different types of reactors (solar-driven catalysis reactor and photo-assisted thermal catalysis reactor) were utilized to manifest the solar-driven catalytic activity and reaction mechanism, respectively. Solar-driven ethanol dehydrogenation reaction was conducted in a home-made flow-type reactor (diameter 10 mm) with quartz cover to allow the irradiation of light to catalysts (Figure 3.2). In this measurement, the AM 1.5 light was employed as the illuminant, and no external thermal energy was applied. A maximum light intensity of 574 mW cm^{-2} was achieved by the optical lens (Figure 3.3). A thermocouple was utilized to test the surface temperature of catalysts. Prior to the activity measurement, the catalysts (10 mg) were reduced at 350 °C for 1 h under a flow of hydrogen (10% in Ar), then dispersed in the reaction cell uniformly after cooling down to the room temperature. Through a bubbler system, the reaction gas (5.6% ethanol

balanced in Ar) was introduced into the reactor. The space velocity was controlled to be 50 mL min^{-1} unless otherwise specified. The products were quantified by gas chromatography (GC) equipped with thermal conductivity and flame ionization detector.

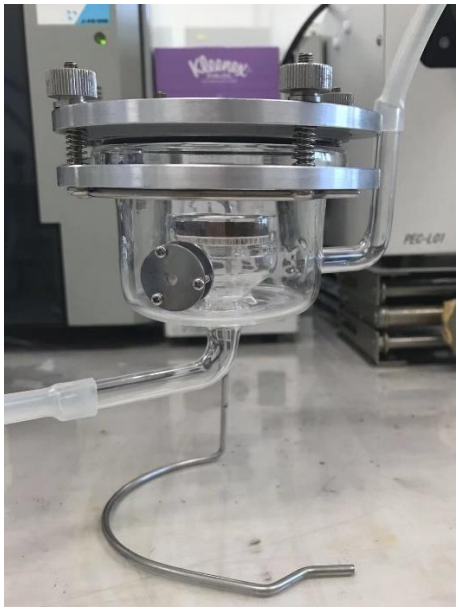

Figure 3.2 Photograph of home-made reactor for solar-driven ethanol dehydrogenation.

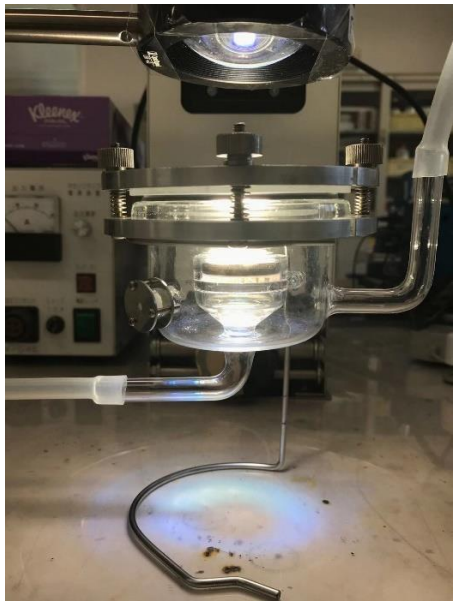

Figure 3.3 Photograph of home-made reactor irradiated by focused sun light.

The solar-to-fuel (STF) efficiency in different light intensity was calculated by the following formula.[35]:

$$STF = [r(H_2) \times \Delta_f G^0_{H_2} + r(C_2H_4O) \times \Delta_f G^0_{C_2H_4O} - r(C_2H_6O) \times \Delta_f G^0_{C_2H_6O}]/P_{\text{irradiation}} \times 100\%$$

The standard molar Gibbs energies of formation (Δ_fG^0) for H_2, C_2H_4O, and C_2H_6O ($\Delta_fG^0_{H2}$, $\Delta_fG^0_{C2H4O}$, and $\Delta_fG^0_{C2H6O}$) are 0, -133.0 and -167.9 kJ mol^{-1},[35, 36] $P_{irradiation}$: the power of light irradiation. In our reaction, only trace amount of CO and CH_4 were generated, indicating the selectivity of this reaction was nearly 100%. Therefore, the r(H_2), r(C_2H_4O) and r(C_2H_6O) were considered to be the same in the STF calculation.

In order to elucidate the reaction mechanism, photo-assisted thermal catalytic ethanol dehydrogenation reaction was conducted under atmospheric pressure in a homemade flow-bed reactor (diameter 8.5 mm), as shown in Figure 3.4. A quartz window was equipped on the reactor to allow the irradiation of visible light to the catalysts. LA-251 Xe lamp with HA30 and L42 filters (to remove the infrared and ultra-violate light) was employed to provide the photon energy (Figure 3.5). The thermocouple and temperature controller (TC-1000, JASCO) were utilized to keep the catalysts at the desired temperature (Figure 3.6). Heat induced by light irradiation was be mitigated by the temperature controller (Figure 3.7). Typically, 5 mg of catalysts were dispersed in the reaction cell uniformly. Prior to the activity measurement, the catalysts were *in-situ* reduced in the reactor at 350 °C for 1 h under a flow of hydrogen (10% in Ar), then cooling down to the room temperature. Subsequently, the reactor was flushed with pure Ar gas for 30 min to remove the hydrogen in the reactor. The reaction gas was introduced into the reactor at a flow rate of 50 mL min^{-1} through the bubbler system. The product measurement method was as same as the solar-driven ethanol dehydrogenation reaction.

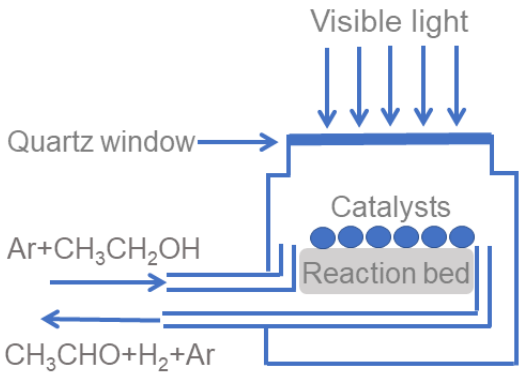

Figure 3.4 Schematic diagram of home-made photo-assisted thermal reactor.

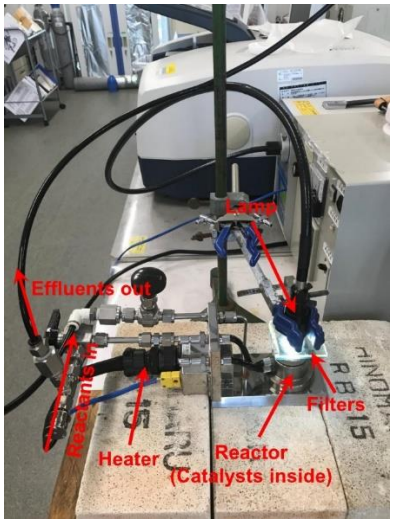

Figure 3.5 Photograph of home-made photo-assisted thermal reactor.

Figure 3.6 Detected temperature of catalysts without light irradiation in the photo-assisted thermal catalytic process.

Figure 3.7 Detected temperature of catalysts with light irradiation in the photo-assisted thermal catalytic process.

3.2.4 *In-situ* DRIFTS analysis

FT-IR-6300 system (JASCO Corp.) equipped with an *in-situ* DR cell and a liquid nitrogen-cooled mercury-cadmium-telluride detector was utilized to elucidate the reaction role of photo-induced hot carriers at 200 °C (Figure 3.8). In DRIFTS measurement, 10 mg of $Ni_{0.04}Cu$ were dispersed uniformly in the DR cell, and in-situ reduced under a flow of hydrogen (10% in Ar) at 350 °C for 1 h. After cooling down to the room temperature, pure Ar gas was introduced to remove the hydrogen, followed by the introduction of Ar (20 mL min^{-1}) at 200 °C to get the background spectrum of the system. The DRIFT spectra during the reaction were recorded after the reaction gas was introduced in the reaction cell at 200 °C with the irradiation of visible light for 15 min.

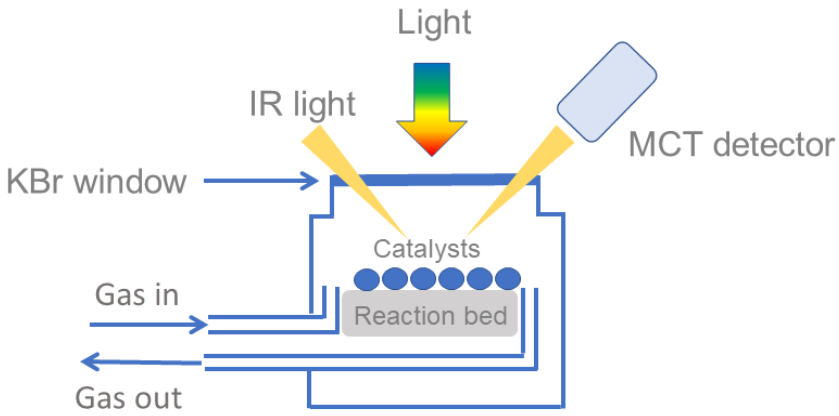

Figure 3.8 Schematic diagram of reactor cell for the *in-situ* DRIFTS analysis.

3.2.5 Computational details

First-principles molecular dynamics simulation[37] and the electronic structure calculations based on the density functional theory within local density approximation (DFT-LDA) were carried out to demonstrate the transfer process of electrons excited from the Cu-based nanoparticles to adsorbate materials. To mimic the Ni surficially doped Cu nanoparticles loaded on a SiO_2 supporter material in presence of gas-phase ethanol (CH_3CH_2OH) molecules, I employed the simulation model including a slab of metal Cu, which was doped with Ni atoms only at the slab surface (184 Cu and 8 Ni), at the bottom of the supercell and the reactant molecules of ethanol ($4CH_3CH_2OH$) in the space above the slab mimicking a gas phase. The detailed model specifications were described blow.

Employing the model, the first-principles quantum molecular dynamics simulation (CPMD) was achieved, and have obtained the equilibrium structure of the system at 200 °C (473 K). Then the electronic structure was computed by solving the Kohn-Sham equation within LDA.

Computational model: Cu metal crystal with face-centered cubic lattice, whose lattice length a is 3.615 Å (ICSD code 627114), was quarried in the size of 4a (14.460 Å) × 4a × 3a (10.845 Å) and was placed at the bottom of the simulation cell whose size was 4a × 4a × 20 Å. The eight surficial Cu atoms at the (001) surface were randomly exchanged for Ni. Then the four ethanol molecules were put in the open space (~ 11 Å in thickness) of the cell with moderate distances kept between molecules each other and between the slab surface and the molecules to avoid undesirable bias. The number of atoms of Cu, Ni, C, O, and H included in the cell box were 184, 8, 8, 4, and 24, respectively.

3.3 Results and discussion

3.3.1 Characterization of catalysts

The X-ray powder diffractometer (XRD) pattern of pure Cu and Ni-Cu bimetallic catalysts were presented in Figure 3.9. The XRD pattern of Cu catalysts was dominated by the diffraction peaks of metallic Cu, revealing that the metallic Cu were synthesized successfully. No diffraction peak could be observed for Ni in Ni-Cu bimetallic catalysts, indicating the small particle size and low contents of Ni. As determined by the inductivity coupled plasma optical emission spectrometer (ICP-OES), the typical atomic ratio of Ni in Cu ranges from 0.04 to 0.18 (Table 3.1). Transmission electron microscopy (TEM) images of $Ni_{0.04}Cu$ show that the Cu nanoparticles were dispersed on the surface of SiO_2 supporter, and the average particle size of Cu was approximately 30 nm (Figure 3.10). A clear lattice fringe was measured to be 0.21 nm, which was in good agreement with the interplanar distance of the (111) plane of metallic Cu (Figure 3.11). Scanning transmission electron microscope energy dispersive X-ray spectrometry (STEM-EDS) mapping of $Ni_{0.04}Cu$ (Figure 3.12) showed that no Ni signal could be detected in the STEM-EDS mapping analysis, which could be attributed to the low contents of Ni. However, the map sum spectrum (Figure 3.12e) indicated the presence of Ni in $Ni_{0.04}Cu$, since the weak peaks of Ni were observed.

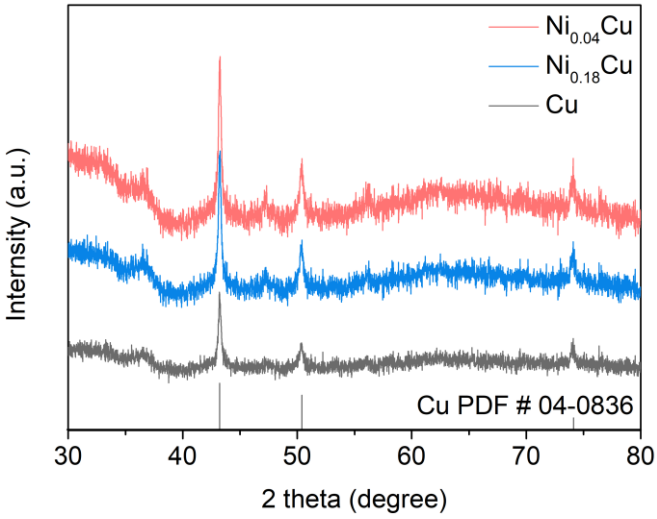

Figure 3.9 XRD patterns of pristine Cu and Ni-Cu bimetallic catalysts.

Table 3.1 Elemental analysis of the catalysts

Samples	Ni (wt. %)[a]	Cu (wt. %)[a]
$Ni_{0.04}Cu$	0.46	10.60
$Ni_{0.18}Cu$	1.78	10.53

a, analyzed by ICP-OES method.

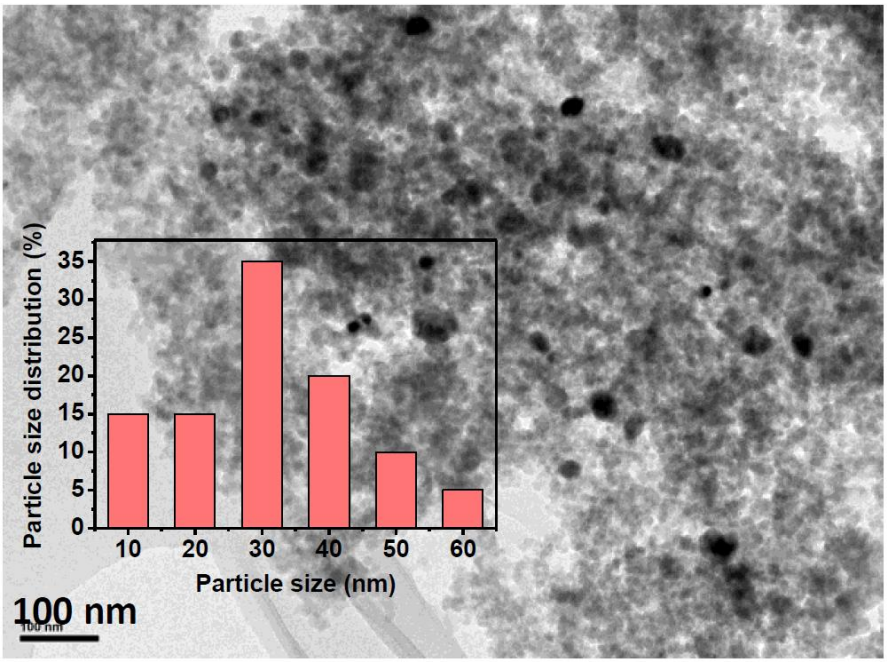

Figure 3.10 TEM image of $Ni_{0.04}Cu$ catalysts

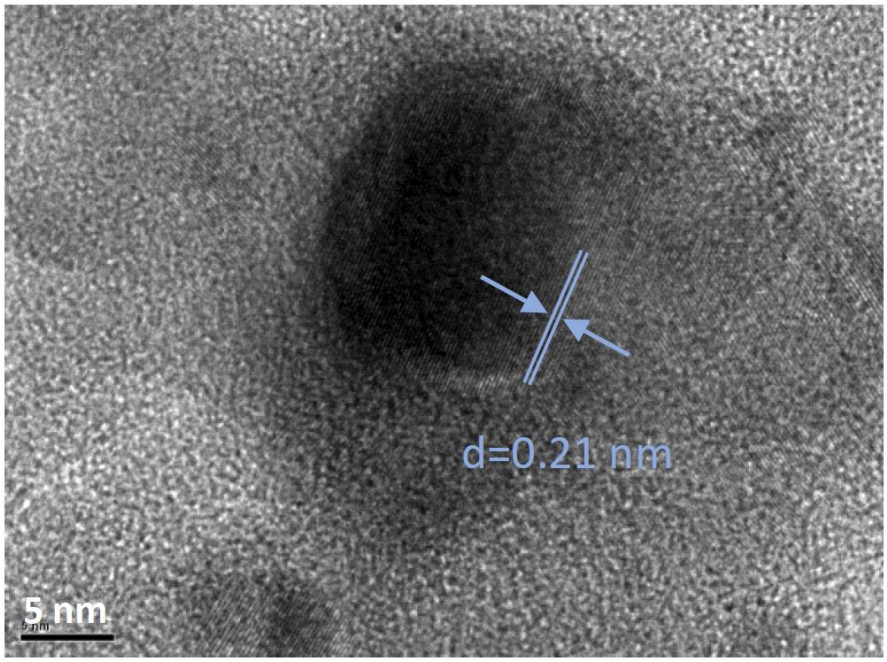

Figure 3.11 HRTEM images of $Ni_{0.04}Cu$ catalysts

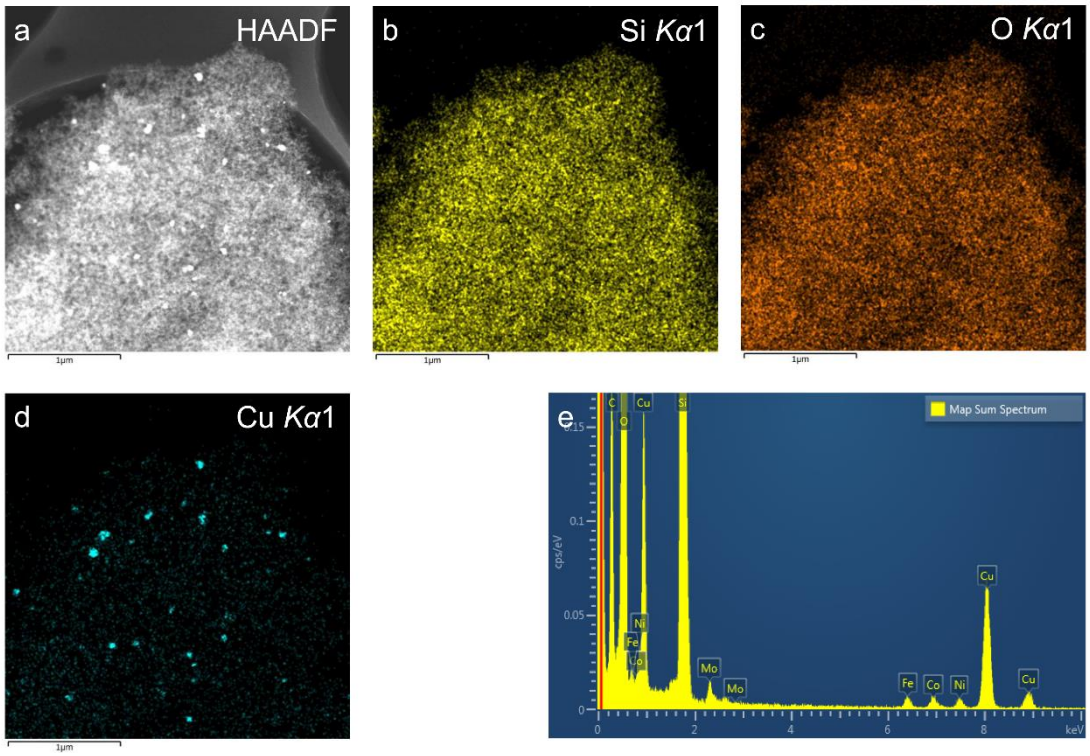

Figure 3.12 STEM-EDS mapping images of $Ni_{0.04}Cu$. (a) High-angle annular dark field (HAADF) image, (b) EDS mapping of Si, (c) EDS mapping of O, (d) EDS mapping of Cu, (e) Map sum spectrum of $Ni_{0.04}Cu$ catalysts

The X-ray photoelectron spectroscopy (XPS) spectra of Cu and Ni were presented in Figure 3.13 and 3.14. In the Cu 2p spectrum, two peaks at 934.8 eV and 933.2 eV were observed, which could be attributed to the Cu^{2+} and metallic Cu, respectively.[3] The existence of Cu^{2+} could be ascribed to the oxidization of catalysts exposed in the air (Figure 3.13). Ni 2p XPS spectra indicated that Ni^{2+} is the dominant species, which could be attributed to the highly dispersed metallic Ni on the surface of Cu can be easily oxidized into NiO in the air (Figure 3.14).[32] The optical properties of pure Cu and $Ni_{0.04}Cu$ catalysts were measured using UV-Vis diffuse reflectance spectra (UV-Vis DRS). As shown in Figure 3.15, the wide absorption peak at a wavelength of 580 nm was observed for the pure Cu catalysts, which could be assigned to the LSPR peak of Cu.[38] After the deposition of Ni on the surface of Cu, the position of absorption peak remains unchanged (Figure 3.15).

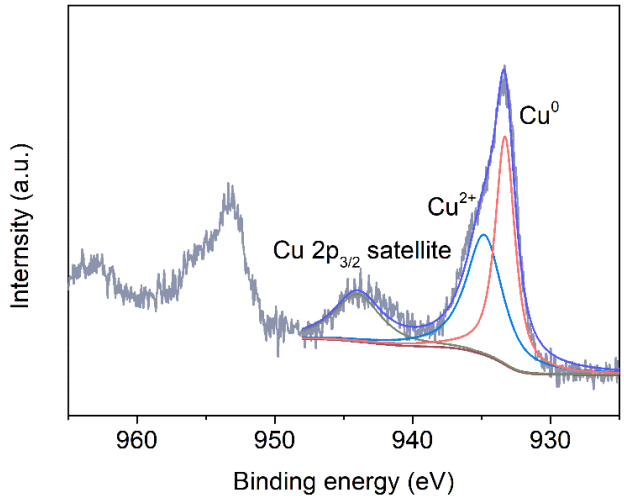

Figure 3.13 XPS Cu spectrum of $Ni_{0.04}Cu$ catalysts.

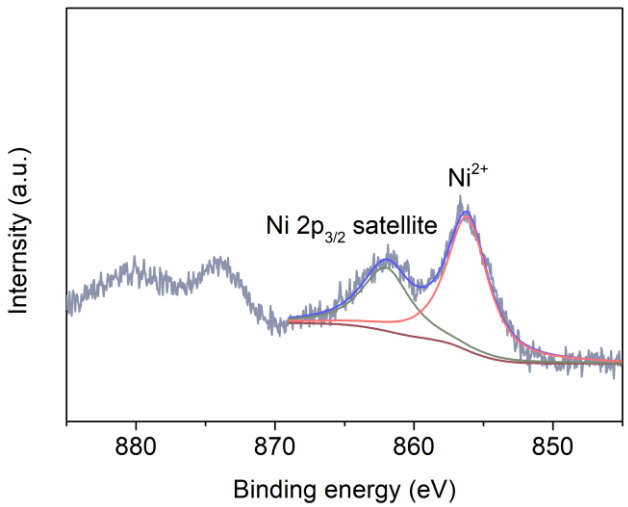

Figure 3.14 XPS Ni spectrum of $Ni_{0.04}Cu$ catalysts.

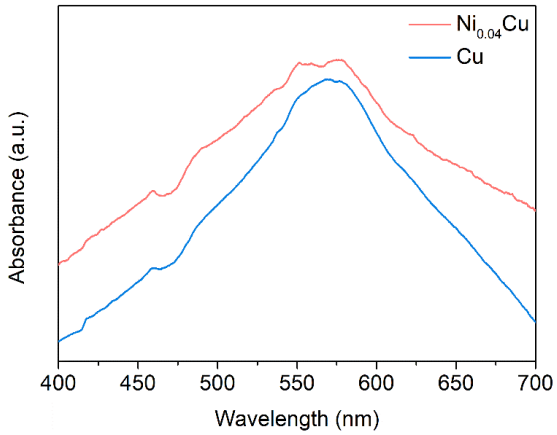

Figure 3.15 UV-Vis DRS patterns of pristine Cu and Ni-Cu bimetallic catalysts.

In order to further elucidate the dispersion of Ni on Cu nanoparticles, CO was employed as a probe molecule in the DRIFTS measurement. In general, single atoms from nanoparticles can be directly identified by using CO in the DRIFTS measurement.[39-43] It is an effective characterization method and provides solid evidence for the formation of single atoms. CO-DRIFT spectra of pure Cu in the CO related region (Figure 3.16a) showed one peak at 2128 cm^{-1}, which could be assigned to CO binding to Cu atom.[44] On the other hand, in the $Ni_{0.18}Cu$ CO-DRIFT spectra (Figure 3.16b), the main peak was observed at 2110 cm^{-1}, which may be related to the adsorption of CO on Ni nanoparticle. The existence of a linear CO adsorption peak at ~2055 cm^{-1} indicated the presence of Ni nanoparticles in $Ni_{0.18}Cu$.[45] Compared with pure Cu and $Ni_{0.18}Cu$, $Ni_{0.04}Cu$ (Figure 3.16c) displayed the main peak at 2128 cm^{-1} and a shoulder peak at 2110 cm^{-1}, while the linear CO adsorption peak was completely absent. The additional shoulder peak at 2110 cm^{-1} could be attributed to Ni(CO)x sub-carbonyl species with x = 2 or 3.[32, 45] CO-DRIFT spectra of $Ni_{0.04}Cu$ indicated that Ni atoms were atomically dispersed on Cu nanoparticles.

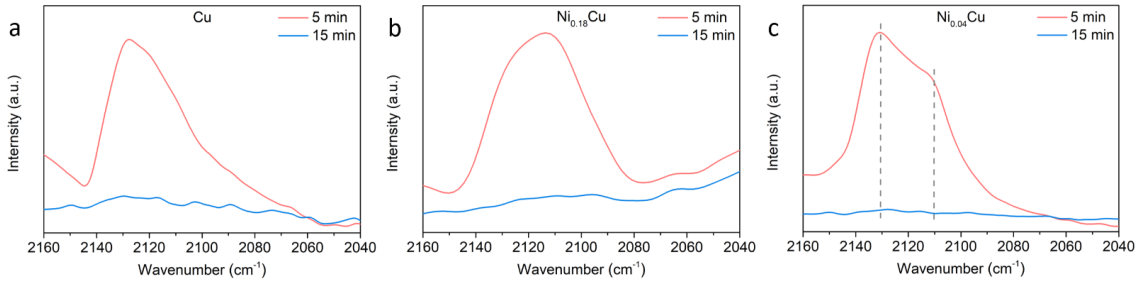

Figure 3.16 CO-DRIFT spectra of (a) pristine Cu catalysts, (b) $Ni_{0.18}Cu$ catalysts, and (c) $Ni_{0.04}Cu$ catalysts.

3.3.2 Solar-driven ethanol dehydrogenation reaction over Ni-Cu bimetallic catalysts

Solar-driven ethanol dehydrogenation reaction over Ni-Cu bimetallic catalysts was performed on a home-made flow-bed reactor under atmospheric pressure. The AM 1.5 light was employed as the illuminant. An optical lens was utilized to focus the light. Maximum light intensity was measured to be 574 mW cm^{-2} (~ 5.7 suns). As shown in Figure 3.17a, with the increasing light intensity, the surface temperature of catalysts increased linearly. A surface temperature of 209 °C was achieved on the $Ni_{0.04}Cu$ at maximum light intensity (Figure 3.17a). Roughly the same temperatures were detected on the surface of $Ni_{0.04}Cu$, $Ni_{0.18}Cu$, and Cu. Figure 3.17b showed that under the irradiation intensity of 289 mW cm^{-2}, $Ni_{0.04}Cu$ exhibited H_2 production rate of 115 μmol $g_{catalyst}^{-1}$ min^{-1}, which was higher than pure Cu (66 μmol $g_{catalyst}^{-1}$ min^{-1}). The reaction rate was increased exponentially with the increasing light intensity. The H_2 production rate of $Ni_{0.04}Cu$ increased to 2943 μmol $g_{catalyst}^{-1}$ min^{-1}, corresponding to 176.6 mmol $g_{catalyst}^{-1}$ h^{-1}, with the light intensity increasing to 574 mW cm^{-2}, while the pure Cu only displayed the reaction rate of 1281 μmol $g_{catalyst}^{-1}$ min^{-1} at a same light intensity. This result illustrated that after adding a little amount of Ni on Cu, $Ni_{0.04}Cu$ showed much higher activity than pure Cu towards ethanol dehydrogenation reaction. Further increasing Ni contents could decrease the catalytic ethanol dehydrogenation activity of Ni-Cu bimetallic catalysts. Compared with $Ni_{0.04}Cu$ (2943 μmol $g_{catalyst}^{-1}$ min^{-1} at 574 mW cm^{-2}), $Ni_{0.18}Cu$ displayed lower activity (2125 μmol $g_{catalyst}^{-1}$ min^{-1}). This result suggested that atomic dispersed Ni significantly promoted the solar-driven catalytic activity of Ni-Cu bimetallic catalysts. Figure 3.17c showed that the solar-to-fuel (STF) efficiency increased with the increasing light intensity. The efficiency of $Ni_{0.04}Cu$ reached about 3.81% when the light intensity was 574 mW cm^{-2}. In addition, the reaction rate in different space velocity (Figure 3.17d) of $Ni_{0.04}Cu$ showed that the reaction rate increased with the increasing space velocity in the low space velocity area (10-50 mL min^{-1}). The H_2 production rate reached maximum value under the space velocity of 50 mL min^{-1}. When the space velocity further increased, the reaction rate remained nearly unchanged.

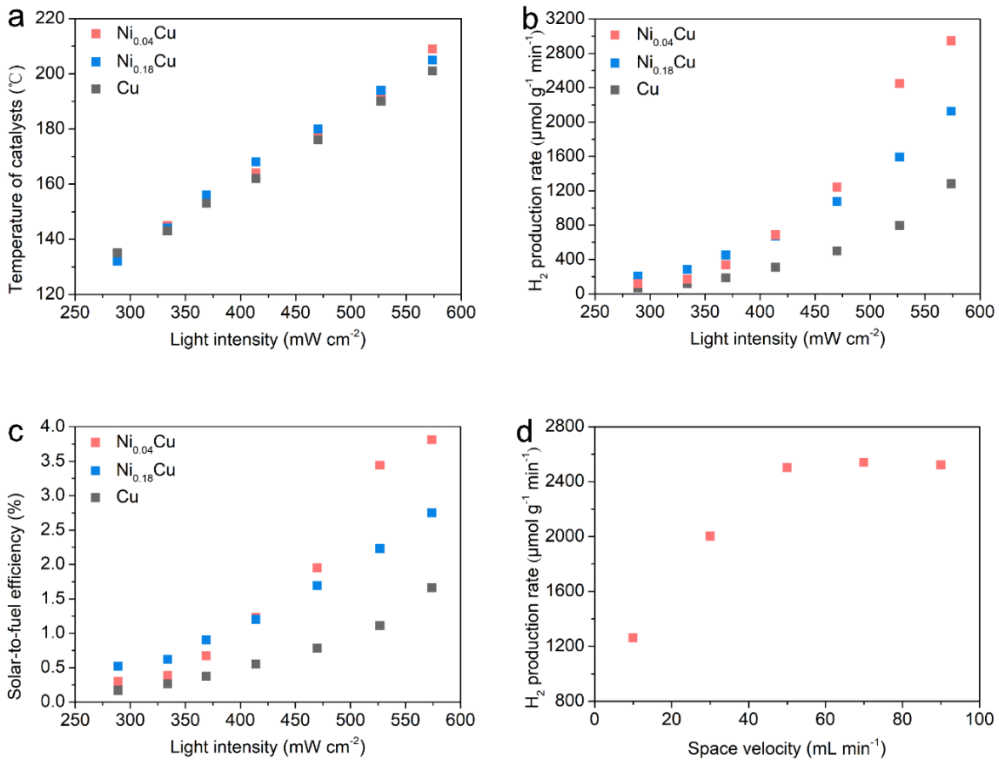

Figure 3.17 Solar-driven ethanol dehydrogenation reaction over Ni-Cu bimetallic catalysts. (a) Dependence of surface temperature of pure Cu and Ni-Cu bimetallic catalysts on different light intensity, (b) Solar-driven ethanol dehydrogenation activity over pure Cu and Ni-Cu bimetallic catalysts, (c) Solar-to-fuel efficiency of pure Cu and Ni-Cu bimetallic catalysts, (d) Dependence of H_2 production rate of $Ni_{0.04}Cu$ on different space velocity under the irradiation intensity of 527 mW cm^{-2}.

3.3.3 Mechanism for hot carriers assisted ethanol dehydrogenation reaction

Photo-assisted thermal catalytic ethanol dehydrogenation reaction was performed on a flow-bed reactor under atmospheric pressure to elucidate the reaction mechanism of hot carriers. To rule out the influence of UV and IR light, only visible light ($420 < \lambda < 800$ nm) with an intensity of ~440 mW cm^{-2} was used in the measurement (Figure 3.18). As shown in Figure 3.19a, under the dark conditions, the H_2 production rate of pure Cu and Ni-Cu bimetallic catalysts increased with increasing reaction temperature. The H_2 production rate of $Ni_{0.04}Cu$ was increased from 264.3 μmol $g_{catalyst}^{-1}$ min^{-1} to 1192.0 μmol $g_{catalyst}^{-1}$ min^{-1} with the increasing temperature from 170 °C to 210 °C, which is higher than the pure Cu at the same reaction temperature. Moreover, the reaction rate could be further promoted after introducing photon energy. As shown from Figure 3.19a, under

the visible light irradiation with the reaction temperature of 170 °C, the H_2 production rate of $Ni_{0.04}Cu$ was measured to be 878.4 μmol $g_{catalyst}^{-1}$ min^{-1}, which is nearly 3.3 times over the reaction rate under dark condition. After the reaction temperature increased to 210 °C with visible light irradiation, the reaction rate of $Ni_{0.04}Cu$ increased to 2140.7 μmol $g_{catalyst}^{-1}$ min^{-1}, which is higher than pure Cu (1073 μmol $g_{catalyst}^{-1}$ min^{-1}) at the same reaction condition. These results indicated that the visible light energy could facilitate the ethanol dehydrogenation activity. Steady-state reaction hydrogen production rate at a temperature of 200 °C (Figure 3.19b) showed that the H_2 production rate increased by ~2 times after the photon energy was introduced, while decreased back to 900 μmol $g_{catalyst}^{-1}$ min^{-1} after the illuminate was removed, suggesting that the dehydrogenation of ethanol reaction over $Ni_{0.04}Cu$ was light-sensitive. The photo-enhancement in activity showed superiority at low temperature, since the enhancement for H_2 production rate of $Ni_{0.04}Cu$ (calculated by the rate with light irradiation divided by the rate in dark condition) declined from 3.3 to 1.7 times with the temperature increasing from 170 to 210 °C (Figure 3.20a). The rate difference of $Ni_{0.04}Cu$ was also calculated by the reaction rate with light irradiated minus the reaction rate in dark conditions. Figure 3.20b showed that the rate difference of $Ni_{0.04}Cu$ increased with the increasing reaction temperature before 200 °C, and then decreased. Moreover, as shown from Figure 3.21a, the $Ni_{0.04}Cu$ catalysts displayed good stability under dark and light conditions in 5-hour reaction. Compared with $Ni_{0.04}Cu$, pure Ni demonstrated lower activity and severe deactivation (Figure 3.21b).

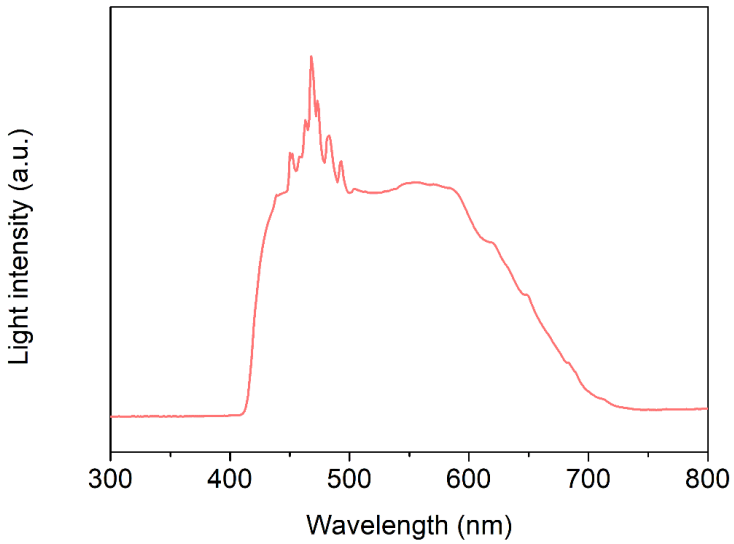

Figure 3.18 Output irradiance of light source in the photo-assisted thermal catalytic reaction

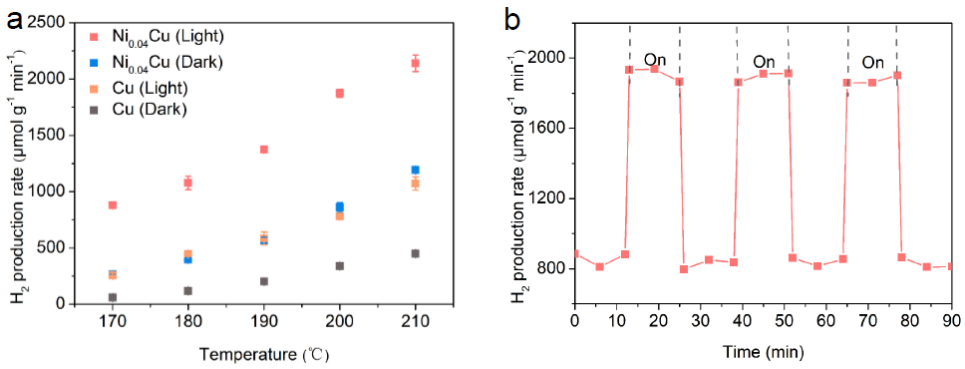

Figure 3.19 (a) Reaction rate of H_2 production on the Cu and Ni-Cu bimetallic catalysts as a function of temperature under the purely thermal condition (dark) and under photo-assisted thermal condition (light), (b) H_2 production rate on $Ni_{0.04}Cu$ catalyst with and without visible light irradiation at 200 °C.

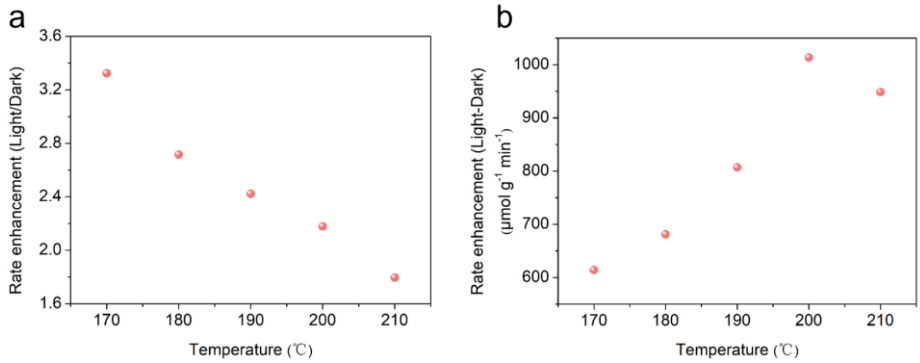

Figure 3.20 (a) Rate enhancement (H_2 production rate rate with light irradiation divided by the rate in dark condition) as a function of temperature, (b) Difference in H_2 production rate between dark and light conditions as a function of temperature.

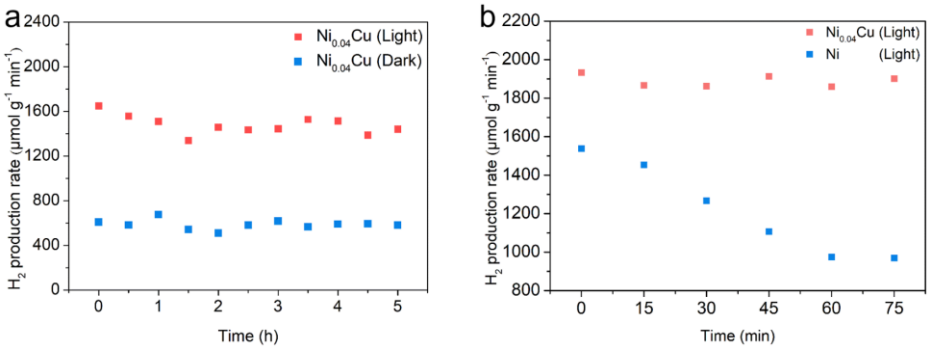

Figure 3.21 (a) Stability measurement of $Ni_{0.04}Cu$, (b) Reaction rate of H_2 production on the Ni and $Ni_{0.04}Cu$ catalysts with visible light irradiation at 200 °C.

The visible light intensity dependent H_2 production rate was carried out to identify the mechanism for enhanced photocatalytic activity of $Ni_{0.04}Cu$, and the result showed that the reaction rate presented a linear dependence on the light intensity, indicating that the hot carriers induced by visible light played a critical role in the photo-enhanced ethanol dehydrogenation reaction over $Ni_{0.04}Cu$ catalysts (Figure 3.22).[24, 25] To verify the enhanced activity was attributed to the LSPR effect of Cu, the impact of different irradiation wavelengths on the reaction rate of $Ni_{0.04}Cu$ catalysts were measured. The monochromatic light filter (MIF-W type 470, 520, 570, 620 nm) coupled with HA30 and L42 filters were utilized in reaction to obtain the desired wavelength range. By the irradiation of light, $Ni_{0.04}Cu$ showed a broad absorption peak of around 580 nm, which could be attributed to the LSPR peak of Cu. The tendency of apparent quantum efficiency (AQE) of $Ni_{0.04}Cu$ catalysts were consistent with its optical absorption spectrum, indicating that the enhancement of photocatalytic activity was attributed to the excitation of hot carriers. The hot electrons induced by a wavelength of 620 nm might be not energetic enough for realizing ethanol dehydrogenation reaction (Figure 3.23).

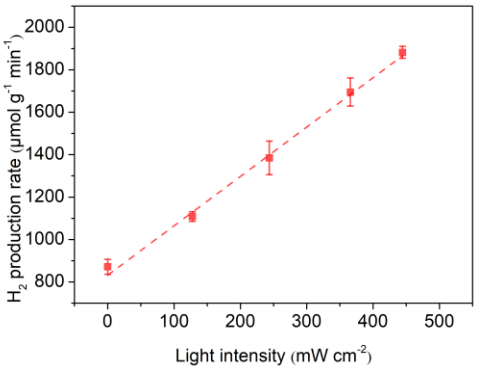

Figure 3.22 Dependence of H_2 production rate of $Ni_{0.04}Cu$ at 200 °C on light intensity.

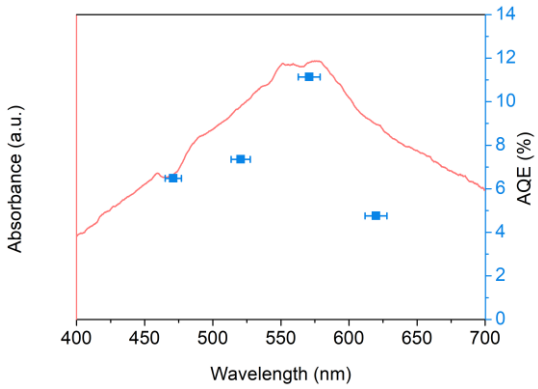

Figure 3.23 Light absorption and AQE values of $Ni_{0.04}Cu$ at 200 °C with light irradiation in different wavelength ranges.

The reaction kinetics of the ethanol dehydrogenation reaction under dark and with light irradiation at a reaction temperature from 170-210 °C were investigated to understand the underlying reaction mechanism. The apparent activation energy was calculated by fitting the reaction rates by using the Arrhenius equation ($\ln r = -E_a/RT + \ln A$), as shown in Figure 3.24 The apparent activation energy of pure Cu in the dark condition was 92.4 kJ mol^{-1}, and it decreased to 61.2 kJ mol^{-1} under the visible light irradiation, indicating that the visible light could provide additional energy for the surface reaction to reduce the apparent activation energy. The apparent activation energy was further reduced when a little amount of Ni was deposited on the surface of Cu. As shown in Figure 3.24, $Ni_{0.04}Cu$ exhibited an activation energy of 67.4 kJ mol^{-1} even without light irradiation. Under the visible light irradiation, the apparent activation energy of $Ni_{0.04}Cu$ remarkably decreased to 41.5 kJ mol^{-1}, demonstrating that photo-induced hot carriers greatly assisted the dehydrogenation process of ethanol.

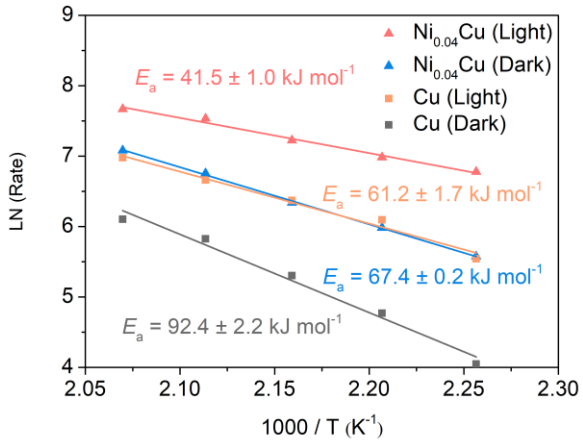

Figure 3.24 Arrhenius plots for H_2 production rate under dark and light conditions over pure Cu and $Ni_{0.04}Cu$ catalysts, error bars represent the standard deviation of three measurements with the same catalysts.

In situ DRIFT spectra were employed to further investigate the effect of hot carriers on ethanol dehydrogenation reaction. Figure 3.25 showed the infrared (IR) absorption spectra of $Ni_{0.04}Cu$ with ethanol at 200 °C under dark and light conditions. Based on the literature results, the sharp bands at 3744 cm^{-1} could be attributed to the isolated silanol groups,[46] whereas the features centered at 3670 cm^{-1} and 1250 cm^{-1} were assigned to O-H stretching and bending frequencies.[47] Two dominant peaks at 2985 cm^{-1} and 2905 cm^{-1} could be attributed to CH_3 and CH_2 asymmetric stretching.[34] The peak centered at 1050

cm^{-1} was characteristic of C-O stretching.[47] Comparatively, upon light irradiation, the intensity of each peak was substantially attenuated, indicating that a more facile activation of the adsorbed intermediates could be achieved with the aid of photo-induced hot carriers. Since the most peaks of ethoxy species (CH_3CH_2O*) and molecularly adsorbed ethanol (CH_3CH_2OH*) overlapped, it was difficult to distinguish from IR spectra. However, the presence of OH peak (1250 and 3670 cm^{-1}) indicated that the adsorbed ethanol was a stable and dominant intermediate. Upon the light irradiation, the intensity of O-H stretching and bending frequencies (1250 and 3670 cm^{-1}) decreased obviously, indicating the formation of more ethoxy intermediates (CH_3CH_2O*). The adsorbed ethoxy species could lose one hydrogen atom to form acetaldehyde or it could gradually lose more hydrogen atoms by sequential C-H bond scission. Meanwhile, two peaks at 1723 and 1756 cm^{-1}, associated with C=O stretching vibration of acetaldehyde, were observed after introducing light.[47] In addition, the broad peak at 2728 cm^{-1} also indicated the generation of acetaldehyde upon light irradiation.[47]

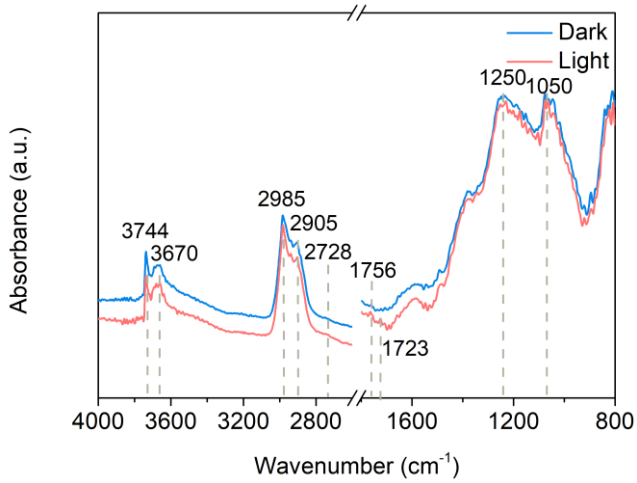

Figure 3.25 *In-situ* DRIFT spectra of $Ni_{0.04}Cu$ catalysts under dark and light conditions.

3.3.4 First-principles molecular dynamics simulation

In the limited duration time of simulation (i.e. less than a few picoseconds) at around 200 °C, no stable adsorption of ethanol molecule on the Ni-doped Cu metallic slab surface was observed, although ethanol molecules often collided with the surface. It was implied that the system was thermally mild for reactant molecules. To save a computational cost although much longer-term simulation might bring us spontaneous molecular dissociation, one of the ethanol molecules was manually decomposed into CH_3CHO and 2 H atoms

near the metallic slab surface. Then, the molecular dynamics of the system were observed for a picosecond. It was found that the CH_3CHO molecule moved away from the near-surface to the free space, but the H atoms were strongly adsorbed to surficial metallic atoms.

Figure 3.26 showed (a) the snapshot of the thermal equilibrium structure of the system, (b) the local structure of proton-metal adsorbate (-M-H), and (c) - (m) the electronic properties of the Cu slab doped with Ni on which -H are adsorbed in presence of one acetaldehyde and three ethanol molecules when one of ethanol molecule collides with the surface. Each detailed weight profile (c) - (m) of atomic orbital wavefunction components was obtained by projecting the eigen-wave-function onto the corresponding atomic orbital(s). The atomic distances of Cu-H and Ni-H fluctuated in the range roughly 1.7~2.0 Å and 1.6~1.8 Å and those at the moment of the snapshot in the Figure 3.26 (b) were 1.78 Å, 1.81 Å, and 1.65 Å, respectively. In the electronic properties,[48, 49] only significant components were presented. The electrons in the system occupied up to -4.25 eV as indicated by the black solid line in (c ~ m). The occupied states were spanned mostly by Cu 3d ((c) for all 184 Cu atoms) and 4s ((d) for all 184 Cu atoms) orbitals components and the unoccupied states in the energy range from -4.25 to -2 eV were also composed dominantly of the Cu 3d and 4s orbitals. Investigating the components of the unoccupied Ni 3d ((e) for all 8 Ni atoms) states and the unoccupied H 1s states in the metallic atom - proton adsorbates (-M-H), some interesting electronic properties were found. Unoccupied Ni 3d band was situated in the energy range from -4.25 roughly to -2 eV (dominantly from -4.25 to -3 eV) and, at the same time, the unoccupied H 1s component ((f) for just one H atom (Figure 3.26 (b)) of the dissociated two H atoms (a)) originating from the absorbed -H on the Cu-based metallic slab were also located mainly in the range from -3.7 to -2.9 eV as underlined in pale orange, which was just around the Ni 3d band. Based on the electronic properties, it could be elucidated that the electrons in 3d and 4s orbitals of Cu were excited to the unoccupied 3d and 4s orbitals of Cu under visible light irradiation and simultaneously the energetic electrons could be distributed to the unoccupied 3d band of Ni, and further transferred into the unoccupied H 1s orbitals of the -Cu-H-Ni- adsorbates. Further detailed electronic properties on the local area of the -Cu-H-Ni- adsorbate (Figure 3.26 b) were presented in Figure 3.26 (j) - (m) using the same transverse range for easy direct comparison. It indicated that the unoccupied H1s band was hybridized with the unoccupied Ni 3d band much better than with the unoccupied Cu

3d band or Cu 4s band. Therefore, the photo-excited hot electrons were easily transferred to the proton adsorbed at the surface with suppressing the non-effective carrier recombination, leading to the promotion of H_2 production.

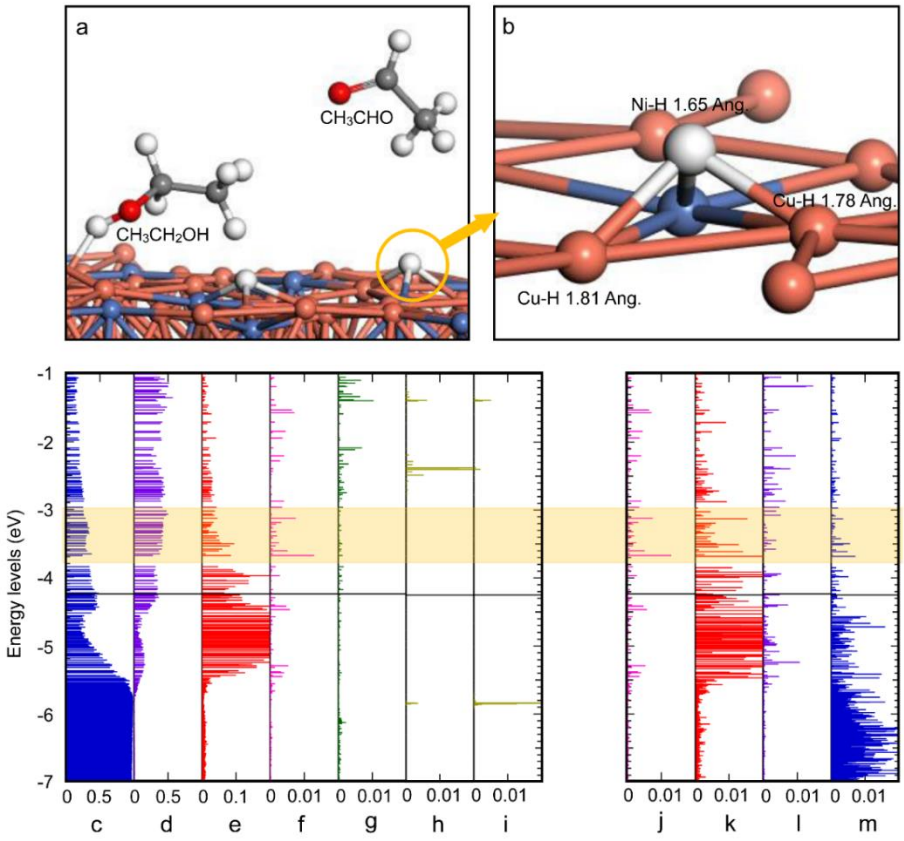

Figure 3.26 First-principles molecular dynamics simulation of $Ni_{0.04}Cu$ in the reaction molecular of CH_3CH_2OH and CH_3CHO. (a) Snapshot of the equilibrium structure at 200 °C of the Cu metal doped with Ni atoms, which is intended to mimic $Cu_{1-\delta}Ni_\delta/SiO_2$ systems, in the presence of ethanol and acetaldehyde molecules. The color code is white for H, red for O, gray for C, brown for Cu, and cyan for Ni, (b) Local adsorbate structure of -Ni-H-Cu- at the slab surface, (c-m) Corresponding electronic structures of the system, (c) Cu 3d, (d) Cu 4s, (e) Ni 3d, (f) H 1s at the surface, (g) H 1s of all H in CH_3CH_2OH colliding with the surface, (h) H 1s of all H of $-CH_3$ in CH_3CHO, (i) H 1s of -CHO in CH_3CHO, (j) H 1s at the surface, (k) Ni 3d of -Ni-H 1.65 Ang. at the surface, (l) Cu 4s of -Cu-H 1.78 Ang. at the surface, (m) Cu 3d of -Cu-H 1.78 Ang. at the surface; Black solid line indicates the Fermi level.

3.4 Conclusions

In summary, our study demonstrated that ethanol dehydrogenation for the production of H_2 and acetaldehyde could be efficiently driven by focused solar light over Ni-Cu bimetallic catalysts (Figure 3.27). High solar-to-fuel conversion efficiency of 3.81% and hydrogen production rate (2943 μmol $g_{catalyst}^{-1}$ min^{-1}) could be achieved under simulated 5.7 Suns irradiation without any additional thermal energy input. Mechanistic investigations revealed that the synergistic effects of photothermal heating and hot carrier generation through the excitation of surface plasmon resonance over Ni-Cu bimetallic catalysts played critical roles for the observed high activity and decreased activation energy. First-principles molecular dynamics simulation revealed that the hot electrons were generated from Cu and migrated to Ni atom, facilitating the formation of hydrogen and suppressing the non-effective carrier recombination. This study provides a new promising strategy to activate industrial useful and tough reactions by using renewable solar energy and the construction of efficient plasmonic photocatalysts.

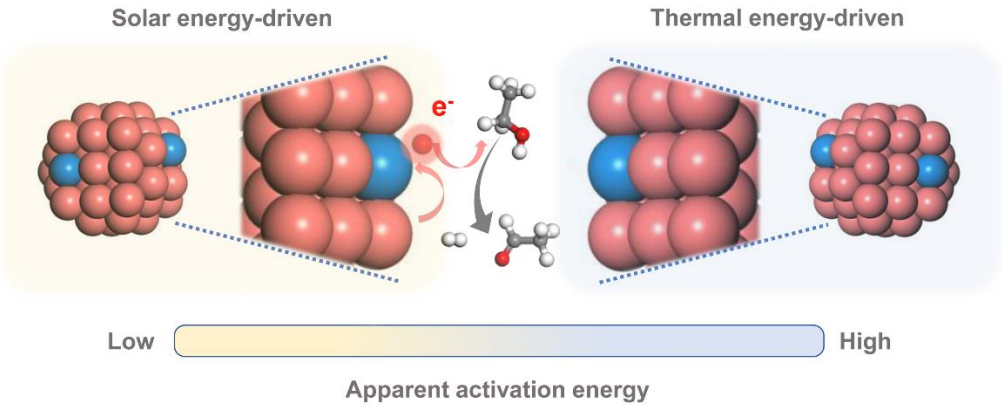

Figure 3.27 Schematic illustration of the reaction mechanism for solar-driven ethanol dehydrogenation over Ni-Cu bimetallic catalysts.

References

1. M.Z. Jacobson, W.G. Colella, D.M. Golden, *Science*, 2005, **308**, 1901-1905.

2. I. Staffell, D. Scamman, A. Velazquez Abad, P. Balcombe, P.E. Dodds, P. Ekins, N. Shah, K.R. Ward, *Energ. Environ. Sci.*, 2019, **12**, 463-491.

3. L. Zhao, Y. Qi, L. Song, S. Ning, S. Ouyang, H. Xu, J. Ye, *Angew. Chem. Int. Ed.*, 2019, **58**, 7708-7712.

4. S.T. Wismann, J.S. Engbæk, S.B. Vendelbo, F.B. Bendixen, W.L. Eriksen, K. Aasberg-Petersen, C. Frandsen, I. Chorkendorff, P.M. Mortensen, *Science*, 2019, **364**, 756-759.

5. B. Wang, S. He, L. Zhang, X. Huang, F. Gao, W. Feng, P. Liu, *Appl. Catal. B-Environ*., 2019, **243**, 229-235.

6. U. Caudillo-Flores, M.J. Muñoz-Batista, M. Fernández-García, A. Kubacka, *Appl. Catal. B-Environ*., 2018, **238,** 533-545.

7. A.V. Puga, A. Forneli, H. García, A. Corma, *Adv. Funct. Mater*., 2014, **24**, 241-248.

8. A. Segawa, A. Nakashima, R. Nojima, N. Yoshida, M. Okamoto, *Ind. Eng. Chem. Res*., 2018, **57**, 11852-11857.

9. P. Liu, E.J. Hensen, *J. Am. Chem. Soc*., 2013, **135**, 14032-14035.

10. E. Taboada, I. Angurell, J. Llorca, *J. Catal*., 2014, **309**, 460-467.

11. M.J. Sampaio, J.W.L. Oliveira, C.I.L. Sombrio, D.L. Baptista, S.R. Teixeira, S.A.C. Carabineiro, C.G. Silva, J.L. Faria, *Appl. Catal. A-Gen*., 2016, **518**, 198-205.

12. X. Zhang, L. Luo, R. Yun, M. Pu, B. Zhang, X. Xiang, *ACS Sustain. Chem. Eng*., 2019, **7**, 13856-13864.

13. C. Lu, J. Li, G. Chen, B. Li, Z. Lou, *Nanoscale*, 2019, **11**, 12774-12780.

14. M. Murdoch, G. I. Waterhouse, M. A. Nadeem, J. B. Metson, M. A. Keane, R. F. Howe, J. Llorca, H. Idriss, *Nat. Chem*., 2011, **3**, 489-492.

15. C. Kim, B.L. Suh, H. Yun, J. Kim, H. Lee, *ACS Catal*, 2017, **7**, 2294-2302.

16. L. Zhou, D.F. Swearer, C. Zhang, H. Robatjazi, H. Zhao, L. Henderson, L. Dong, P. Christopher, E.A. Carter, P. Nordlander, N.J. Halas, *Science*, 2018, **362**, 69-72.

17. H. Robatjazi, H. Zhao, D.F. Swearer, N.J. Hogan, L. Zhou, A. Alabastri, M.J. McClain, P. Nordlander, N.J. Halas, *Nat. Commun*., 2017, **8**, 27.

18. D. Gao, W. Liu, Y. Xu, P. Wang, J. Fan, H. Yu, *Appl. Catal. B-Environ*., 2020, **260**, 118190.

19. X. Meng, L. Liu, S. Ouyang, H. Xu, D. Wang, N. Zhao, J. Ye, *Adv. Mater*., 2016, **28**, 6781-6803.

20. Z.J. Wang, H. Song, H. Liu, J. Ye, Coupling of Solar Energy and Thermal Energy for Carbon Dioxide Reduction: Status and Prospects, Angew. Chem. Int. Ed., 2020, **59**, 2-22.

21. M. Ghoussoub, M. Xia, P.N. Duchesne, D. Segal, G. Ozin, *Energ. Environ. Sci.*, 2019, **12**, 1122-1142.

22. M.Q. Yang, L. Shen, Y. Lu, S.W. Chee, X. Lu, X. Chi, Z. Chen, Qi.H. Xu, U. Mirsaidov, G.W. Ho, *Angew. Chem. Int. Ed*., 2018, **58**, 3077-3081.

23. S. Kim, J.M. Kim, J.E. Park, J.M. Nam, *Adv. Mater*., 2018, **30**, 1704528.

24. H. Song, X. Meng, Z.J. Wang, Z. Wang, H. Chen, Y. Weng, F. Ichihara, M. Oshikiri, T. Kako, J. Ye, *ACS Catal*., 2018, **8**, 7556-7565.

25. H. Song, X. Meng, T.D. Dao, W. Zhou, H. Liu, L. Shi, H. Zhang, T. Nagao, T. Kako, J. Ye, *ACS Appl. Mater. Inter.*, 2018, **10**, 408-416.

26. H. Song, X. Meng, Z.-j. Wang, H. Liu, J. Ye, *Joule*, 2019, **3**, 1606-1636.

27. U. Aslam, V.G. Rao, S. Chavez, S. Linic, *Nat. Catal*., 2018, **1**, 656-665.

28. X.Y. Gan, E.L. Keller, C.L. Warkentin, S.E. Crawford, R.R. Frontiera, J.E. Millstone, *Nano Lett*., 2019, **19**, 2384-2388.

29. J. Chen, J. Feng, F. Yang, R. Aleisa, Q. Zhang, Y. Yin, *Angew. Chem. Int. Ed*., 2019, **58**, 9275-9281.

30. J. Jiao, R. Lin, S. Liu, W.C. Cheong, C. Zhang, Z. Chen, Y. Pan, J. Tang, K. Wu, S.F. Hung, H.M. Chen, L. Zheng, Q. Lu, X. Yang, B. Xu, H. Xiao, J. Li, D. Wang, Q. Peng, C. Chen, Y. Li, *Nat Chem*., 2019, **11**, 222-228.

31. A. Carrero, J.A. Calles, A.J. Vizcaíno, *Appl. Catal. A-Gen*., 2007, **327**, 82-94.

32. J. Shan, N. Janvelyan, H. Li, J. Liu, T.M. Egle, J. Ye, M.M. Biener, J. Biener, C.M. Friend, M. Flytzani-Stephanopoulos, A*ppl. Catal. B-Environ*., 2017, **205**, 541-550.

33. M.D. Marcinkowski, M.T. Darby, J. Liu, J.M. Wimble, F.R. Lucci, S. Lee, A. Michaelides, M. Flytzani-Stephanopoulos, M. Stamatakis, E.C.H. Sykes, *Nat Chem*., 2018, **10**, 325-332.

34. J. Shan, J. Liu, M. Li, S. Lustig, S. Lee, M. Flytzani-Stephanopoulos, *Appl. Catal. B-Environ*., 2018, 226, 534-543.

35. H. Huang, M. Mao, Q. Zhang, Y. Li, J. Bai, Y. Yang, M. Zeng, X. Zhao, *Adv. Energy Mater*., 2018, **8**, 1702472-1702482.

36. D.R. Lide, *CRC Handbook of Chemistry and Physics*, 84th Edition, 2003.

37. R. Car, M. Parrinello, *Phys. Rev. Lett*., 1985, **55**, 2471-2474.

38. A. Marimuthu, J. Zhang, S. Linic, *Science*, 2013, **339**, 1590-1593.

39. B. Qiao, A. Wang, X. Yang, L.F. Allard, Z. Jiang, Y. Cui, J. Liu, J. Li, T. Zhang, *Nat. Chem*., 2011, **3**, 634-641.

40. Z. Zhang, Y. Zhu, H. Asakura, B. Zhang, J. Zhang, M. Zhou, Y. Han, T. Tanaka, A. Wang, T. Zhang, N. Yan, *Nat. Commun*., 2017, **8**, 16100.

41. L. Wang, W. Zhang, S. Wang, Z. Gao, Z. Luo, X. Wang, R. Zeng, A. Li, H. Li, M. Wang, X. Zheng, J. Zhu, W. Zhang, C. Ma, R. Si, J. Zeng, *Nat. Commun*., 2016, **7**, 14036.

42. H. Li, L. Wang, Y. Dai, Z. Pu, Z. Lao, Y. Chen, M. Wang, X. Zheng, J. Zhu, W. Zhang, R. Si, C. Ma, J. Zeng, *Nat. Nanotechnol*., 2018, **13**, 411-417.

43. X. Fang, Q. Shang, Y. Wang, L. Jiao, T. Yao, Y. Li, Q. Zhang, Y. Luo, H.L. Jiang, *Adv. Mater*., 2018, **30**, 1705112-1705118.

44. N.D. Subramanian, C.S.S.R. Kumar, K. Watanabe, P. Fischer, R. Tanaka, J.J. Spivey, *Catal. Sci. Technol*., 2012, **2**, 621-631.

45. S.F. Moya, R.L. Martins, M. Schmal, *Appl. Catal.A-Gen*., 2011, **396**, 159-169.

46. V.L. Sushkevich, I.I. Ivanova, E. Taarning, *ChemCatChem*, 2013, **5**, 2367-2373.

47. A. Kumar, A. Ashok, R.R. Bhosale, M.A.H. Saleh, F.A. Almomani, M. Al-Marri, M.M. Khader, F. Tarlochan, *Catal. Lett*., 2016, **146**, 778-787.

48. B.G. Johnson, P.M.W. Gill, J.A. Pople, *J. Chem. Phys*., 1993, **98**, 5612-5626.

49. M. Oshikiri, J. Ye, M. Boero, *J. Phys. Chem. C*, 2014, **118**, 8331-8341.

Chapter 4 Exploiting water and methanol activation for solar-driven H_2 production: interplay of dual active sites over plasmonic ZnCu alloy

4.1 Introduction

Hydrogen has attracted growing interest since it is considered as a promising alternative clean energy that can be used in various fields, especially in polymer electrolyte membrane fuel cells (PEMFCs).[1, 2] However, the physical properties of H_2 make storage and transportation difficult, which hinder its practical application.[3] The liquid organic hydrogen carriers (LOHCs) concept, including the transportation of H_2 in liquids and *in-situ* production of H_2 through activating certain chemical bonds of LOHCs in the presence of catalysts, offers a prospective approach to solve the storage and transportation issues of H_2.[4] Due to the merits of high H_2 storage density (99 kg m^{-3}), high safety, easy transport and low cost, methanol (CH_3OH) is regarded as an ideal candidate for LOHCs.[5] Thermocatalytic production of H_2 by methanol steam reforming (MSR) reaction ($CH_3OH + H_2O = 3H_2 + CO_2$) at high temperature (200-350 °C) with production of 3 moles of H_2 from 1 mole of CH_3OH is an attractive process, and the supported metallic nanoparticles (NPs), such as Pt, Pd, Au, and Cu, are generally employed as the catalysts.[6, 7] To achieve highly efficient MSR under milder reaction conditions, both methanol and water molecules need to be activated effectively.[8, 9] To this end, a previous study reported PdZn surface alloys for efficient MSR due to the predominant transformation of methanol to formaldehyde and the effective activation of water by forming ZnOH species.[10] Recently, Ma and co-authors designed atomically dispersed Pt/α-MoC and Ni/α-MoC catalysts that enabled both efficient methanol and water dissociation by isolated Pt or Ni sites and α-MoC, respectively, thus leading to exceptional low-temperature H_2 production from methanol aqueous solution.[11, 12] Despite the impressive activities, noble metals and/or relatively high temperature (> 190 °C) are still required, resulting in high capital costs and consuming massive heat energy from electric energy or the combustion of fossil fuels. Therefore, it is of great significance to develop a cost-effective and sustainable catalytic process for MSR by constructing low-cost catalysts with outstanding ability for both methanol and water activation as well as using clean and renewable energy input.

Chapter 4

An innovative and sustainable strategy for initiating catalytic reactions is to utilize the solar energy.[13-16] In fact, photocatalytic H_2 production from CH_3OH/H_2O solution has been extensively investigated using either particulate semiconductors or photosensitizers coupled with cocatalysts, but is commonly inefficient because of the limitations of photogenerated carriers transfer processes and poor sunlight harvesting property of typical photocatalysts in the visible and near infrared spectral regions.[17-20] Although significant progresses have been made recently, the state-of-the-art photocatalytic H_2 production rate from methanol aqueous solution remains at several mmol g^{-1} h^{-1}, far behind the demands of industrialization. Recently, plasmonic nanostructures (such as Au, Ag, and Cu), which can efficiently harness and convert solar energy into energetic "hot carriers" and heat synergistically through the excitation of localized surface plasmon resonance (LSPR), have emerged as promising photocatalysts for efficient solar-to-chemical energy conversion.[21-26] Due to the good LSPR property and low price, Cu has attracted much attention for plasmonic catalysis, yet suffers from low catalytic activity and stability.[24, 27] The construction of alloy NPs by integrating the plasmonic NPs with catalytically active components is a powerful strategy for mediating the catalytic properties due to the electronic and geometric effects. For instance, Halas et al. reported plasmonic CuRu alloy NPs for light-driven methane dry reforming with greatly enhanced activity and stability.[25] Similar material design concept was also applied into other plasmonic complexes, such as Al-Pd,[28] Cu-Ni,[29] and Al-Ir.[30] These concepts of catalyst design inspire us to utilize the solar energy solely as the energy input to initiate the MSR through constructing efficient plasmonic photothermal catalysts. Considering the excellent visible-light response for hot carrier excitation and the good ability for activating C-H bond over Cu NPs, I reasoned that the modification of Cu by other components with an outstanding capacity for water activation could bring a further catalytic activity enhancement towards solar-driven MSR.

Here, a highly efficient solar-driven MSR process (without additional thermal energy input) for selectively production of H_2 over plasmonic ZnCu alloy catalyst is reported. Under the irradiation of simulated solar light at the maximum light intensity of 788 mW cm^{-2}, a remarkable H_2 production rate of 328 mmol $g_{catalyst}^{-1}$ h^{-1} with a high solar energy conversion efficiency of 1.2% are achieved over $Zn_{1.3}Cu_{98.7}$. Mechanistic investigations suggest that the introduction of Zn into Cu can enhance water dissociation with lower activation energy and promote the transfer of hot electrons from Cu to Zn sites, thus

further facilitating the activation of water and methanol. Bifunctional nature of the interface between Zn and Cu together with their unique hot carrier transfer and activation capacity endow the ZnCu catalysts with outstanding activity towards solar-driven MSR.

4.2 Experimental section

4.2.1 Materials preparation

Wet chemistry method was employed to synthesize the ZnCu alloy nanoparticles with different Zn/Cu atomic ratio. To prepare the ZnCu alloy nanoparticles, 20 mL of ascorbic acid solution (0.1 M) was added to 100 mL aqueous solution containing Cu $(NO_3)_2 \cdot 3H_2O$ (1 mM) and PVP (200:1 M ratio of Cu to PVP), followed by adding certain amounts of Zn $(NO_3)_2 \cdot 6H_2O$ into above solution with continuous stirring. After stirring for 30 min, 20 mL (0.1 M) of $NaBH_4$ was drop-wisely added into the above solution to reduce the metal ion into metallic states. The solution was stirred at room temperature in the Ar atmosphere to prevent the oxidation of metallic nanoparticle. Afterward, 500 mg of SiO_2, as the supporter for the metallic nanoparticles, was added in the solution, followed by stirring for 30 min and ultra-sonicating for 10 min. The precipitates were collected by using a centrifuge, wished by deionized water three times, and then dried at 70 $^{\circ}$C overnight. Finally, the catalysts were calcinated at 350 ℃ in the air for 4h. Before the activity measurement, catalysts were *in-situ* reduced in H_2 atmosphere at 350 ℃ for 1h to prepare the SiO_2 supported ZnCu alloy nanoparticles (named as ZnCu here and after). For comparison, pure Cu nanoparticles supported on SiO_2 were synthesized without adding the Zn $(NO_3)_2 \cdot 6H_2O$. Noble-metal-based (Pt, Pd, and Au) catalysts were prepared using standard impregnation method, and SiO_2 was used as catalyst supporter. The theoretical mass ratio between metal and supporter was controlled to be 1.0 wt %.

4.2.2 Material characterization

X-ray diffraction (XRD) patterns were obtained on an X-ray powder diffractometer with Cu Kα radiation (PANalytical). The surface electronic states of catalysts were characterized by an X-ray photoelectron spectroscopy (XPS, Escalab 250 Xi, Thermo Scientific). Ultraviolet-visible absorption spectra were collected using a UV/Vis spectrophotometer (UV-2600, Shimadzu). Transmission electron microscopy (TEM) and high-resolution transmission electron microscopy (HRTEM) experiments were carried out using a JEOL JEM-ARM200F transmission electron microscope. The chemical

compositions of catalysts were analyzed by an inductivity coupled plasma optical emission spectrometer (ICP-OES, iCAP 6300, Thermo Scientific). Diffuse reflectance infrared Fourier transform spectroscopy (DRIFTS) measurements were performed on a FT-IR-6300 system (JASCO Corp.) equipped with an *in-situ* DR cell and a liquid nitrogen-cooled mercury-cadmium-telluride detector.

4.2.3 Photocatalytic activity measurement

Two types of reactors (solar-driven catalysis reactor and photo-enhanced thermocatalytic reactor) were employed to investigate the solar-driven catalytic activity and the reaction mechanism, respectively. Solar-driven methanol steam reforming reaction was conducted in a solar-driven catalysis reactor, in which the solar energy was introduced into the reactor solely as the energy input (without additional thermal energy) for initiating the reaction. The solar-driven catalysis reactor was a home-made flow-type reactor with a quartz cover to allow the introduction of solar energy into the reactor, and the irradiation diameter was 10 mm. AM 1.5 light was used as the illuminant, and a maximum light intensity of 788 mW cm^{-2} can be achieved by a condenser. The surface temperatures of catalysts were recorded by a thermo-couple. Before catalytic activity test, the catalysts were reduced in H_2 atmosphere (10% balanced in Ar) at 350 °C for 1 h, and then dispersed in the reactor. Through the bubbler system (CH_3OH/H_2O solution, 1/1 v/v), the reaction gas was introduced into the reactor. The space velocity was controlled to be 30 mL min^{-1}. The products were quantified by gas chromatography (GC) equipped with thermal conductivity and flame ionization detector.

The solar energy conversion efficiency was calculated using

$$\eta = \frac{\alpha(mol\cdot s^{-1})\cdot \Delta H^0_{MSR}(J\cdot mol^{-1})}{light\ power\ (J\cdot s^{-1})} \times 100\%,$$

where ΔH^0_{MSR} (48.97 kJ mol^{-1}) is the standard reaction enthalpy changes of methanol steam reforming reaction.

In order to elucidate the role of the photo-induced hot carriers, the activity for photo-assisted thermocatalytic methanol steam reforming was tested in a home-made flow reactor under the atmospheric pressure. The temperature controller and thermocouple (TC-1000, JASCO) were used to heat the reaction bed and keep the catalysts at desired temperatures. Visible-light energy was provided by a LA-251 Xe lamp equipped with HA30 and L42 filters to remove the ultraviolet and infrared light. Through a quartz

window, the visible light was introduced into the reactor and irradiated on the catalysts. The diameter of the irradiation area was 8.5 mm. Temperature controller was used to mitigate the heat induced by the light irradiation. Before the activity measurement, 5 mg of catalysts were dispersed uniformly on the reaction bed of the reactor, and the catalysts were *in-situ* reduced at 350 °C for 1 h under the H_2 atmosphere (10% balanced in Ar). After cooling down to the room temperature, the reactor was flushed by Ar gas to remove the H_2. The catalytic activity measurement method was as same as the solar-driven methanol steam reforming process.

Isotopic labeling experiments for MSR were measured using D_2O (Cambridge Isotope Laboratories, Inc.) at a reaction temperature of 180 °C. The reactant gas mixture was CH_3OH and H_2O (or D_2O) produced from CH_3OH aqueous solution via bubbler system. The reaction rate was detected by gas chromatograph (GC) equipped with thermal conductivity detector and flame ionization detector. The kinetic isotope effects (KIE) under different reaction conditions were calculated by dividing the reaction rates of H_2 production from CH_3OH and H_2O by the reaction rates of H_2 production from CH_3OH and D_2O.

4.2.4 *In-situ* DRIFTS measurement

In order to elucidate the reaction role of photo-induced hot carriers and the intermediates formed during the reaction, FT-IR-6300 system (JASCO Corp.) equipped with an *in-situ* DR cell and a liquid nitrogen-cooled mercury-cadmium-telluride detector was utilized. In the DRIFTS measurement, 5 mg of catalysts were dispersed in the DR cell, and were *in-situ* reduced under the H_2 atmosphere (10% balanced in Ar) at 350 °C for 1 h. After cooling down to the room temperature, Ar gas was introduced into the DR cell to purge the H_2. The reaction gas was injected into the DR cell through the bubbler system, and the background spectrum of the system was recorded after the adsorption-desorption equilibrium was reached between the reaction gas and catalysts. Then, the DR cell was closed by cutting off the injection of reaction gas. After the temperature of DR cell was increased to 180 °C, the DRIFT spectra were recorded at the certain time to investigate the intermediates formed during the purely thermocatalytic process. Afterward, the visible light energy was introduced into the DR cell, and the DRIFT spectra were recorded at the certain time to reveal the reaction role of photo-induced hot carrier.

4.2.5 Finite difference time domain (FDTD) simulation

The spatial distribution of the electric field around the pure Cu and the $Zn_{1.3}Cu_{98.7}$ alloy plasmonic nanoparticles was calculated by means of the finite difference time domain (FDTD) method using the FullWAVE software (RSoft, Synopsys). The dielectric functions of Cu and Zn were obtained from the literature.[31, 32] Since the Zn content of the $Zn_{1.3}Cu_{98.7}$ alloy nanoparticle is low, a Maxwell-Garnett effective medium approximation was applied to calculate the effective dielectric constant of the $Zn_{1.3}Cu_{98.7}$ alloy.[33]

4.2.6 Computational details for first-principles calculation

The first-principle calculation was performed using PWSCF code from the Quantum ESPRESSO package.[34, 35] The exchange and correlation potential were used in the generalized gradient approximation (GGA) in the scheme of Perdew, Burke and Ernzerrof (PBE).[36] All the geometry structures were relaxed until energy is converged to 1×10^{-5} Ry and 1×10^{-3} eV/Å for electronic and force convergence. The projector augmented wave (PAW) method[37] with a plane-wave cutoff energy of 45 Ry was used for the real-space integration grid. Brillouin zone was sampled by 3×3×1 k-points Monkhorst-Pack grid for optimization. The DFT-D2 method was employed for van der Waals correction.[38, 39] The Cu (111) surface was modeled using a slab of 3 layers of a 3×3 unit cell which lattice parameters were a=b=15.362 Å, c = 30 Å, $\alpha = \beta = 90°$, $\gamma=120°$. In the Zn-Cu (111) modes, two Cu atoms on the Cu (111) surface were substituted by Zn atoms. The free–energy change (ΔG) of each elementary reaction step was calculated according to the computational hydrogen electrode (CHE) model suggested by Nørskov et al.[40-42] In this method, the free energy change defined as: $\Delta G = \Delta E + \Delta ZPE - T\Delta S$, where ΔE is the reaction energy directly obtained from DFT calculations, ΔZPE and ΔS are the zero point energy difference and the entropy change between the products and reactants, respectively, and T is the temperature (298.15 K). The entropies and vibrational frequencies of molecules in the gas phase were taken from the NIST database,[40] while the vibrational frequencies of adsorbed species were computed to obtain ZPE contribution in the free energy expression. Only adsorbate vibrational modes were computed explicitly, while the catalyst sheet was fixed (assuming that vibrations of the substrate are negligible).[42-45]

4.2.7 Computational details for first-principles molecular dynamics simulations

First-principles molecular dynamics simulation[46] and the electronic structure calculations based on the density functional theory within local density approximation (DFT-LDA) using pseudopotentials were carried out to demonstrate the transfer process of electrons excited from the Cu based nanoparticles to adsorbate materials. To mimic the Zn doped Cu nanoparticles loaded on a SiO_2 support particle material in presence of gas phase reactant and final products, I employed the simulation model including a slab of metal Cu (including 213 Cu atoms) exposing a (111) surface, which was doped with Zn atoms (3 Zn atoms) at the both slab surfaces and also in the inner area of the slab to check the effect of location dependence, at the bottom of the supercell. The following three kinds of reactants were prepared in the open space provided on the slab surface. [Case A] Mixed gas of 4 CH_3OH and 4 H_2O (of initial input molecules), 1 H_2 and 1 CO_2 (of final products), [Case B] Mixed gas of 4 CH_3OH, 2 H_2O, 1 H_2, 1 CO_2 in the space, and Zn-OH, Cu-H, Cu-OH, and Zn-H adsorbates on the slab surface at initial stage of simulation, [Case C] Only 10 H_2O molecules in the space above the slab surface. The detailed model specifications were described in the following section. Employing the model, we achieved the first-principles quantum molecular dynamics simulation and obtained equilibrium structure of the system at 220 °C (493 K). Then, the electronic structure was computed by solving the Kohn-Sham equation in LDA level.

Dynamical simulations were conducted within the Car-Parrinello framework (CPMD)[46] using an unrestricted spin (Local Spin Density: LSD) approach and including gradient corrections (GGA) on the exchange and correlation functional after Becke-Lee-Yang-Parr (BLYP).[47, 48] The valence-core interaction was modeled by norm-conserving Troullier-Martins (TM) pseudopotentials (PP)[49] for Cu, Zn, C, O, and H atoms. The electrons of Cu 4s, 3d; Zn 4s, 3d; C 2s, 2p; O 2s, 2p; H 1s were treated explicitly as valence electrons in molecular dynamics simulation. Those wavefunctions were expanded in a plane-wave basis set with an energy cut-off of 80 Ry, with the sampling of the Brillouin restricted to the Γ point. A fictitious electronic mass of 1200 a.u. and an integration step of 5.0 a.u. ensured a good control of the conserved quantities. The configuration of electrons and wavefunctions prepared for solving Kohn-Sham equations were almost same as those in dynamical simulations but some unoccupied states (number of unoccupied states was about 30 % of the number of occupied states) were included in the calculation to investigate the energy levels of unoccupied states. The weight profiles

of atomic orbital components were obtained by projecting the eigen-wave-function onto the corresponding atomic orbitals.[50]

Computation models: Cu metal crystal with face-centered cubic lattice, whose lattice length a is 3.615 Å (Ref. ICSD code 627115[51]) was used. Supposed that this cubic cell vectors were a, b, c (|a|=|b|=|c|), the cell vectors of the supercell used in the simulation were 3*(c-a), 3*(b-a), 2*(a+b+c) + open space thickness about 15 angstroms in (a+b+c) direction. |3*(c-a)| = |3*(b-a)| = 15.335661 angstroms, |2*(a+b+c) + open space thickness about 15 angstroms in (a+b+c) direction | = 28 angstroms. Each atomic layer had 36 atoms and the slab was formed by 6 atomic layers. The first (top) layer and the third layer and sixth layer were doped with one Zn atom by substituting one Cu atom. Therefore, the slab included 213 Cu atoms and 3 Zn atoms. The total gas pressure, for example in the Case A, corresponds to roughly 340 atms considering the temperature, the number of molecules, and the open space volume for the molecules (4 CH_3OH, 4 H_2O, 1 H_2, and 1 CO_2).

4.3 Results and discussion

4.3.1 Preparation and structural characterization of catalysts

A series of ZnCu alloy NPs were prepared by reducing Cu^{2+} and Zn^{2+} with $NaBH_4$ in the presence of ascorbic acid and polyvinylpyrrolidone (Figure 4.1a), and then loaded on SiO_2 with a weight amount of approximately 6.0% (Table 4.1). The typical atomic ratios of Zn in Cu were ranged from 0.8% to 1.8% (denoted as $Zn_{0.8}Cu_{99.2}$, $Zn_{1.3}Cu_{98.7}$, and $Zn_{1.8}Cu_{98.2}$, here and after) (Table 4.1). Due to the more positive standard electrode potential of Cu^{2+} (Cu^{2+}/Cu, $E^0 = +0.34$ V) compared with Zn^{2+} (Zn^{2+}/Zn, $E^0 = -0.76$ V), the reduction of Cu^{2+} occurred first to form Cu NPs, followed by Zn deposition on the surface of Cu, thus resulting in the formation of ZnCu surface alloy (Figure 4.1a). The X-ray diffraction (XRD) patterns (Figure 4.2) showed that both pure Cu NPs and ZnCu alloy NPs with different Zn amount exhibited the same diffraction peaks attributed to metallic Cu, and no Zn related peaks were detected, indicating that the structure of Cu NPs did not change due to the introduction of a small amount of Zn. Transmission electron microscopy (TEM) image (Figure 4.3) showed that the $Zn_{1.3}Cu_{98.7}$ NPs were dispersed on the surface of SiO_2 supporters, with an average nanoparticle size of approximately 35 nm. High resolution (HR)-TEM images showed a clear lattice fringe of 0.21 nm, consistent with the (111) plane of metallic Cu (Figure 4.1b). No Zn species were observed

in HRTEM images, revealing the high dispersion of Zn in ZnCu alloy. The reciprocal lattice spacings of Bragg spots from selected area electron diffraction (SAED) were derived from Cu NPs (Figure 4.1c), illustrating that the introduction of Zn into Cu could not affect the crystalline structure of Cu due to their similar atomic radius, in well agreement with the XRD result. The dispersion of Zn atoms in $Zn_{1.3}Cu_{98.7}$ was further investigated by using scanning transmission electron microscope energy dispersive X-ray spectrometry (STEM-EDS) mapping (Figure 4.1d-g), and the results showed that the Zn atoms were evenly distributed on the surface of Cu (Figure 4.1g, Figure 4.3b).

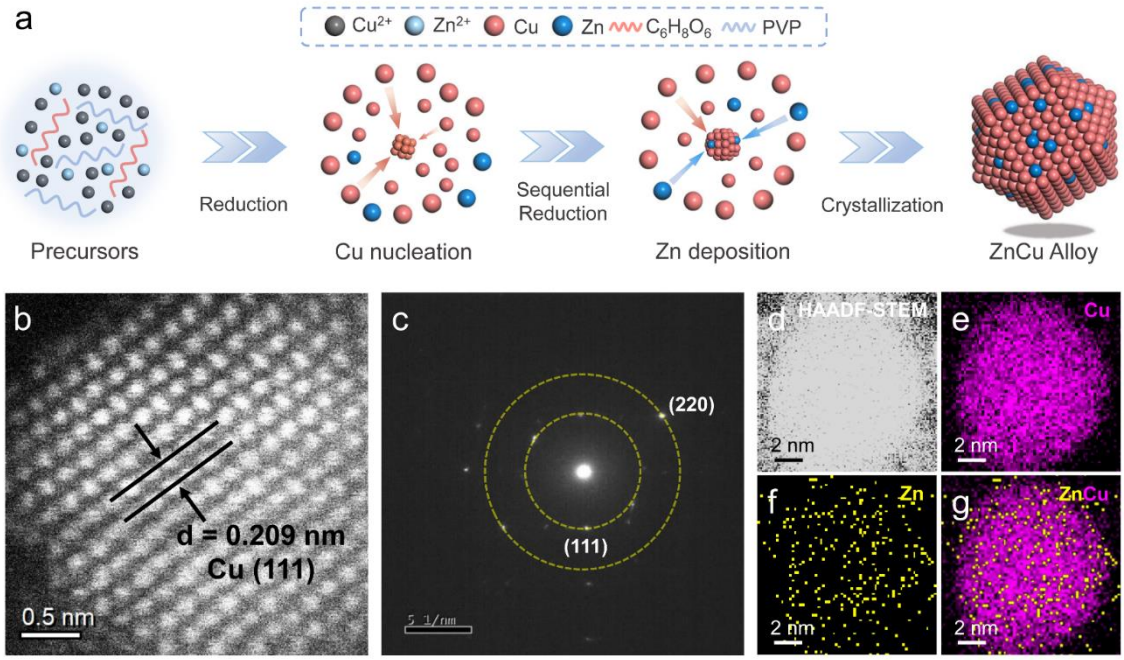

Figure 4.1 Synthesis and microstructure of catalysts. (a) Schematic illustration of fabrication process of ZnCu alloy. (b) STEM image of $Zn_{1.3}Cu_{98.7}$. (c) SAED pattern of $Zn_{1.3}Cu_{98.7}$. (d-g) STEM-EDS mapping of $Zn_{1.3}Cu_{98.7}$.

Table 4.1 Elemental analysis of the catalysts

Samples	Zn (wt. %)[a]	Cu (wt. %)[a]
$Zn_{0.8}Cu_{99.2}$	0.05	5.85
$Zn_{1.3}Cu_{98.7}$	0.08	5.76
$Zn_{1.8}Cu_{98.2}$	0.11	5.77
$Zn_{2.3}Cu_{97.7}$	0.14	5.85

a, analyzed by ICP-OES method.

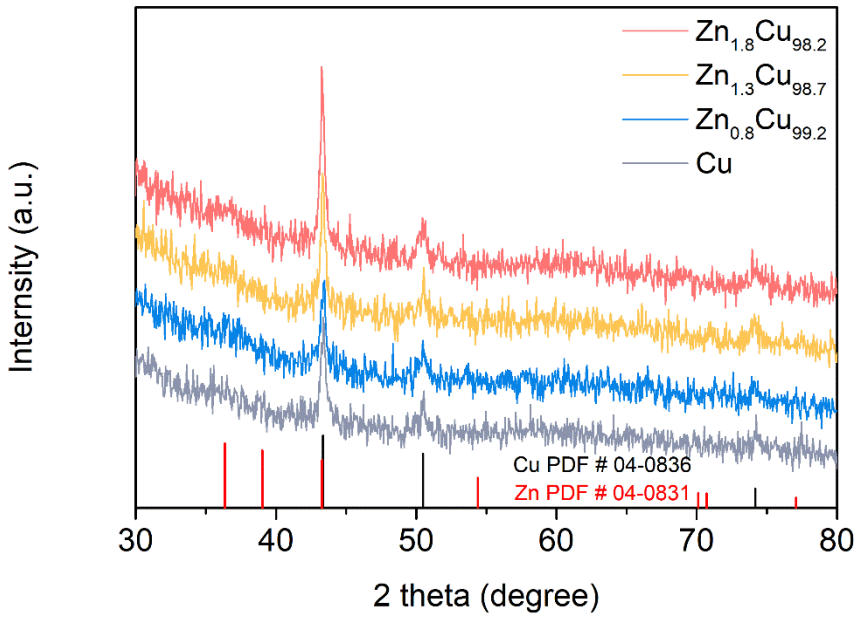

Figure 4.2 XRD patterns of pristine Cu and ZnCu alloy catalysts.

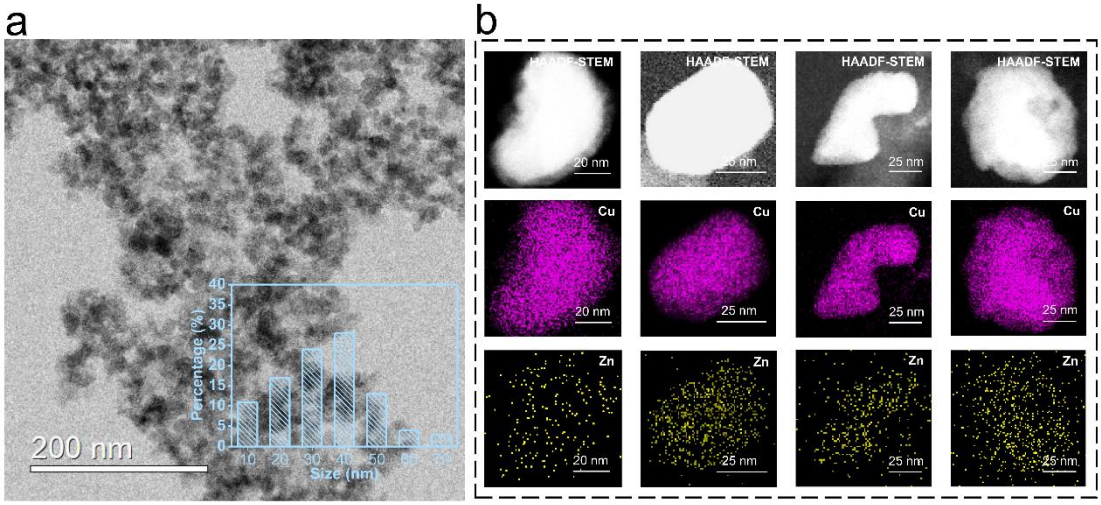

Figure 4.3 TEM image and STEM-EDS mapping of $Zn_{1.3}Cu_{98.7}$. (a) TEM image and size distribution of $Zn_{1.3}Cu_{98.7}$. (b) HAADF-STEM and EDS mapping of different $Zn_{1.3}Cu_{98.7}$ nanoparticles.

Before the catalytic activity measurement, all the catalysts were *in-situ* reduced in H_2 atmosphere at 350 °C in the reactor. The X-ray photoelectron spectroscopy (XPS) measurements were carried out to determine the surface electronic states of Cu and ZnCu alloy before and after reduction. As shown in Figure 4.4, before H_2 reduction, a Cu $2p_{3/2}$ peak at 933.6 eV assigned to the CuO along with strong satellite peaks related to Cu^{2+}

were observed in $Zn_{1.3}Cu_{98.7}$, indicating that the Cu was in the oxidation states. After reduction in H_2 atmosphere at temperature of 350 °C, the $2p_{3/2}$ peak of Cu was shifted to the binding energy of 933.0 eV with the disappearance of Cu^{2+} satellite peaks, proving that Cu was transformed into metallic states with the absence of Cu_2O or CuO in $Zn_{1.3}Cu_{98.7}$ alloy (Figure 4.4).[52] XPS Auger spectra of Cu and Zn demonstrated that both the Cu and Zn in $Zn_{1.3}Cu_{98.7}$ alloy were transformed from oxidation state into the metallic state after H_2 reduction (Figure 4.5 and 4.6). Compared with pure Cu NPs, the valence state of Cu and Zn in ZnCu alloy remained unchanged (Figure 4.7a-c). The Cu $L_3M_{45}M_{45}$ spectra in Cu and ZnCu alloy showed clear peaks at 918.6 eV, which strongly indicated that the Cu was in metallic state in both the pristine Cu and ZnCu samples (Figure 4.7b).[53] In addition, the Zn $L_3M_{45}M_{45}$ spectra were detected at 992.0 eV over ZnCu alloy catalysts, in good agreement with the Zn metal (Figure 4.7c).[54] The UV-Vis diffuse reflectance spectrum (UV-Vis DRS) of pristine Cu showed a wide absorption peak at the wavelength of 575 nm, which was ascribed to the LSPR peak of Cu. After the introduction of Zn into Cu, the position of the optical absorption peak remained almost unchanged with strong optical absorption in the visible light region (Figure 4.7d).

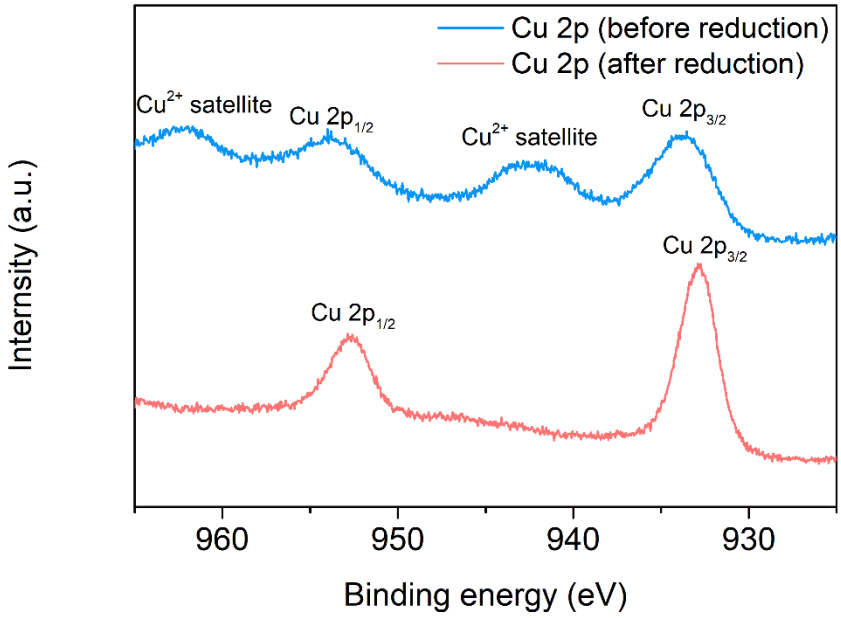

Figure 4.4 XPS Cu 2p spectrum of $Zn_{1.3}Cu_{98.7}$ catalysts before and after reduction.

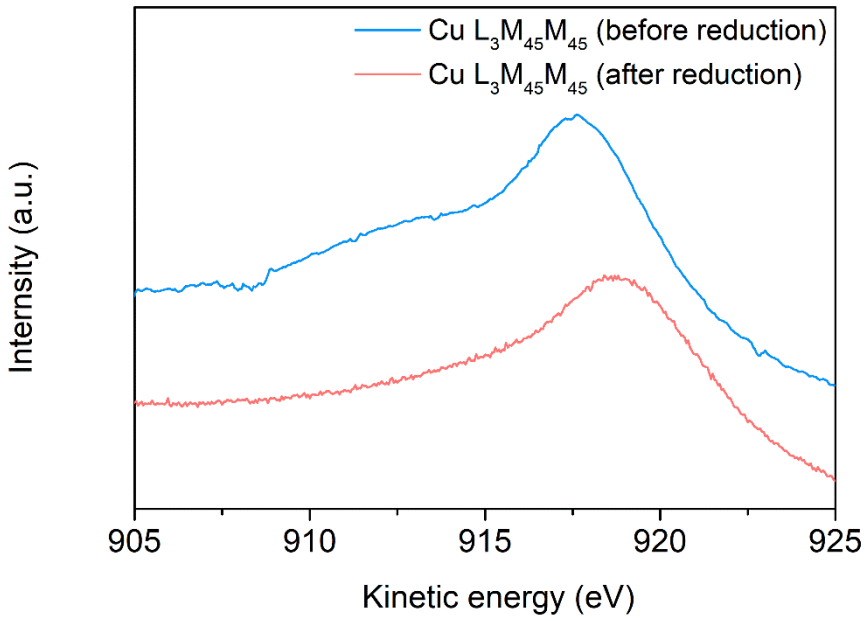

Figure 4.5. Auger spectrum of Cu $L_3M_{45}M_{45}$ over $Zn_{1.3}Cu_{98.7}$ catalysts before and after reduction.

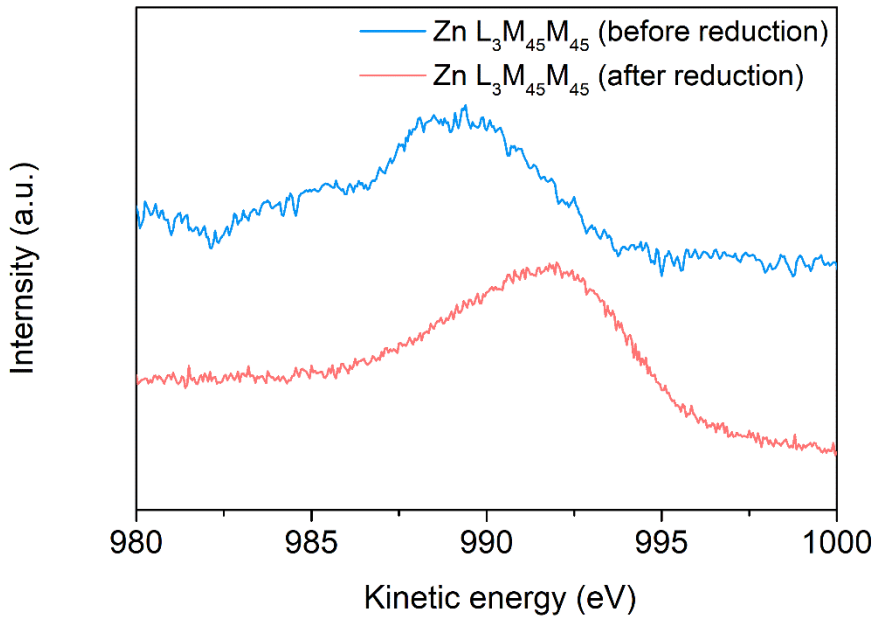

Figure 4.6. Auger spectrum of Zn $L_3M_{45}M_{45}$ over $Zn_{1.3}Cu_{98.7}$ catalysts before and after reduction.

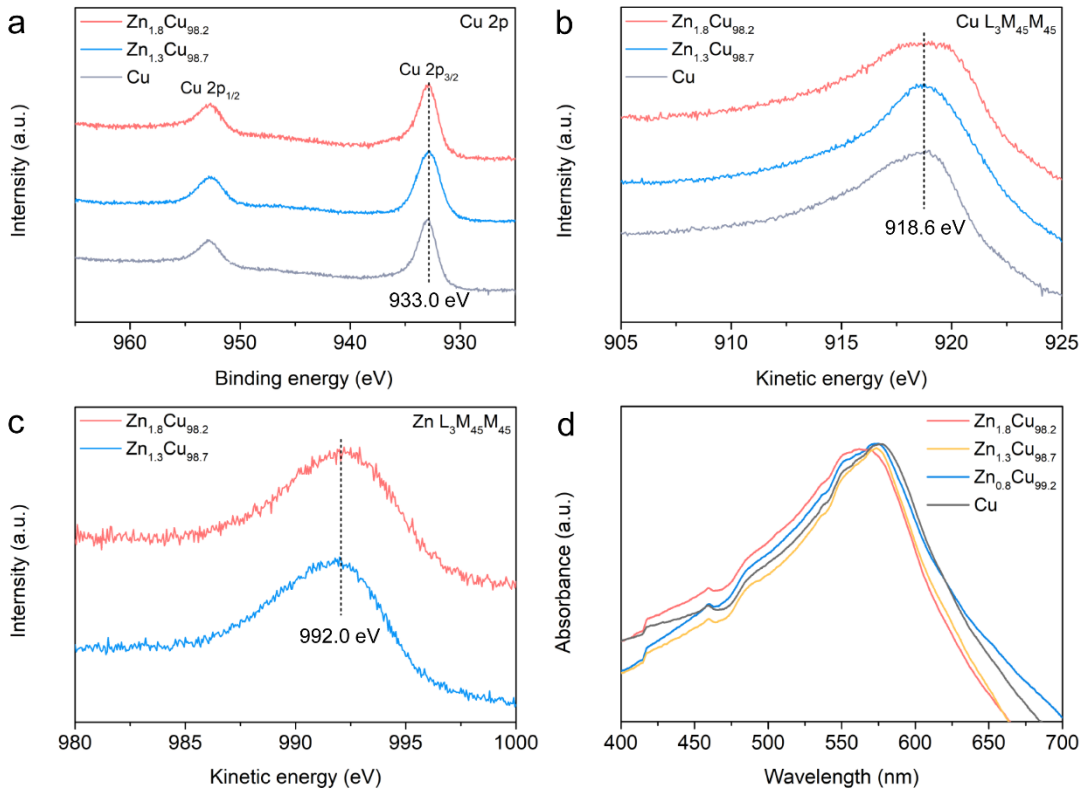

Figure 4.7 Structural characterization of Cu and ZnCu alloy catalysts. (a) XPS Cu 2p spectra of Cu and ZnCu alloy catalysts. (b) Auger spectra of Cu $L_3M_{45}M_{45}$ over Cu and ZnCu catalysts. (c) Auger spectra of Zn $L_3M_{45}M_{45}$ over ZnCu catalysts. (d) UV-Vis DRS patterns of pristine Cu and ZnCu alloy catalysts.

4.3.2 Solar-driven methanol steam reforming over ZnCu plasmonic catalysts

To test the advantage of plasmonic ZnCu alloy NPs, solar-driven MSR was conducted on the home-made solar-driven reactor (Figure 4.8). The focused simulated solar light (AM 1.5G) was used as the light source (Figure 4.9). As presented in Figure 4.10a, the surface temperatures over Cu and ZnCu alloy catalysts were measured to be roughly identical under same light irradiation and increased linearly with the light intensity, reaching approximately 250 °C at a light intensity of 788 mW cm^{-2}. The identical surface temperature revealed that introducing small amounts of Zn did not affect the photothermal conversion capacity of Cu NPs. However, the Cu and ZnCu alloy catalysts demonstrated drastically different plasmonic photothermal catalytic performances under same reaction conditions. As presented in Figure 4.10b, the H_2 production rate over Cu and ZnCu alloy catalysts increased exponentially with increasing light intensity, but all the ZnCu alloy

catalysts exhibited higher H_2 production rate than pristine Cu, and $Zn_{1.3}Cu_{98.7}$ gave rise to the highest activity. The H_2 production rate of $Zn_{1.3}Cu_{98.7}$ reached 5472.6 μmol g^{-1} min^{-1} under the irradiation intensity of 788 mW cm^{-2}, which was 3 times higher than pristine Cu at the same reaction condition. Further increasing Zn amount into Cu reduced the catalytic activity of ZnCu alloy catalysts, probably due to the excessive Zn blocking active Cu sites. $Zn_{1.3}Cu_{98.7}$ catalyst demonstrated a much higher activity compared with conventional photocatalytic MSR, and the activity was even superior to the thermocatalytic systems at higher reaction temperature (Table 4.2).[55-62] The solar energy conversion efficiency, which can be defined as the efficiency of solar energy converted to chemical energy in the form of reaction enthalpy, was calculated over $Zn_{1.3}Cu_{98.7}$ and pristine Cu. The conversion efficiency gradually increased with increasing light intensity and amounted to 1.2% over $Zn_{1.3}Cu_{98.7}$ at the intensity of 788 mW cm^{-2}, which was also 3 times higher than pristine Cu (Figure 4.10c). To compare the solar-driven catalytic performance of ZnCu alloy catalysts with noble-metal-based catalysts, which are generally considered as highly efficient catalysts towards MSR, additional pure noble-metal catalysts were fabricated using impregnation method and were applied for solar-driven MSR (Figure 4.10d). $Zn_{1.3}Cu_{98.7}$ catalysts (5472.6 μmol g^{-1} min^{-1}) demonstrated more than 1 order of magnitude higher catalytic activity than Pt/SiO_2 catalysts (501.0 μmol g^{-1} min^{-1}) under the same light irradiation (788 mW cm^{-2}). The production rates of H_2 and CO_2 over Cu and ZnCu catalysts were consistent with the stoichiometry of MSR with a trace amount of undesirable product (such as CO) (Table 4.3). On the contrary, noble-metal-based catalysts exhibited higher selectivity for CO and CH_4 (Table 4.3). These results indicate that Cu NPs exhibit good performance for solar-driven MSR, and the introduction of a small amount of Zn into Cu can substantially accelerate the reaction.

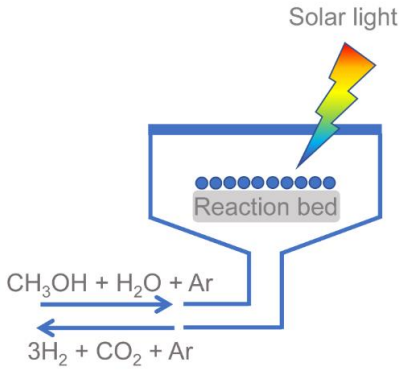

Figure 4.8 Schematic illustration of home-made reactor for solar-driven methanol steam reforming.

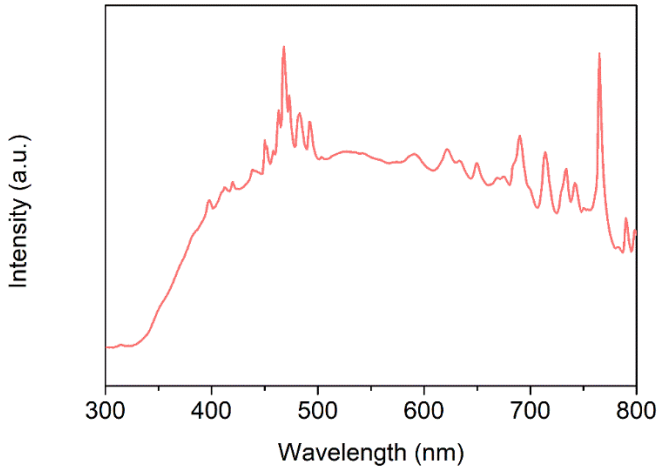

Figure 4.9 Output irradiance of simulated solar light in the solar-driven catalytic reaction.

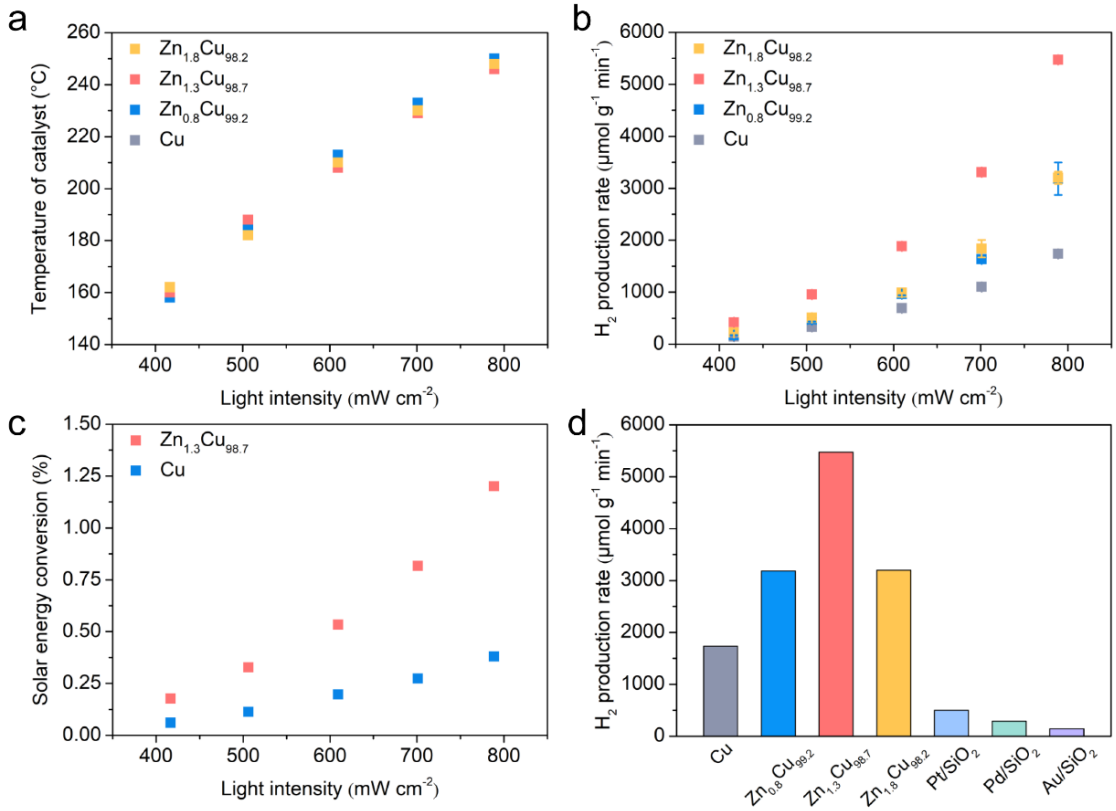

Figure 4.10 Catalytic performance for solar-driven MSR. (a) Dependence of surface temperature of Cu and ZnCu alloy catalysts under the irradiation of full solar spectrum with different light intensity. (b) Solar-driven MSR activity over Cu and ZnCu alloy catalysts under the irradiation of full solar spectrum with different light intensity. (c) Solar energy conversion efficiency over Cu and $Zn_{1.3}Cu_{98.7}$. (d) Solar-driven MSR activity over Cu, ZnCu alloy, and noble-metal-based catalysts at the irradiation intensity of 788 mW cm^{-2}.

Table 4.2 Comparison of the activities over the representative catalytic systems for photocatalytic or thermocatalytic methanol steam reforming

Entry	Materials	Reaction conditions	Mass specific activity (μmol H_2 g^{-1} s^{-1})
1[55]	Pt/TiO_2	UV-Vis light irradiation	5.9
2[56]	$1\%Pt/TiO_2$	350 - 450 nm wavelength light irradiation	5.2
3[57]	$Cu_2O/ZnO/TiO_2$	Simulated solar light with reaction temperature of 210 ℃	21.2
4[58]	NiAl-Au	Reaction temperature of 280 °C	54.3
5[58]	NiAl-Au	Reaction temperature of 340 °C	128.7
6[59]	$Cu/ZnO/Al_2O_3$	Reaction temperature of 200 °C	52.9
7[60]	Cu/ZnO	Reaction temperature of 220 °C	37.0
8[61]	Pd/ZnO	Reaction temperature of 200 °C	8.3
9[62]	$1Pt/3In_2O_3/CeO_2$	Reaction temperature of 325 °C	92.5
This work	$Zn_{1.3}Cu_{98.7}$ alloy	Focused solar light (788 mW cm^{-2})	91.2

Table 4.3. Catalytic performance for methanol steam reforming over Cu, ZnCu alloy, and noble-metal based catalysts under solar-driven or light-promoted thermocatalytic conditions

Samples	Reaction condition	H_2 production rate ($\mu mol\ g^{-1}\ min^{-1}$)	Selectivity (CO) %	Selectivity (CH_4) %
$Zn_{1.3}Cu_{98.7}$	788 mW cm^{-2} (Solar-driven process)	5472.6	1.1	-
Cu	788 mW cm^{-2} (Solar-driven process)	1735.4	0.8	-
Pt/SiO_2	788 mW cm^{-2} (Solar-driven process)	501.0	1.6	2.2
Pd/SiO_2	788 mW cm^{-2} (Solar-driven process)	289.9	63	0.9
Au/SiO_2	788 mW cm^{-2} (Solar-driven process)	144.0	-	3.4
Cu	220 °C with visible light irradiation	1222.9	0.7	-
Cu	220 °C	500.0	0.8	-
$Zn_{0.8}Cu_{99.2}$	220 °C with visible light irradiation	2328.8	0.8	-

$Zn_{1.3}Cu_{98.7}$	220 °C with visible light irradiation	2871.1	1.1	-
$Zn_{1.3}Cu_{98.7}$	220 °C	862.4	0.7	-
$Zn_{1.8}Cu_{98.2}$	220 °C with visible light irradiation	2431.5	0.9	-
$Zn_{2.3}Cu_{97.7}$	220 °C with visible light irradiation	1639.4	0.9	-

4.3.3 The role of light energy towards MSR

In the plasmonic photocatalytic process, in addition to photo-induced heating, photo-induced hot carriers can also participate in the surface chemical reactions by activating adsorbates. To verify the contributions of hot carriers, photo-assisted thermocatalytic MSR reaction was conducted in a home-made flow reactor equipped with a quartz mirror under atmospheric pressure (Figure 4.11). Visible light ($420 < \lambda < 800$ nm) with a maximum light intensity of 624.7 mW cm^{-1} was used (Figure 4.12). The influence of ultraviolet and infrared light was ruled out by the light filters (L42 and HA30), and photo-induced heat was mitigated by the temperature controller (Figure 4.13 and 4.14).

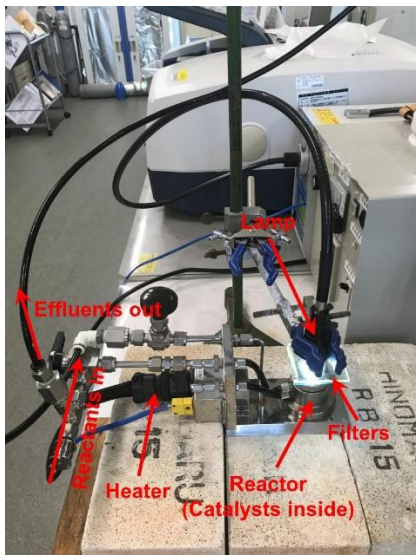

Figure 4.11 Photograph of home-made photo-assisted thermal reactor.

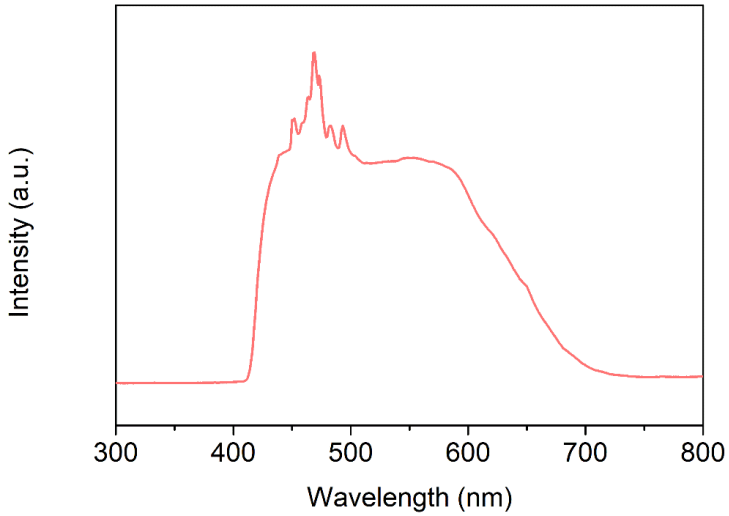

Figure 4.12 Output irradiance of the visible light in the photo-assisted thermal catalytic reaction.

Figure 4.13. Detected temperature of catalysts without light irradiation in the thermocatalytic process.

Figure 4.14 Detected temperature of catalysts with light irradiation in the photo-assisted thermocatalytic process.

Figure 4.15 demonstrated the reaction rates of H_2 production over catalysts at 220 °C with and without visible light irradiation. In dark, the optimized $Zn_{1.3}Cu_{98.7}$ demonstrated a higher H_2 production rate of 862 μmol g^{-1} min^{-1} compared with pristine Cu and Cu/ZnO with same amount of Zn and Cu. Under visible light irradiation, the reaction rate of $Zn_{1.3}Cu_{98.7}$ was increased to 2871 μmol g^{-1} min^{-1} (Figure 4.15). Figure 4.16 showed the H_2 production rates of $Zn_{1.3}Cu_{98.7}$ were consistently much higher than that of pristine Cu at the reaction temperature from 180 °C to 220 °C, and the reaction rates over Cu and $Zn_{1.3}Cu_{98.7}$ catalysts with light irradiation were higher than that of without light irradiation. The activity enhancement (calculated by the reaction rate at light condition divided by the rate at dark condition) over $Zn_{1.3}Cu_{98.7}$ declined from 9.2 to 3.3 times with increasing reaction temperature from 180 to 220 ºC (Figure 4.17), while, in contrast, the rate difference increased with the rise in temperature (Figure 4.18). Steady-state reaction H_2 production rate at a temperature of 200 °C revealed that the photo-enhanced activity over $Zn_{1.3}Cu_{98.7}$ catalysts was light-sensitive and reversible (Figure 4.19). Furthermore, the $Zn_{1.3}Cu_{98.7}$ catalysts displayed good stability in both dark and light conditions, and the catalytic activity remained stable in 4-h reaction (Figure 4.20). The visible light irradiation could lead to an obvious activity enhancement. I suppose that the observed photo-enhancement mainly resulted from the hot carrier-induced reactants activation.

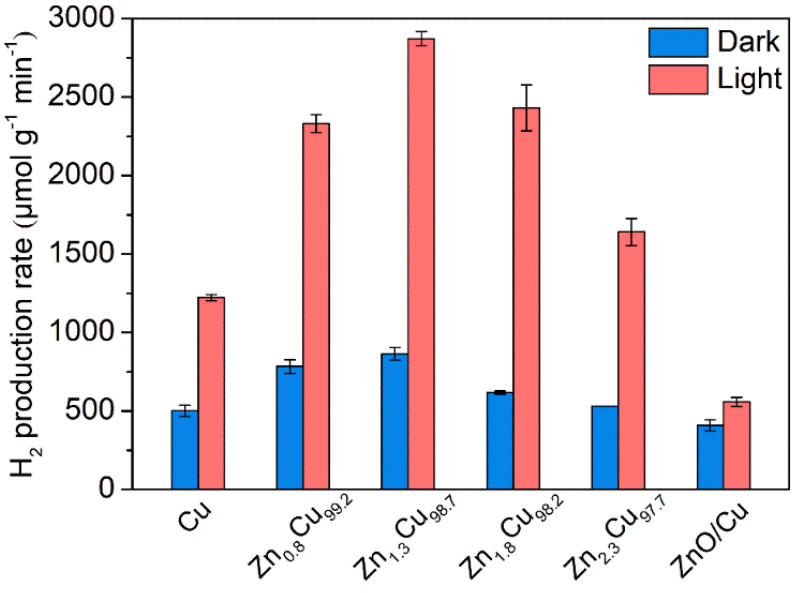

Figure 4.15 MSR activity at 220 °C with and without visible light irradiation over different catalysts.

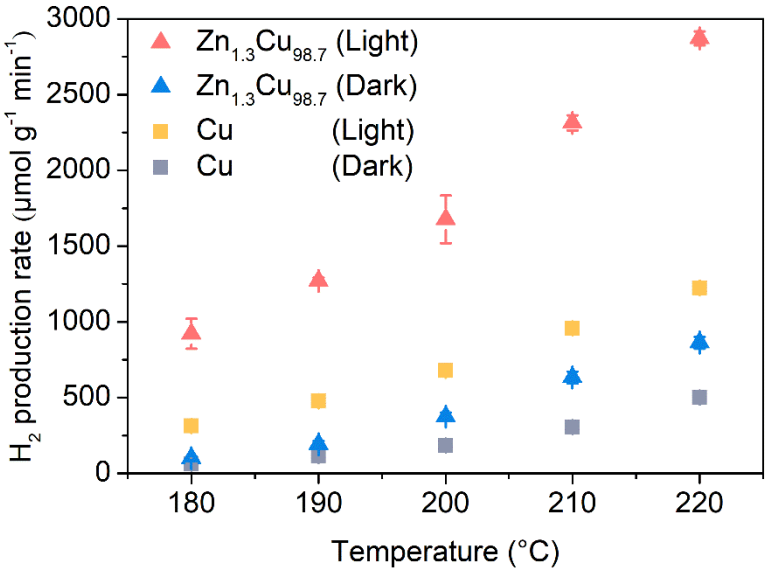

Figure 4.16 Reaction rate of Cu and $Zn_{1.3}Cu_{98.7}$ alloy catalysts as a function of temperature under the purely thermal condition (dark) and under photo-assisted thermal condition (light).

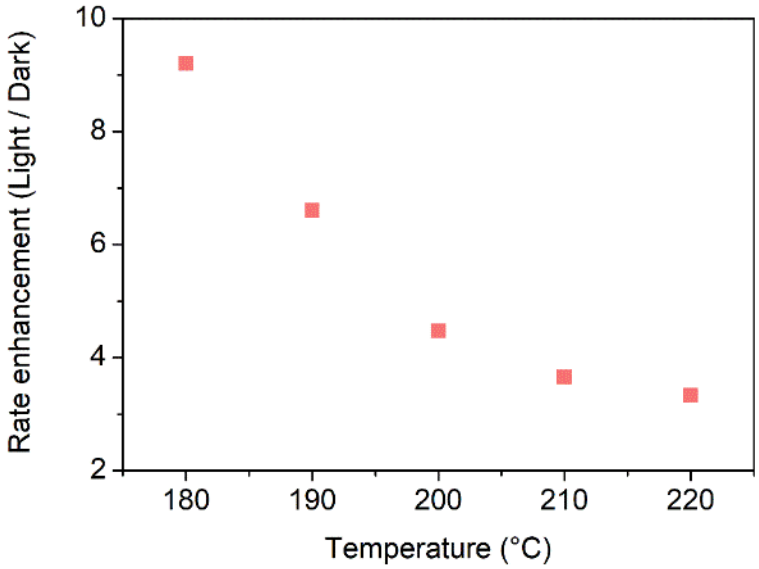

Figure 4.17 Rate enhancement (H_2 production rate with light irradiation divided by the rate in dark condition) as a function of reaction temperatures over $Zn_{1.3}Cu_{98.7}$ alloy.

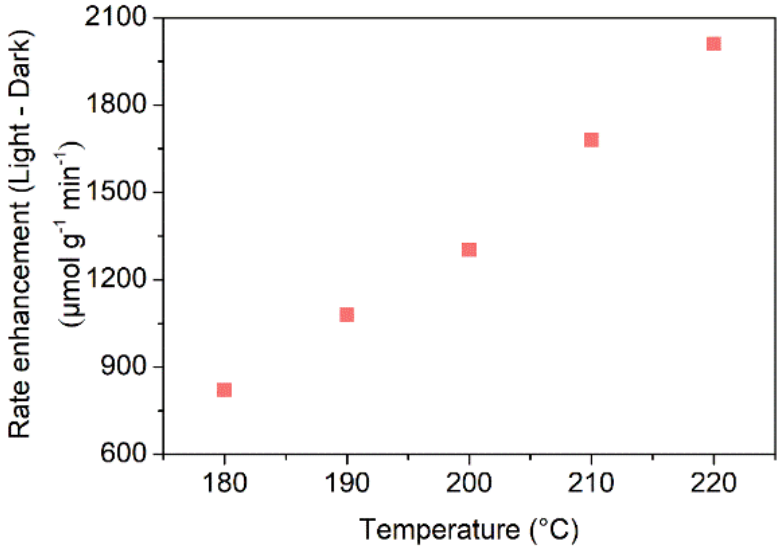

Figure 4.18 Difference in H_2 production rate between dark and light conditions as a function of reaction temperatures over $Zn_{1.3}Cu_{98.7}$ alloy.

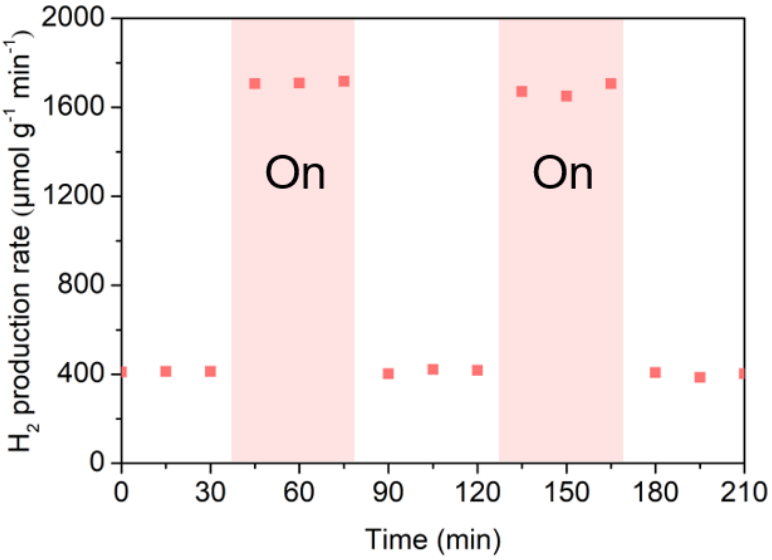

Figure 4.19 MSR activity over $Zn_{1.3}Cu_{98.7}$ alloy catalysts with and without visible light irradiation at 200 °C.

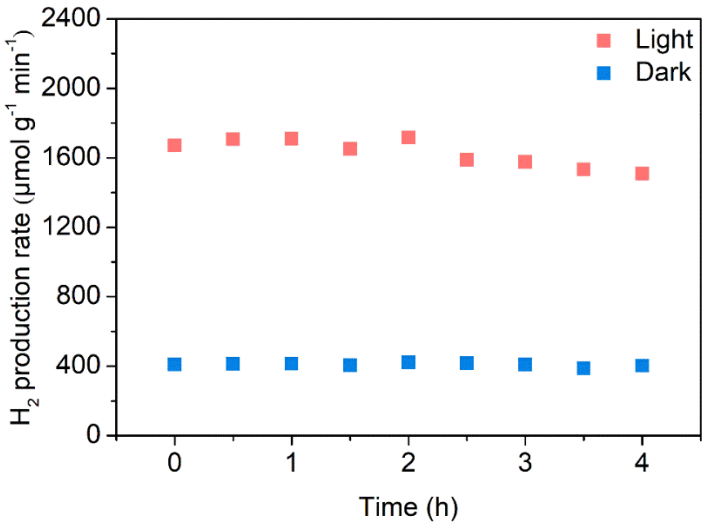

Figure 4.20 Stability test of $Zn_{1.3}Cu_{98.7}$ alloy under dark and light conditions at reaction temperature of 200 °C.

To verify this assumption, we performed a series of fundamental studies. The finite difference time domain (FDTD) simulations showed an intense electric field on both Cu and $Zn_{1.3}Cu_{98.7}$ NPs under light irradiation at 570 nm (the LSPR peak of Cu) (Figure 4.21). The amplified electric field triggered the excitation of hot carriers capable of enhancing the catalytic reactions by activating certain chemical bonds of adsorbates.[63] No significant difference in the electric field was observed between Cu and $Zn_{1.3}Cu_{98.7}$, confirming that adding a small amount of Zn did not alter the LSPR property of Cu NPs, in accordance with UV-Vis DRS results.

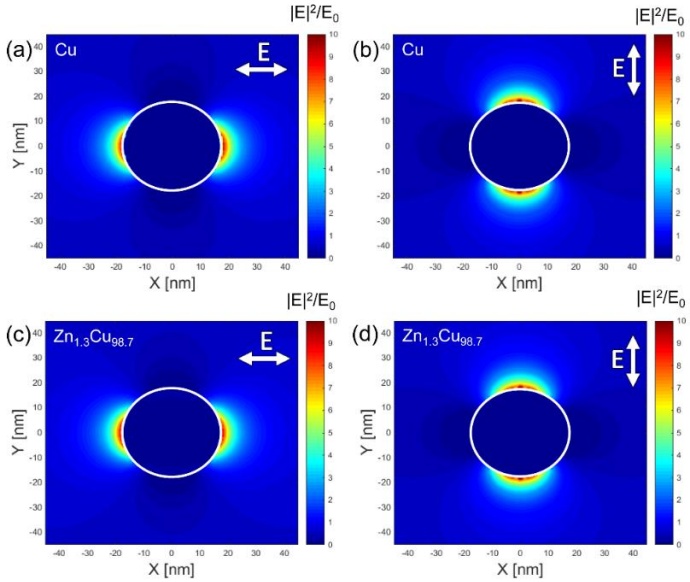

Figure 4.21 Electrical field enhancement of Cu (a-b) and $Zn_{1.3}Cu_{98.7}$ (c-d) at 570 nm.

The H_2 production rate of $Zn_{1.3}Cu_{98.7}$ showed a linear dependence on light intensity (Figure 4.22), validating that the reaction was facilitated by the photo-induced hot carriers.[24] With the assistance of these photo-induced hot carriers, the apparent activation energy over $Zn_{1.3}Cu_{98.7}$ catalyst dropped from 102.7 ± 2.5 kJ mol^{-1} to 53.6 ± 3.6 kJ mol^{-1} (Figure 4.23), leading to a ~50% decrease. The significant decrease in activation energy demonstrated that photo-induced hot carriers can facilitate the activation of methanol and/or water in MRS, thus enhancing catalytic activity.

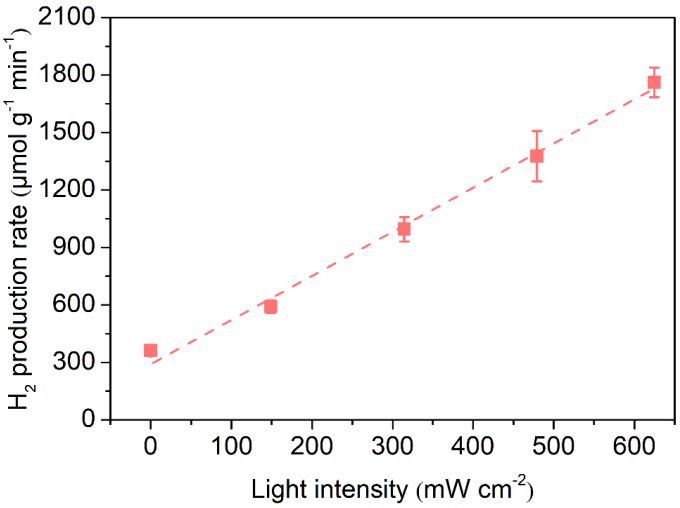

Figure 4.22 Dependence of reaction rate of $Zn_{1.3}Cu_{98.7}$ on light intensity at reaction temperature of 200 °C.

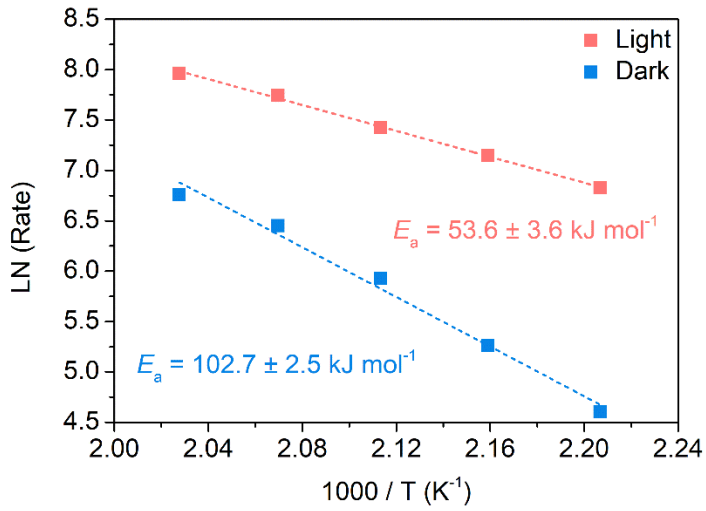

Figure 4.23 Arrhenius plots for H_2 production rate under dark and light conditions over $Zn_{1.3}Cu_{98.7}$ catalysts.

I further calculated the apparent quantum efficiency (AQE) of $Zn_{1.3}Cu_{98.7}$ under different monochromatic light irradiation (Figure 4.24). The tendency of AQE showed a

similar trend to the light absorption spectra of $Zn_{1.3}Cu_{98.7}$, indicating that the excitation of hot carrier contributed to the observed activity enhancement (Figure 4.25).

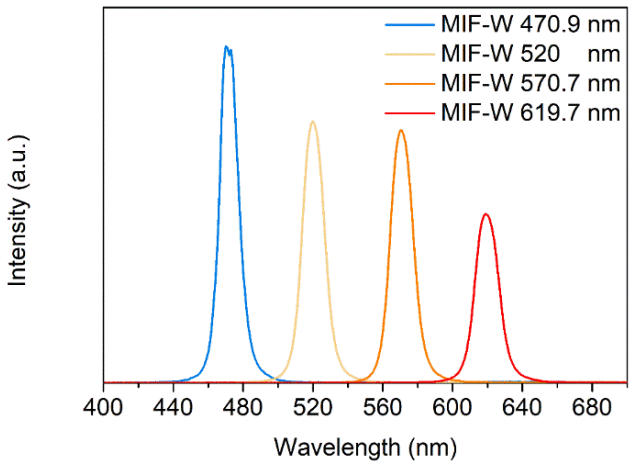

Figure 4.24 Output irradiance of different wavelengths in the photo-assisted thermal catalytic reaction.

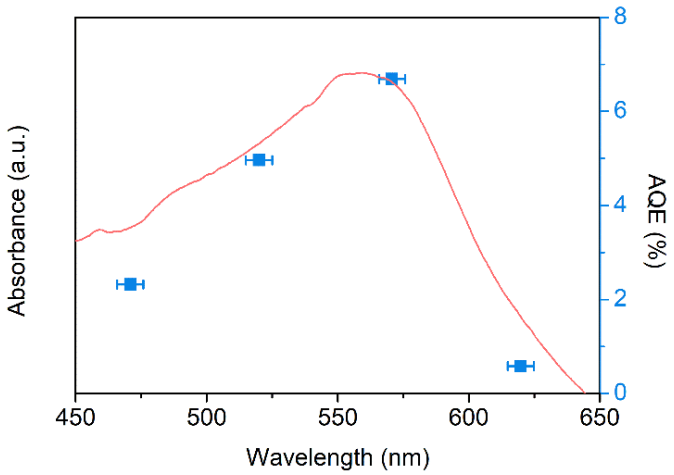

Figure 4.25 Light absorption spectrum and apparent quantum efficiency values of $Zn_{1.3}Cu_{98.7}$ at 200 °C with light irradiation in different wavelengths.

In-situ diffuse reflectance infrared Fourier transform spectra (DRIFTS) were conducted to investigate the reaction intermediates in MSR over $Zn_{1.3}Cu_{98.7}$ under dark and light conditions at 180 °C. The spectra over time before and after light irradiation were shown in Figure 4.26. The peaks at around 2360 cm^{-1} can be assigned to the characteristic rotation-vibration of gaseous CO_2. Under dark condition, the intensity of these peaks increased over time (Figure 4.26). After introducing light into the reaction system, the peak intensity of CO_2 grew faster than that in the dark, as shown from the slope change in Figure 4.27, which was in consistent with the result of photo-induced

activity enhancement. Previous studies suggested that the key intermediates formed over Cu-based catalysts in MSR are CH_2O and HCOOH (Figure 4.28a)[64-66] or $HCOOCH_3$ (Figure 4.28b),[66, 67] while several studies suggested the formation of CO followed by the conversion of CO to CO_2 through the water-gas-shift reaction.[11, 68] In this work, no peaks from gaseous or absorbed CO located between 2100 and 2000 cm^{-1} were observed at 180 °C with and without light irradiation,[69] suggesting that the reaction mainly proceed through the former pathway. Under the light illumination, two peaks at around 1720 and 1410 cm^{-1} were observed (Figure 4.26), which can be assigned to the vibration bands of υ(CO) and δ(CH) in the adsorbed CH_2O intermediate, respectively.[70, 71] Another relatively weak peak related to the vibration bands of υ(COO) in the adsorbed HCOOH intermediate appeared at around 1560 cm^{-1} (Figure 4.26). The upward peaks below 2000 cm^{-1} suggested that the amount of produced CH_2O and HCOOH increased after introducing light. In contrast, the amount of the adsorbed CH_3O species decreased, which can be evidenced from the downward peaks at around 2950 cm^{-1}.[70, 71] The gradually ascending amount of the key intermediates (CH_2O and HCOOH) after light irradiation indicated that a much easier conversion of CH_3O to CH_2O and HCOOH can be achieved with the assistance of hot carriers (Figure 4.27), leading to a dramatic activity enhancement. In order to further elucidate the unique contribution of photo-induced hot carriers, the DRIFT spectra in elevated reaction temperature (from 180 to 220 °C) without light irradiation were recorded. As shown in Figure 4.29, a weak peak at around 2100 cm^{-1} assigned to CO appeared upward when increasing temperature. Such a signal was absent when applying the light illumination at 180 °C, implying the potential of hot carriers for modulating the reaction pathway to increase the activity.

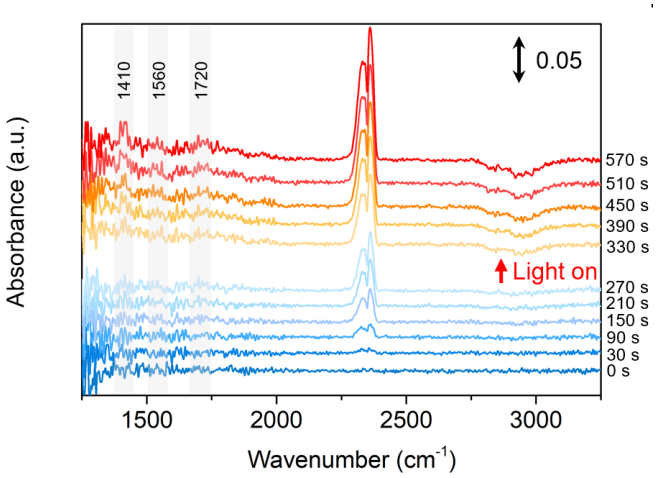

Figure 4.26 *In-situ* DRIFT spectra of $Zn_{1.3}Cu_{98.7}$ under dark and light conditions at 180 °C.

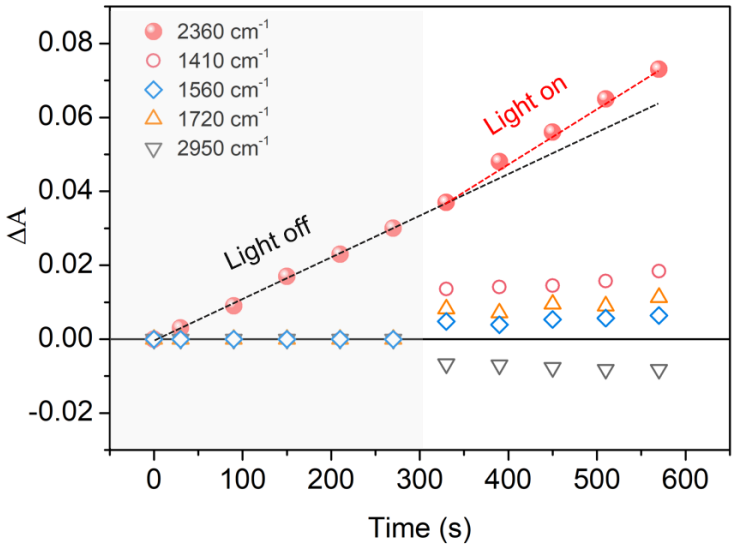

Figure 4.27 Slope change of the peak intensity of key intermediates derived from *in-situ* DRIFT spectra in Figure 4.26.

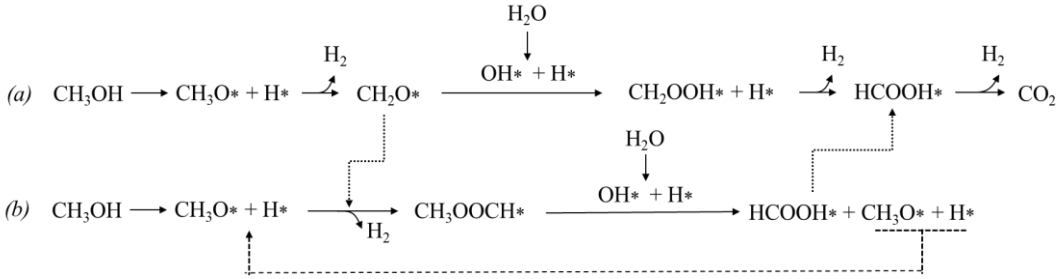

Figure 4.28 Main reaction pathways for methanol steam reforming over Cu-based catalysts.

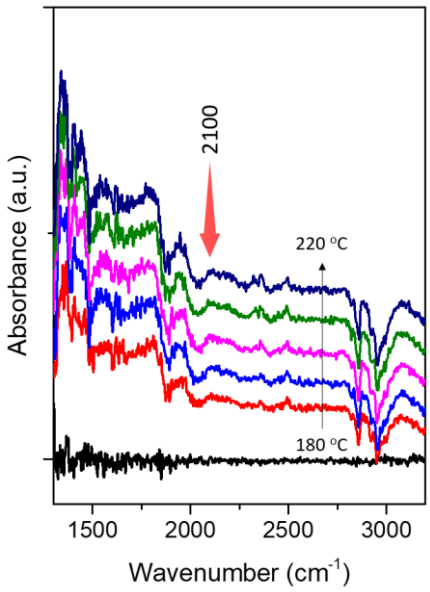

Figure 4.29 *In-situ* DRIFT spectra of $Zn_{1.3}Cu_{98.7}$ under dark condition at elevated reaction temperatures.

To investigate the effect of Zn in ZnCu alloy on the possible reaction pathways, we performed density functional theory (DFT) calculations to acquire Gibbs free energy diagrams. Figure 4.30 showed the energy barrier of each elementary step for MSR on the pristine Cu (111) and Zn-Cu (111) surfaces. Based on the previous studies, specifically, the CH_3OH was initially dehydrogenated into CH_3O*, followed by decomposition into CH_2O* through C-H bond activation, and subsequently converted into CH_2OOH* through the interaction between CH_2O* and OH* which was produced from the water dissociation.[65] Whereafter, the CH_2OOH* was transformed into HCOOH*, and finally dehydrogenated into CO_2 and H_2. The detailed calculation results revealed that the dehydrogenation of methoxy species (CH_3O* → CH_2O* + H*) and water dissociation (H_2O* → OH* + H*) were thermodynamically unfavorable with much positive high Gibbs free energy, and hence were considered as the rate-determining steps, demonstrating that both methanol and water activation are pivotal in MSR. Interestingly, the free energy of methoxy dehydrogenation on Zn-Cu (111) alloy was similar to that of pristine Cu (111) (1.64 vs 1.56 eV), while Zn-Cu (111) alloy have a much lower water dissociation energy than the pristine Cu (0.36 vs 0.91 eV), indicating that the methanol dehydrogenation process was primarily dominated by Cu, meanwhile Zn as the catalytic sites could greatly promote water activation and dissociation. With the assistance of Zn, abundant surface hydroxyls can be produced through water dissociation, further facilitating the conversion of key intermediates to products, and therefore promoting the MSR at the interface between Zn and Cu.

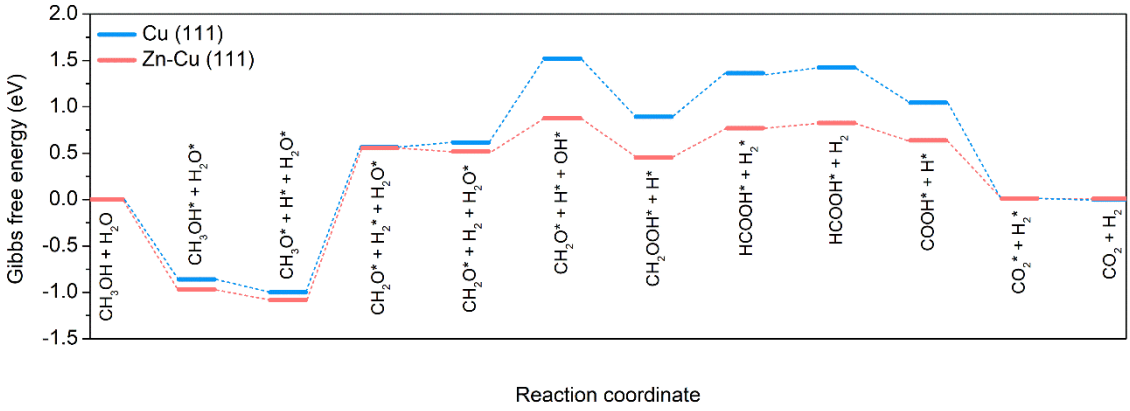

Figure 4.30 Energy profiles for MSR over Cu (111) and Zn atoms substituted Cu (111) surfaces.

To further verify the contribution of the Zn for activating water molecules, kinetic isotope effect (KIE) measurements were carried out by measuring the reaction rates of Cu and $Zn_{1.3}Cu_{98.7}$ with CH_3OH/H_2O and CH_3OH/D_2O (Figure 4.31). For a given methyl isotopic identity (CH_3), the reaction rate with H_2O was 1.47 times higher than that with D_2O over Cu catalysts, in good agreement with the previous work on thermocatalytic MSR over Cu-based catalysts.[72 73] In contrast, the KIE value was 1.36 over $Zn_{1.3}Cu_{98.7}$ under the identical reaction condition, which was lower than that of pristine Cu. The lower KIE value detected on $Zn_{1.3}Cu_{98.7}$ strongly indicated that the introduction of Zn in Cu can lead to a better O-H bond activation for water dissociation, consistent with the DFT results. Furthermore, KIE measurements can be employed to distinguish the hot carrier-mediated surface reactions from phonon-driven reactions, since hot carrier-driven reactions demonstrate higher KIE than the thermal-driven reactions.[74-76] A larger KIE of 1.54 was obtained under light condition over $Zn_{1.3}Cu_{98.7}$, indicating that the hot carrier generated from $Zn_{1.3}Cu_{98.7}$ can facilitate MSR reaction by promoting the water dissociation. KIE results, in accordance with experimental results, demonstrated that the surface-deposited Zn atoms could serve as active sites for water dissociation; and even more crucially, Zn could act as charge transfer channels for trapping the hot electron from Cu, delivering the hot electrons to water molecules and further powering the water activation.

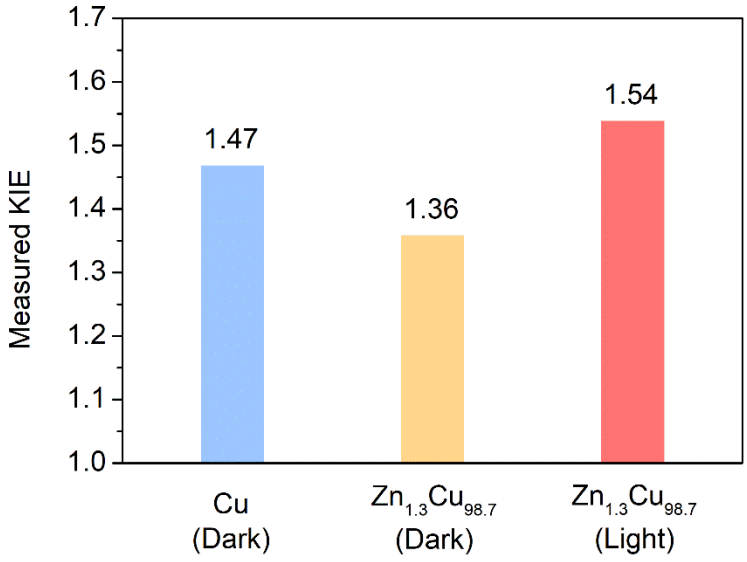

Figure 4.31 Kinetic isotope effect (KIE) ($CH_3OH + H_2O$ rate / $CH_3OH + D_2O$ rate) over Cu and $Zn_{1.3}Cu_{98.7}$ at 180 °C.

To further validate the charge transfer process between the Zn-Cu interface and the surface adsorbates, DFT-based first-principles molecular dynamic simulation and electronic structure calculation were performed. The following three kinds of reactants were prepared in the open space provided on the slab surface. [Case A] Mixed gas of 4 CH_3OH and 4 H_2O (of initial input molecules), 1 H_2 and 1 CO_2 (of final products), [Case B] Mixed gas of 4 CH_3OH, 2 H_2O, 1 H_2, 1 CO_2 in the space, and Zn-OH, Cu-H, Cu-OH, and Zn-H adsorbates on the slab surface at initial stage of simulation, [Case C] Only 10 H_2O molecules in the space above the slab surface.

[Case A: 4 CH_3OH, 4 H_2O, 1 H_2, and 1 CO_2 are prepared at initial stage of simulation.]

Investigating the dynamical properties of reactant molecules at around 220 °C in our limited duration time of simulation (i.e. 7.2 picoseconds), we noticed that one of the methanol molecules was adsorbed at Cu site and the molecule was spontaneously dissociated (Figure 4.32). The -OH part did not detach from the surface, but it was drifting on the surface. On the other hand, the -CH_3 part detached from the surface soon after the dissociation and it wafted in the space and then adsorbed at a Cu site of the other side of the slab surface. The -CH_3 crawled along the surface but it did not detach itself from the surface once it was adsorbed in the duration time of our simulation with keeping the -Cu-C(-H_3) atomic distance roughly between 1.7 and 2.7 angstroms. The other molecules did not indicate stable adsorption properties and only indicated simple collision properties. The shortest collision atomic distances of -Cu-O between slab surface and water molecules and of -Cu-C between the surface and CO_2 molecules and of -Cu-H between the surface and the hydrogen molecule were roughly 2.1, 3.0, and 1.9 angstroms, respectively. Since the top surface in our simulation model included 36 atoms in total and only one of them was Zn atom, the phenomena of adsorptions or collisions of the molecules at the Zn site were observed rarely. The examples of atomic approaches were 1.9 angstroms of -Zn-H(-CH_2) and 2.4 angstroms of -Zn-C(-H_3) at around the moment of the contact between Zn site and the crawling -CH_3. Those atomic distances were still larger than those of -Cu-H(CH_2), 1.5 angstroms and -Cu-C(H_3), 1.9 angstroms at the moment of molecule dissociation of methanol in Figure 4.32.

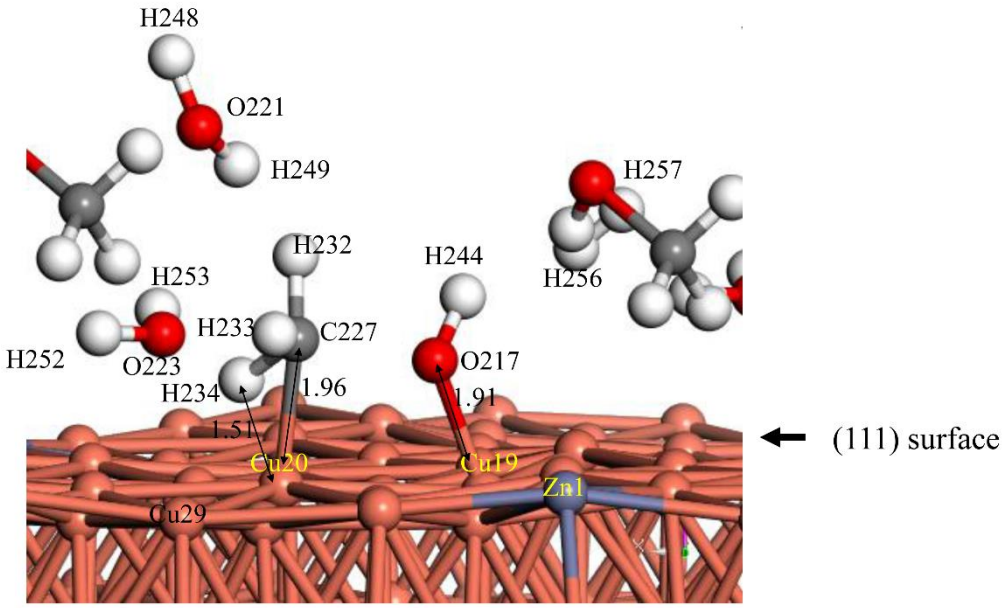

Figure 4.32 The moment when the one methanol molecule was spontaneously dissociated at 220 °C on the (111) Cu surface. The unit of atomic distance is angstrom. Color code: Brown Cu, Cyan Zn, Gray C, Red O, White H.

Profiles (a) ~ (k) were weight profiles of atomic orbital wavefunction components obtained by projecting the eigen-wave-function onto the corresponding atomic orbitals (Figure 4.33). The red broken line in each profile located at -4.2 eV indicated the highest occupied level (HOL). The dominant components of the unoccupied band were Cu 4p and Cu 4s, and the Cu 4s component was the strongest in the almost all energy range of the unoccupied states. It was noteworthy that Cu 4s profile indicated a valley structure in the energy range from -0.2 to -1.8 eV and this valley part of Cu 4s component was well compensated by the Zn 4p component which was mainly derived from the surficial Zn atoms and this unoccupied Zn 4p orbital component was well-matched with the main part of the unoccupied H 1s orbital component located from -1.4 to -0.4 eV (indicated in red circles in (c), (f), (k) of Figure 4.33). The effect of Zn substitution on electronic structure was significant since the Zn 4p component per one Zn atom at around -1 eV was at least as ten times as large as the Cu 4s component per one Cu atom although the atomic concentration of Zn is only 1.4 atomic % in the slab. What is interesting furthermore is that although it appeared that the main components at around the HOL, which marked by orange narrow band in (a) ~ (f) in Figure 4.33, were Cu 3d and Cu 4s by the profiles (a) and (c) of Figure 4.33, actually the main component at around the surficial Zn was Zn 4s

component of the Zn instead of neighbor surficial Cu components in the local electronic structure (see Figure 4.34 (a) ~ (i), especially the parts marked by circles in (d) and (h)).

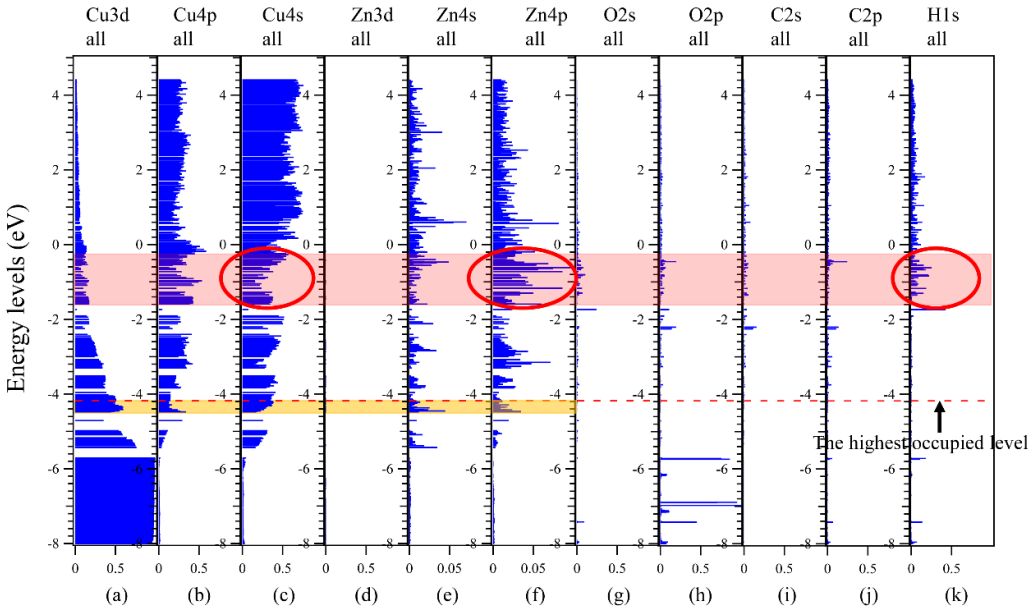

Figure 4.33. The global electronic properties of the whole system at the moment when the one methanol molecule was dissociated. The highest occupied level (HOL) is indicated in a red broken line.

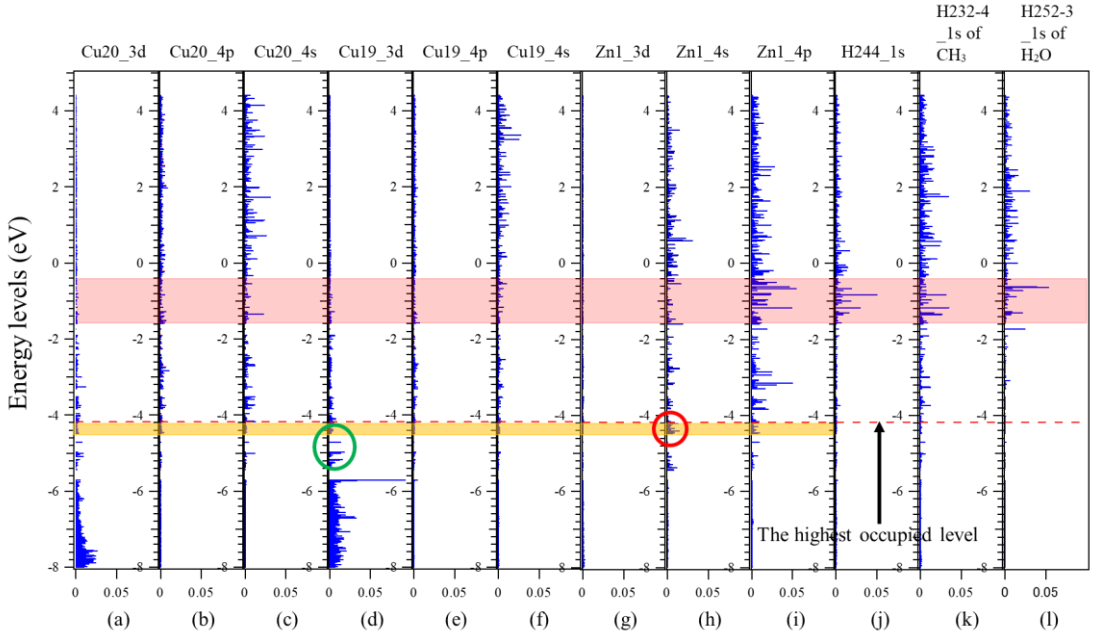

Figure 4.34 The detailed local electronic properties related to the adsorbates in Figure 4.32. The red broken line indicates HOL.

[Case B: 4 CH_3OH, 2 H_2O, 1 H_2, 1 CO_2, and -Zn-OH, -Cu-H, -Cu-OH, -Zn-H adsorbates are prepared at initial stage of simulation.]

Since the adsorbates including surficial Zn atom did not appear during the limited term of simulation Case A, the Case B which included -Zn-OH, -Cu-H, -Cu-OH, and -Zn-H adsorbates at initial stage of molecular dynamics simulation was investigated aiming to obtain the moments showing -Zn-OH and -Zn-H structures on the slab surface as thermally equilibrated condition at 220 ℃. The obtained -Zn-OH and -Zn-H structures equilibrated at 220 ℃ are shown in Figure 4.35 (a) and (b), respectively, and the electronic properties for the cases are shown in Figure 4.36 (a) and (b), respectively. In the case that -Zn-O-H structure was formed on the surface, it is confirmed that the unoccupied Zn 4p components was hybridized with O 2p of -Zn-O-H adsorbate. The energy range (-0.8 ~ -1.6 eV) which included strong unoccupied components of the water molecule in the vicinity of the surficial Zn was also well overlapped with the energy range where the strong unoccupied component of Zn 4p located. Interestingly, the electron density of the Cu atom in the vicinity of the Zn at around the HOL was much smaller than the surficial Zn (see the components, Cu200_3d, Cu195_3d, and Zn3_4s in Figure 4.36 (a)). It implies that the photo-excitation can be concentrated at the surficial Zn site. On the other hand, the hybridization between Zn 4p and H 1s unoccupied components at the energy range (-0.2 ~ -1.6 eV), where the strong unoccupied component of Zn 4p situated, looks not so strong in the case that -Zn-H was formed on the surface, in spite of the fact that the Zn-H atomic distance is small (Figure 4.36 (b)).

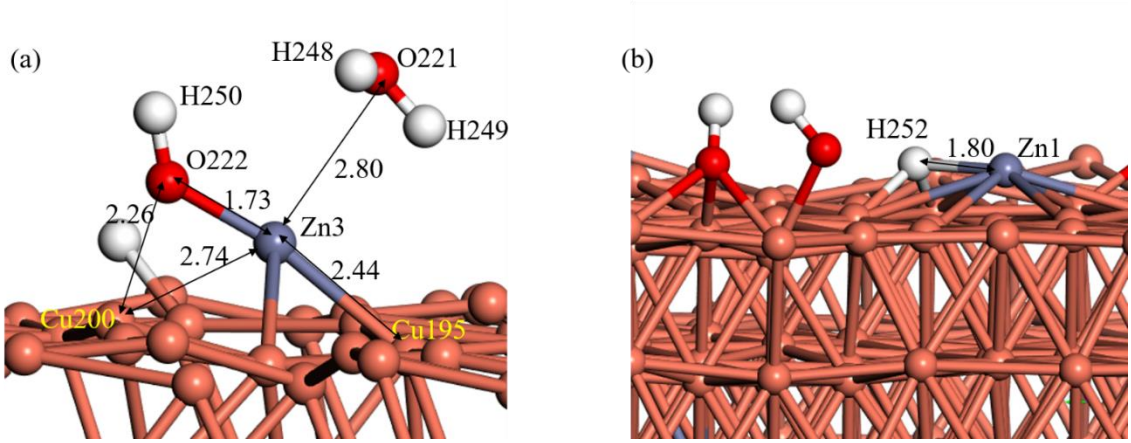

Figure 4.35 (a) A geometry at the moment when the -Zn-O-H structure was formed. (b) A geometry at the moment when the -Zn-H structure was formed.

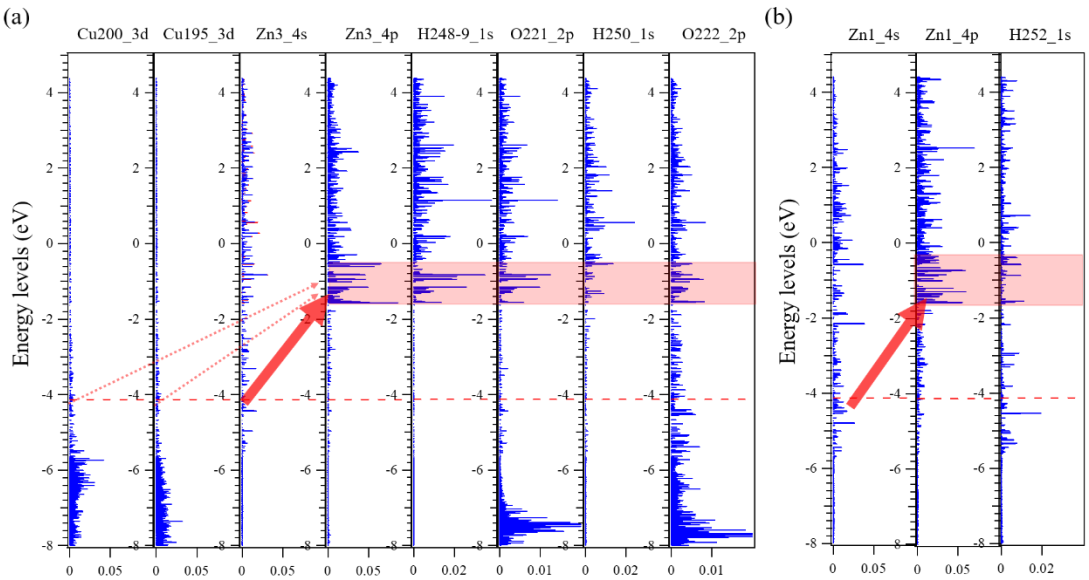

Figure 4.36 The electronic properties (a) at the moment when the -Zn-O-H structure was formed (Figure 4.35 (a)) and (b) at the moment when the -Zn-H structure was formed (Figure 4.35 (b)). The red broken lines indicate HOL.

[Case C: 10 H_2O are prepared at initial stage of simulation.]

To investigate the water molecule adsorption properties at the Zn site in limited computational cost, a simulation model that contains only ten water molecules without other kinds of molecules above the ZnCu alloy slab surface was prepared. No water molecule spontaneous dissociative adsorption can be observed, but the moment when one water molecule collided with the surficial Zn site was detected. The geometry at moment is indicated in Figure 4.37 (a), and the electronic properties at the moment is shown in Figure 4.37 (b). It is confirmed that the unoccupied H 1s component of adsorbed water molecule was well hybridized with the unoccupied component of the 4p orbital of the surficial Zn atom. The 4s component of the surficial Zn at HOL was larger than that of Cu atoms neighbor to the Zn on the surface.

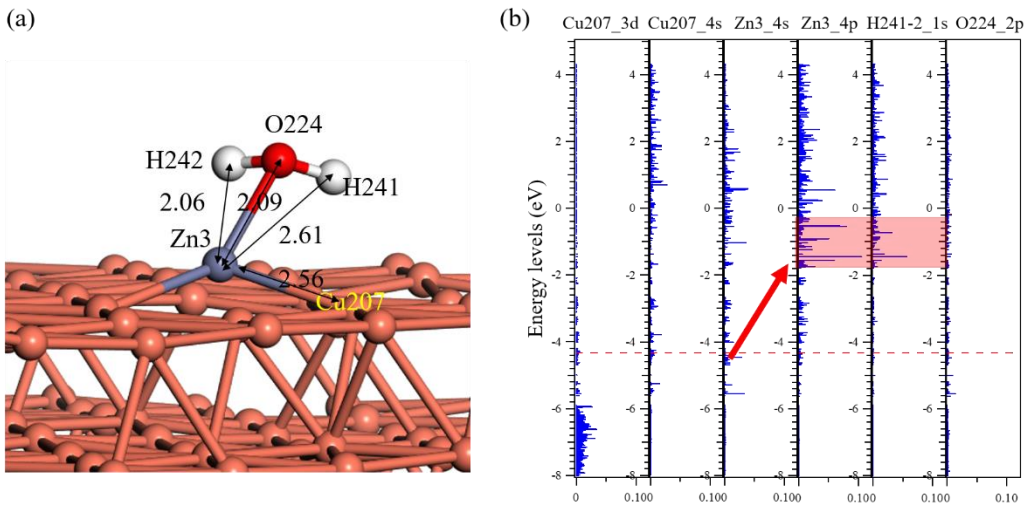

Figure 4.37 (a) A geometry at the moment when the H_2O molecule came close to the surficial Zn site. (b) The electronic properties at the moment (a). The red broken line indicates HOL.

Based on the above results and discussion, I proposed a plausible reaction mechanism for solar-driven MSR over ZnCu alloy. As shown in Figure 4.38, under light irradiation, photo-induced hot electrons can be excited from Cu, and be pumped into water molecules through the electron transfer channel of Zn atoms, expediting the water dissociation to produce more surface adsorbed hydroxyls for a much easier conversion of reaction intermediates. Such a hot electron migration process favored the separation of hot carriers, consequently resulting in electron-deficient Cu for further facilitating the methanol oxidation. This unique hot electron migration process, together with photothermal heating, endows the interface of ZnCu alloy with outstanding capacity for activating both the water and methanol molecules, concertedly enabling an efficient solar-driven MSR.

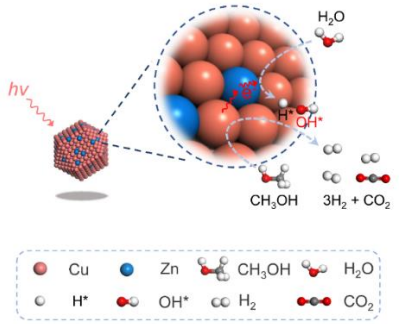

Figure 4.38 Proposed mechanism for the hot electron-mediated methanol steam reforming reaction over plasmonic ZnCu alloy.

4.4 Conclusion

In summary, a solar-driven methanol steam reforming process is developed over Zn-Cu alloy plasmonic catalysts that comprise homogeneously dispersed Zn atoms on the surface of Cu. Through the excitation of LSPR of Cu under solar light irradiation, both the hot carriers and photothermal heating are generated and contributed to the surface reaction, resulting in highly efficient solar-driven MSR. Under concentrated simulated sunlight irradiation (788 mW cm^{-2}) without additional thermal energy input, a H_2 production rate of 328 mmol $g_{catalyst}^{-1}$ h^{-1} (5472 μmol $g_{catalyst}^{-1}$ min^{-1}) and a solar energy conversion efficiency of 1.2% are achieved over $Zn_{1.3}Cu_{98.7}$ plasmonic catalyst. Both the experimental and theoretical investigations indicate that introducing Zn atoms can lower the activation energy of water dissociation, and can trap the hot electrons from Cu and deliver them to water molecules, further promoting the water activation and retarding the back-flow of hot electrons. Such a charge migration process suppresses the non-effective carrier recombination, and subsequently induces electron-deficient Cu for methanol oxidation. The interface formed between Zn and Cu in ZnCu alloy favors the hot carrier transfer to activate both the water and methanol molecules, which accounts for the hot carrier-mediated catalytic performance. This new catalytic process paves a potential way towards a commercially viable and sustainable H_2 production strategy.

References

1. M. Z. Jacobson, W. Colella and D. Golden, *Science*, 2005, **308**, 1901-1905.

2. O. Z. Sharaf and M. F. Orhan, *Renewable Sustainable Energy Rev.*, 2014, **32**, 810-853.

3. R. L. Cohen and J. Wernick, *Science*, 1981, **214**, 1081-1087.

4. P. Preuster, C. Papp and P. Wasserscheid, *Acc. Chem. Res.*, 2017, **50**, 74-85.

5. L.-N. Chen, K.-P. Hou, Y.-S. Liu, Z.-Y. Qi, Q. Zheng, Y.-H. Lu, J.-Y. Chen, J.-L. Chen, C.-W. Pao, S.-B. Wang, Y.-B. Li, S.-H. Xie, F.-D. Liu, D. Prendergast, L. E. Klebanoff, V. Stavila, M. D. Allendorf, J. Guo, L.-S. Zheng, J. Su and G. A. Somorjai, *J. Am. Chem. Soc.*, 2019, **141**, 17995-17999.

6. D. R. Palo, R. A. Dagle and J. D. Holladay, *Chem. Rev.*, 2007, **107**, 3992-4021.

7. S. Sá, H. Silva, L. Brandão, J. M. Sousa and A. Mendes, *Appl. Catal., B*, 2010, **99**, 43-57.

8. M. Friedrich, S. Penner, M. Heggen and M. Armbrüster, *Angew. Chem. Int. Ed.*, 2013, **52**, 4389-4392.

9. C. Rameshan, W. Stadlmayr, S. Penner, H. Lorenz, N. Memmel, M. Hävecker, R. Blume, D. Teschner, T. Rocha, D. Zemlyanov, A. Knop-Gericke, R. Schlögl and B. Klötzer, *Angew. Chem. Int. Ed.*, 2012, **51**, 3002-3006.

10. C. Rameshan, W. Stadlmayr, C. Weilach, S. Penner, H. Lorenz, M. Hävecker, R. Blume, T. Rocha, D. Teschner, A. Knop-Gericke, R. Schlögl, N. Memmel, D. Zemlyanov, G. Rupprechter and B. Klötzer, *Angew. Chem. Int. Ed.*, 2010, **49**, 3224-3227.

11. L. Lin, W. Zhou, R. Gao, S. Yao, X. Zhang, W. Xu, S. Zheng, Z. Jiang, Q. Yu, Y.-W. Li, C. Shi, X.-D. Wen and D. Ma, *Nature*, 2017, **544**, 80-83.

12. L. Lin, Q. Yu, M. Peng, A. Li, S. Yao, S. Tian, X. Liu, A. Li, Z. Jiang, R. Gao, X. Han, Y.-w. Li, X.-d. Wen, W. Zhou and D. Ma, *J. Am. Chem. Soc.*, 2021, **143**, 309-317.

13. Y. Zhao, W. Gao, S. Li, G. R. Williams, A. H. Mahadi and D. Ma, *Joule*, 2019, **3**, 920-937.

14. Z.-j. Wang, H. Song, H. Liu and J. Ye, *Angew. Chem. Int. Ed.*, 2020, **59**, 8016-8035.

15. G. Chen, G. I. N. Waterhouse, R. Shi, J. Zhao, Z. Li, L.-Z. Wu, C.-H. Tung and T. Zhang, *Angew. Chem. Int. Ed.*, 2019, **58**, 17528-17551.

16. H. Song, X. Meng, Z.-j. Wang, H. Liu and J. Ye, *Joule*, 2019, **3**, 1606-1636.

17. A. Kudo and Y. Miseki, *Chem. Soc. Rev.*, 2009, **38**, 253-278.

18. T. Hisatomi and K. Domen, *Nature Catalysis*, 2019, **2**, 387-399.

19. W.-T. Chen, A. Chan, Z. H. N. Al-Azri, A. G. Dosado, M. A. Nadeem, D. Sun-Waterhouse, H. Idriss and G. I. N. Waterhouse, *J. Catal.*, 2015, **329**, 499-513.

20. T. Jafari, E. Moharreri, A. S. Amin, R. Miao, W. Song and S. L. Suib, *Molecules*, 2016, **21**, 900.

21. D. F. Swearer, H. Zhao, L. Zhou, C. Zhang, H. Robatjazi, J. M. P. Martirez, C. M. Krauter, S. Yazdi, M. J. McClain, E. Ringe, E. A. Carter, P. Nordlander and N. J. Halas, *Proc. Natl. Acad. Sci. U. S. A.*, 2016, **113**, 8916-8920.

22. M. L. Brongersma, N. J. Halas and P. Nordlander, *Nat. Nanotechnol.*, 2015, **10**, 25-34.

23. L. Zhou, D. F. Swearer, C. Zhang, H. Robatjazi, H. Zhao, L. Henderson, L. Dong, P. Christopher, E. A. Carter, P. Nordlander and N. J. Halas, *Science*, 2018, **362**, 69-72.

24. U. Aslam, V. G. Rao, S. Chavez and S. Linic, *Nat. Catal.*, 2018, **1**, 656-665.

25. L. Zhou, J. M. P. Martirez, J. Finzel, C. Zhang, D. F. Swearer, S. Tian, H. Robatjazi, M. Lou, L. Dong, L. Henderson, P. Christopher, E. A. Carter, P. Nordlander and N. J. Halas, *Nat. Energy*, 2020, **5**, 61-70.

26. Z.-j. Wang, H. Song, H. Pang, Y. Ning, T. D. Dao, Z. Wang, H. Chen, Y. Weng, Q. Fu, T. Nagao, Y. Fang and J. Ye, *Appl. Catal., B*, 2019, **250**, 10-16.

27. A. Marimuthu, J. Zhang and S. Linic, *Science*, 2013, **339**, 1590-1593.

28. C. Zhang, H. Zhao, L. Zhou, A. E. Schlather, L. Dong, M. J. McClain, D. F. Swearer, P. Nordlander and N. J. Halas, *Nano Lett.*, 2016, **16**, 6677-6682.

29. S. Luo, H. Song, D. Philo, M. Oshikiri, T. Kako and J. Ye, *Appl. Catal., B*, 2020, **272**, 118965.

30. D. F. Swearer, H. Robatjazi, J. M. P. Martirez, M. Zhang, L. Zhou, E. A. Carter, P. Nordlander and N. J. Halas, *ACS Nano*, 2019, **13**, 8076-8086.

31. E. D. Palik, *Handbook of optical constants of solids*, Academic press, 1998.

32. W. S. M. Werner, K. Glantschnig and C. Ambrosch-Draxl, *J. Phys. Chem. Ref. Data*, 2009, **38**, 1013-1092.

33. J. C. M. Garnett and J. Larmor, *Philosophical Transactions of the Royal Society of London. Series A, Containing Papers of a Mathematical or Physical Character*, 1906, **205**, 237-288.

34. P. Giannozzi, S. Baroni, N. Bonini, M. Calandra, R. Car, C. Cavazzoni, D. Ceresoli, G. L. Chiarotti, M. Cococcioni, I. Dabo, A. Dal Corso, S. de Gironcoli, S. Fabris, G. Fratesi, R. Gebauer, U. Gerstmann, C. Gougoussis, A. Kokalj, M. Lazzeri, L. Martin-Samos, N. Marzari, F. Mauri, R. Mazzarello, S. Paolini, A. Pasquarello, L. Paulatto, C. Sbraccia, S. Scandolo, G. Sclauzero, A. P. Seitsonen, A. Smogunov, P. Umari and R. M. Wentzcovitch, *J. Phys.: Condens. Matter*, 2009, **21**, 395502.

35. P. Giannozzi, O. Andreussi, T. Brumme, O. Bunau, M. Buongiorno Nardelli, M. Calandra, R. Car, C. Cavazzoni, D. Ceresoli, M. Cococcioni, N. Colonna, I. Carnimeo, A. Dal Corso, S. de Gironcoli, P. Delugas, R. A. DiStasio, A. Ferretti, A. Floris, G. Fratesi, G. Fugallo, R. Gebauer, U. Gerstmann, F. Giustino, T. Gorni, J. Jia, M. Kawamura, H. Y.

Ko, A. Kokalj, E. Küçükbenli, M. Lazzeri, M. Marsili, N. Marzari, F. Mauri, N. L. Nguyen, H. V. Nguyen, A. Otero-de-la-Roza, L. Paulatto, S. Poncé, D. Rocca, R. Sabatini, B. Santra, M. Schlipf, A. P. Seitsonen, A. Smogunov, I. Timrov, T. Thonhauser, P. Umari, N. Vast, X. Wu and S. Baroni, *J. Phys.: Condens. Matter*, 2017, **29**, 465901.

36. J. P. Perdew, K. Burke and M. Ernzerhof, *Phys. Rev. Lett.*, 1996, **77**, 3865-3868.

37. G. Kresse and D. Joubert, *Phys. Rev. B*, 1999, **59**, 1758-1775.

38. S. Grimme, *J. Comput. Chem.*, 2006, **27**, 1787-1799.

39. V. Barone, M. Casarin, D. Forrer, M. Pavone, M. Sambi and A. Vittadini, *J. Comput. Chem.*, 2009, **30**, 934-939.

40. J. K. Nørskov, J. Rossmeisl, A. Logadottir, L. Lindqvist, J. R. Kitchin, T. Bligaard and H. Jónsson, *J. Phys. Chem. B*, 2004, **108**, 17886-17892.

41. J. Rossmeisl, A. Logadottir and J. K. Nørskov, *Chem. Phys.*, 2005, **319**, 178-184.

42. A. A. Peterson, F. Abild-Pedersen, F. Studt, J. Rossmeisl and J. K. Nørskov, *Energy Environ. Sci.*, 2010, **3**, 1311-1315.

43. D.-H. Lim and J. Wilcox, *J. Phys. Chem. C*, 2012, **116**, 3653-3660.

44. S. Kattel, P. Atanassov and B. Kiefer, *J. Phys. Chem. C*, 2012, **116**, 17378-17383.

45. Y. Wang, H. Yuan, Y. Li and Z. Chen, *Nanoscale*, 2015, **7**, 11633-11641.

46. R. Car and M. Parrinello, *Phys. Rev. Lett.*, 1985, **55**, 2471-2474.

47. A. D. Becke, *Phys. Rev. A*, 1988, **38**, 3098-3100.

48. C. Lee, W. Yang and R. G. Parr, *Phys. Rev. B*, 1988, **37**, 785-789.

49. N. Troullier and J. L. Martins, *Phys. Rev. B*, 1991, **43**, 1993-2006.

50. M. Oshikiri, J. Ye and M. Boero, *J. Phys. Chem. C*, 2014, **118**, 8331-8341.

51. S. S. Rao and T. Anantharaman, *Current Science*, 1963, **32**, 262-263.

52. M. Romand, M. Roubin and J. P. Deloume, *J. Electron. Spectrosc. Relat. Phenom.*, 1978, **13**, 229-242.

53. K. S. Kim, S. W. Gaarenstroom and N. Winograd, *Chem. Phys. Lett.*, 1976, **41**, 503-506.

54. C. D. Wagner, *Faraday Discuss. Chem. Soc.*, 1975, **60**, 291-300.

55. A. Naldoni, M. D'Arienzo, M. Altomare, M. Marelli, R. Scotti, F. Morazzoni, E. Selli and V. Dal Santo, *Appl. Catal., B*, 2013, **130-131**, 239-248.

56. G. L. Chiarello, M. H. Aguirre and E. Selli, *J. Catal.*, 2010, **273**, 182-190.

57. Z. Sun, S. Fang, Y. Lin and Y. H. Hu, *Chem. Eng. J.*, 2019, **375**, 121909.

58. C. Qi, J. C. Amphlett and B. A. Peppley, *Catal. Lett.*, 2005, **104**, 57-62.

59. T. Shishido, Y. Yamamoto, H. Morioka, K. Takaki, K. Takehira, *Appl. Catal. A* 2004, ***263*** **(2)**, 249-253.

60. J. Toyir, P. Ramírez de la Piscina, N. Homs, *Int. J. Hydrogen Energy* 2015, **40 (34),** 11261-11266.

61. N. Iwasa, S. Kudo, H. Takahashi, S. Masuda and N. Takezawa, *Catal. Lett.*, 1993, **19**, 211-216.

62. X. Liu, Y. Men, J. Wang, R. He and Y. Wang, *J. Power Sources*, 2017, **364**, 341-350.

63. L. Yuan, M. Lou, B. D. Clark, M. Lou, L. Zhou, S. Tian, C. R. Jacobson, P. Nordlander and N. J. Halas, *ACS Nano*, 2020, **14**, 12054-12063.

64. N. Takezawa and N. Iwasa, *Catal. Today*, 1997, **36**, 45-56.

65. B. Frank, F. C. Jentoft, H. Soerijanto, J. Kröhnert, R. Schlögl and R. Schomäcker, *J. Catal.*, 2007, **246**, 177-192.

66. T. Kazunari, K. Haruo and T. Nobutsune, *Chemistry Letters*, 1985, **14**, 759-762.

67. K. Takahashi, N. Takezawa and H. Kobayashi, *Applied Catalysis*, 1982, **2**, 363-366.

68. E. Santacesaria and S. Carrá, *Applied Catalysis*, 1983, **5**, 345-358.

69. J. Weigel, R. A. Koeppel, A. Baiker and A. Wokaun, *Langmuir*, 1996, **12**, 5319-5329.

70. D. B. Clarke, D. K. Lee, M. J. Sandoval and A. T. Bell, *J. Catal.*, 1994, **150**, 81-93.

71. V. Lochař, *Applied Catalysis A: General*, 2006, **309**, 33-36.

72. D. K. Kim and E. Iglesia, *J. Phys. Chem. C*, 2008, **112**, 17235-17243.

73. F. Westheimer, *Chem. Rev.*, 1961, **61**, 265-273.

74. S. Linic, U. Aslam, C. Boerigter and M. Morabito, *Nat. Mater.*, 2015, **14**, 567-576.

75. H. Song, X. Meng, Z.-j. Wang, Z. Wang, H. Chen, Y. Weng, F. Ichihara, M. Oshikiri, T. Kako and J. Ye, *ACS Catal.*, 2018, **8**, 7556-7565.

76. S. Luo, X. Ren, H. Lin, H. Song and J. Ye, *Chem. Sci.*, 2021, DOI: 10.1039/D1SC00064K, 10.1039/D1031SC00064K.

Chapter 5 Conclusions and prospects

5.1 General conclusions

In this dissertation, I set out to push the boundaries of chemical reactions that can be initiated using plasmonic photothermal catalysis for sustainable and highly-efficient H_2 production. More specifically, this dissertation aimed to design and fabricate Cu-based nanostructures that could harvest the energy of solar light and transfer that energy into surface reactants effectively for initiating the reaction. In order to attain this objective, I considered the case of modulating the size of Cu nanoparticles to affect the light-harvesting cross-section, and the fabrication of multicomponent Cu nanostructures that composed of plasmonic Cu metals with surface-deposited active sites to regulate the charge transfer pathway. Using these Cu-based plasmonic nanostructures, I performed solar-driven alcohol dehydrogenation to produce H_2 and other high value-added chemicals (i.e., methyl formate and acetaldehyde) to demonstrate how these catalysts can harvest solar energy and trigger the excitation of hot carriers capable of initiating the catalytic reactions by activating certain chemical bonds of adsorbates. The detailed study could be concluded in the following parts.

1. Solar-driven methanol self-coupling to produce hydrogen and methyl formate over plasmonic Cu nanoparticles with optimized size

In this part, plasmonic Cu nanoparticles with different mean sizes were constructed for methanol self-coupling reaction to produce hydrogen and methyl formate with the assistance of light irradiation. The results revealed that under purely thermocatalytic condition, the catalytic activity decreased with the increasing diameter of Cu nanoparticles; while in the photo-assisted thermocatalytic reaction, the optimized Cu catalysts with an average diameter of 34.8 nm exhibited the best photo-enhanced catalytic activity among other Cu samples. With the assistance of visible light energy, an approximately 43% decrease in the apparent activation energy compared to that of purely thermocatalytic process was observed over optimized sample. Mechanistic investigations indicated that the photo-induced hot carriers from plasmonic Cu nanoparticles play a dominant role in facilitating the reaction.

2. Solar-driven production of hydrogen and acetaldehyde from ethanol on Ni-Cu bimetallic catalysts

In this part, I demonstrate an efficient solar-driven ethanol dehydrogenation process for the production of H_2 and acetaldehyde over plasmonic Ni-Cu bimetallic catalysts. Under the illumination of simulated 5.7 Suns with no external energy input, a superior H_2 production rate of 176.6 mmol $g_{catalyst}^{-1}$ h^{-1} with 3.81% of solar-to-fuel conversion efficiency is obtained. Mechanistic investigations indicate that photothermal heating and hot carrier generation over Ni-Cu catalysts take responsibility for the high activity. The apparent activation energy for ethanol dehydrogenation reaction is reduced by ~55% over Ni-Cu bimetallic catalysts under visible light irradiation compared to the pure Cu under dark condition. *In-situ* DRIFTS results reveal that the adsorbed intermediates could be activated by the photo-induced hot carriers. First-principles molecular dynamics simulation results suggest that the hot electrons produced by Cu nanoparticles easily migrate to Ni atoms and then transfer to the adsorbates, hence suppressing the non-effective carrier recombination and leading to the promotion of hydrogen production.

3. Exploiting water and methanol activation for solar-driven H_2 production: Interplay of dual active sites over plasmonic ZnCu alloy

In this part, it was demonstrated that the deposition of Zn atoms on the surface of Cu nanoparticles can serve as an excellent active site for water activation, leading to a highly-efficient solar-driven methanol steam reforming activity. Under the irradiation of simulated solar light at the maximum light intensity of 788 mW cm^{-2}, a remarkable H_2 production rate of 328 mmol $g_{catalyst}^{-1}$ h^{-1} with a high solar energy conversion efficiency of 1.2% are achieved over $Zn_{1.3}Cu_{98.7}$ without addition thermal energy input. Mechanistic investigations suggest that the introduction of Zn into Cu can enhance water dissociation with lower activation energy and promote the transfer of hot electrons from Cu to Zn sites, thus further facilitating the activation of water and methanol. Bifunctional nature of the interface between Zn and Cu together with their unique hot carrier transfer and activation capacity endow the ZnCu catalysts with outstanding activity towards solar-driven MSR.

5.2 Future prospects

Although some achievements have been made in designing efficient Cu-based plasmonic materials for alcohol reforming to produce hydrogen and other value-added chemicals, there are still a number of challenges towards the efficient alcohol reforming, the utilization of solar energy, and the reaction mechanism of photo-activation of reactants. Some issues listed below are worthy of special attention:

First, charge transfer behavior of plasmonic nanostructures is an essential factor for determining the overall catalytic activity and selectivity. Such phenomenon is attributed to the injection of hot carriers from photocatalysts to certain chemical bonds of adsorbates, resulting in a new mechanistic pathway through the selective initiation of individual elementary steps of chemical reactions. Current investigations suggest that the energy of hot carriers could be modulated by tailoring the optical properties of plasmonic nanostructures (such as SPR band position and intensity) in order to match the specific electronic states and/or vibrational modes of adsorbates, ultimately controlling the reaction selectivity precisely. Toward this end, significant advancements in design and fabrication of plasmonic nanostructures with optimal geometry and composition will be highly desirable to realize a controllable charge transfer process. For instance, combining the plasmonic metal with another chemically reactive metal is considered to be promising for constructing highly efficient plasmonic photothermal catalysts. The optical property of the catalysts is determined by plasmonic metals, and the interaction between adsorbates and reactive metals enables tunning of the electronic structure of adsorbates. By matching these optical and electronic properties, the charge transfer behavior over plasmonic metals can be regulated, inducing a preferential charge carrier injection to particular orbital of adsorbates. Besides, great efforts should also be devoted to the development of predictive theories and basic understanding of the molecular behavior on the surface of plasmonic metals, which is helpful for us to design plasmonic photothermal catalysts with optimal nanostructures and compositions.

Second, except hot carrier excitation and adsorbates activation, photo-thermal conversion is also a critical parameter which influence the performance of plasmonic photothermal catalysts. The optical characteristics (such as position of LSPR absorption peak and light absorption capacity) of plasmonic nanostructures are the fundamentals to determine the photon energy that can be utilized for participating the reaction. As for the aspect of photo-thermal conversion, transform solar-energy across the entire solar-spectrum, especially low-energy photons in visible and infrared regions, into heat should be more favorable. One potential avenue for achieving this is to synthesize complex (potentially multi-metallic) plasmonic nanostructures to create more oscillation modes and hot spots, resulting in a full solar-spectrum response. Besides, modification of the nanostructures to improve the antireflection may result in enhanced sunlight harvesting ability, improving the photo-thermal conversion.

Third, plasmonic photothermal catalysis is a newly developed technology in the broad area of catalysis. Basic understandings of the reaction mechanism, such as hot-carrier generation and reactant activation on the plasmonic nanostructures, remain at the preliminary stage owing to the complicated reaction pathways and limited surface characterization techniques. Advanced mechanistic investigations, such as excited-state theoretical calculation and *in-situ* transient surface analysis are expected to provide some convincing evidences to unravel the interaction process between plasmonic nanostructures and reactants. In addition, in the plasmonic photothermal catalysis system, photothermal heat and hot carrier transfer are likely to act in concert, and the contribution of each factor remains to be clarified qualitatively and quantitively. In order to investigate the underlying thermodynamics and kinetics of plasmonic photothermal catalytic reactions, more technologies are required for not only accurately measuring the surface temperature of catalysts, but also identifying the transient species generated during the reaction.

Acknowledgement

First of all, I would like to express my sincere gratitude to my supervisor Prof. Jinhua Ye. Thank you for giving me the opportunity to conduct my Ph.D study at Hokkaido University. Thank you for your valuable guidance, fruitful discussions, incredible patience, and continuous encouragement throughout my study. All your positive altitude and great passion will benefit me through my whole life. I am appreciated to have the opportunity to study under the supervision of Prof. Ye.

I am also grateful to my supervisors, Prof. Yasuchika Hasegawa and Prof. Naoto Shirahata. Thank you for all your suggestions and kind help during my PhD study.

I would like to thank the China Scholarship Council for the financial support during my PhD study.

Then, I would like to thank Dr. Hui Song, who gave me a lot of advice for my research. I also want to thank all the members in the Photocatalytic Materials Group in NIMS and the persons who have helped me. I will cherish these memorable days with you forever. I would like to express my thanks to Dr. Huiwen Lin, Dr. Gaoliang Yang, Dr. Yunxiang Li, Mr. Qi Wang, Mr. Xiaohui Ren, Ms. Sijie Li, Dr. Yu He, Mr. Davin Philo, Mr. Bowen Deng, Ms. Lan Li, Dr. Shengyao Wang, Dr. Li Shi, Dr. Xusheng Wang, Dr. Hong Pang, Dr. Fumihiko Ichihara, Dr. Tetsuya Kako, Dr. Mitsutake Oshikiri, Ms. Kanae Hasegawa and Ms. Haruna Kaunang for their kind helps in both experiments and daily life.

Last but not least, I would like to express my deepest gratitude to my dearest family members. Thank you for your endless love and constant encouragement all the time. Your love is the source of my happiness.